

We are committed to providing [accessible customer service](#).

If you need accessible formats or communications supports, please [contact us](#).

Nous tenons à améliorer [l'accessibilité des services à la clientèle](#).

Si vous avez besoin de formats accessibles ou d'aide à la communication, veuillez [nous contacter](#).

Michael Zhdanov CEO  
4001 S 700 E STE 500,  
Salt Lake City, UT 84107, USA  
+1 801 264 6700  
mzhdanov@technoimaging.com

**CONFIDENTIAL**

**Final Report**

**Three-dimensional inversion of VTEM electromagnetic  
and TMI data in  
Echum Project Area, Wawa, Ontario, Canada**

Prepared for

**KINGSVIEW MINERALS LTD.  
(KINGSVIEW)**

Attn: Jamie Macintosh, President and CEO  
Kingsview Minerals Ltd.  
2702 – 401 Bay Street  
Toronto, Ontario M5H 2Y4, CANADA  
+1 416 862 7003  
[jmacintosh@rogers.com](mailto:jmacintosh@rogers.com)

October 18<sup>th</sup>, 2021

## Table of Contents

<b>1</b>	<b>Executive Summary</b> .....	<b>4</b>
<b>2</b>	<b>Introduction</b> .....	<b>6</b>
2.1	Kingsview Project in the Geological and Geophysical Context	6
2.1.1	Geological context	6
2.1.2	Geophysical context	9
2.2	Data Provided by Kingsview to TechnoImaging	10
2.3	Echum Project	11
<b>3</b>	<b>Data Collection</b> .....	<b>12</b>
3.1	VTEM™ Plus with Horizontal Cross-Line Magnetic Gradiometer	13
3.1.1	VTEM System parameters	14
<b>4</b>	<b>Overview of the Modeling and Inversion Algorithms</b> .....	<b>20</b>
4.1	Modeling of VTEM data	20
4.1.1	Modeling Checks	21
4.2	VTEM™ plus Inversion	21
4.3	TMI Inversion	21
4.3.1	Magnetic vector properties and susceptibility	21
4.3.2	Focusing regularization	22
4.3.3	The moving sensitivity domain approach	24
<b>5</b>	<b>Inversion of Echum Project Area</b> .....	<b>25</b>
5.1	VTEM Inversion Specifications	25
5.1.1	Data processing	25
5.1.2	Components	25
5.1.3	Inversion parameters and workflow	25
5.2	TMI Inversion	26
5.2.1	System parameters	26
5.2.2	Data processing	26
5.2.3	Inversion parameters and workflow	29
<b>6</b>	<b>Discussion of the results</b> .....	<b>29</b>
6.1	VTEM Inversion Results	29
6.1.1	3D Versus 1D Inversion	36
6.1.2	Chargeability Inversion Results	38

6.2	TMI Inversion Results	43
7	Digital Deliverables .....	53
8	Recommendations for a Follow-up Study .....	54
9	Conclusions .....	54
10	References .....	55



## 1 Executive Summary

TechnoImaging has completed the final 3D inversion of 387 line-km of VTEM and Total Magnetic Intensity (TMI) data at 100-meter line spacing over the Echum Project Area, 54 km ENE of the town of Wawa in Northwestern Ontario, Canada for Kingsview Minerals Ltd.

A comprehensive review of the historic data over the Echum Project Area is presented in a 146-page 43-101 technical report on the property by Robert. G Komarechka, P.Geo. of Bedrock Research Corp. (April 2021). The technical report summarizes the 4 known mineralized zones that occur on the Property include: the Ballard Lake showing (Au), the Davies Lead Occurrence (Pb, Au), the Davies Gold Occurrence (Au), and the M.P.D showing (Zn, Cu).

The 43-101 report also references a 2017 report by RTC Minerals over the Ballard Lake Property and the initial diamond drilling, which focused on historical gold mineralization returning anomalous gold values as well as IP anomalies. The diamond drilling intersected alkali ultramafic dikes are interpreted to be potentially associated with deep crustal or mantle tapping conduits. These conduits are claimed to be verified by the alkali ultramafic and kimberlite rocks located within the claim block.

The 43-101 report referenced the helicopter airborne VTEM and magnetometer survey that was conducted in February 2021. This survey discovered a significant multichannel VTEM anomaly near the MPD zinc copper occurrence outside the main magnetic anomaly. The magnetometer survey also encountered several negative circular anomalies about the diameter of typical kimberlites.

The VTEM dB/dt data were successfully inverted into 3D conductivity and chargeability voxel models. The TMI data were inverted into both 3D magnetic susceptibility models and 3D magnetization vector (remanent magnetization) models. All four types of inverse models have been provided to Kingsview in the form of 3D voxel files.

All valid channels and both the horizontal components (X-along line) and vertical (Z) components of the trapezoidal waveform dB/dt field were simultaneously fit to a **Glass Earth®** conductivity and chargeability model. Many features have been brought out by including the X and Z component data in the inversion, which can be achieved with TechnoImaging's patented 3D inversion methods, because the traditional layered earth 1D inversion, provided by most of the contractors, is not sensitive to the horizontal component.

Processed TMI data were independently fit to **Glass Earth®** magnetic susceptibility and magnetization vector models. TechnoImaging's 3D magnetization vector inversion method is sensitive to both induced and remanent magnetization, whereas traditional magnetic susceptibility inversion methods are sensitive to induced magnetization only. Many features of interest have been brought into focus in the magnetization vector model that are less apparent in the susceptibility model.

Deliverables include 3D conductivity and chargeability models, 3D magnetic susceptibility models and 3D magnetization vector models in UBC mesh/model format, conductivity, chargeability, and magnetic properties, and this final report.

A list of deliverables is provided below:

- 1) 3D volume of conductivity derived from AEM data

- 2) 3D volume of chargeability derived from AEM data
- 3) 3D volume of magnetic susceptibility derived from TMI data
- 4) 3D volume of magnetization vector derived from TMI data
- 5) Final report in PDF format

## 2 Introduction

TechnoImaging, LLC (“TechnoImaging”) inverted 387 line-km of VTEM and Total Magnetic Intensity (TMI) data to support the exploration activities of Kingsview Minerals Ltd. (“Kingsview”). The data were quality controlled, processed, and inverted with TechnoImaging’s proprietary software, EMVision®. This software package has a suite of codes for regularized 3D inversion of geophysical data with image focusing and sharpening to better reflect geological structures. It can transform the observed airborne EM and TMI data into 3D images of rock physical properties thus rendering the subsurface entirely transparent – a metaphorical “Glass Earth®.”

This report details the data processing and inversion workflow specific to this project. For more information on the general details and methods used, please refer to the references cited in the last section of this report.

### 2.1 Kingsview Project in the Geological and Geophysical Context

#### 2.1.1 Geological context

An excellent overview of the geology of the study area is presented in the *43-101 Technical Report on the Echum Property, Bruyere, Dolson and Echum Townships, Sault Ste. Marie Mining Division, Ontario, Canada, Prepared by: Robert. G Komarechka, P.Geo., Bedrock Research Corp., April 23, 2021*. A summary of the regional geology from the report is presented below:

*“The Property is located in the southeastern part of the Wawa Greenstone Belt which consists of early 2.89- to 2.70-billion-year-old, Precambrian rock that extends inland from the northeastern margin of Lake Superior eastward to as far as Missanabi Lake, terminating along the western contact of the Kapuskasing Horst structural zone of migmatized rock. In the area of study this metavolcanic – metasedimentary belt is intruded by stocks of mafic to ultramafic bodies of different ages.*

*The volcanic unit is composed of predominantly basaltic flows overlain by more felsic flow units of dacitic composition and its pyroclastic equivalent. The granitic units found in the belt are foliated to gneissic granodiorite and trondhjemite.*

*Gold, silver, zinc, copper and iron mineralization are the common associated metallic occurrences found in the belt. Recently diamondiferous kimberlite and lamprophyre rocks have been recognized in the southeastern part of the Wawa Greenstone belt.*

*Several gold properties are found around the northwest periphery of the same granite-granodiorite batholith that occurs along the east side of the Property. Figure 1 below shows the regional geology.”*

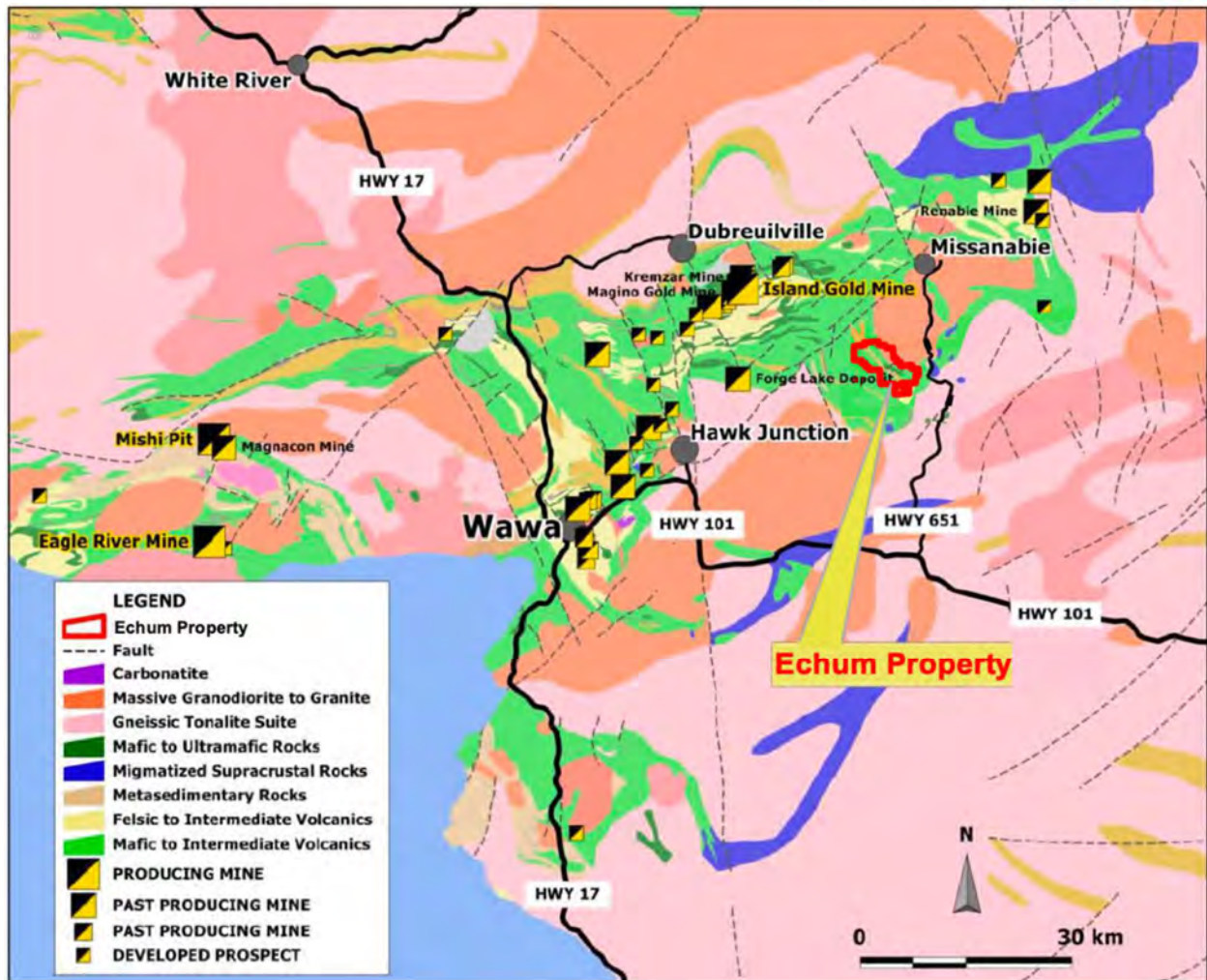


Figure 1. Regional Geology (from Figure 8 of Cullen, D., Clark Garry, 2017.) (43-101 report Figure 7, page 32)

On the Property the predominant rocks are a southeast striking sequence of mafic volcanics to the east and intermediate volcanics to the west separated by a band of metasedimentary rocks. Massive granodiorite/granite occurs along the eastern edge of the Property. Mafic (gabbro) intrusives are also located on the Property along the east side of the metasedimentary band. Ultramafic rock and kimberlite dykes are also present outside around the southeast, south and east of the property. Numerous mineral occurrences of gold and base metals have been documented on the Property.

The four known mineralized zones that occur on the Property include: the Ballard Lake Showing (Au), the Davies Lead Occurrence (Pb, Au), the Davies Gold Occurrence (Au) and the M.P.D. Showing (Zn, Cu). Diamondiferous kimberlite has been found within several kilometres outside of the Property boundary. There are no mineral resources or mineral reserves within the Property boundaries.

The 3 gold occurrences on the Property are in mafic volcanics near the eastern contact of



granodiorite to the northeast and associated with the 120°-150° striking, steeply dipping, Ballard Lake Shear. See Figures 2 and 3.

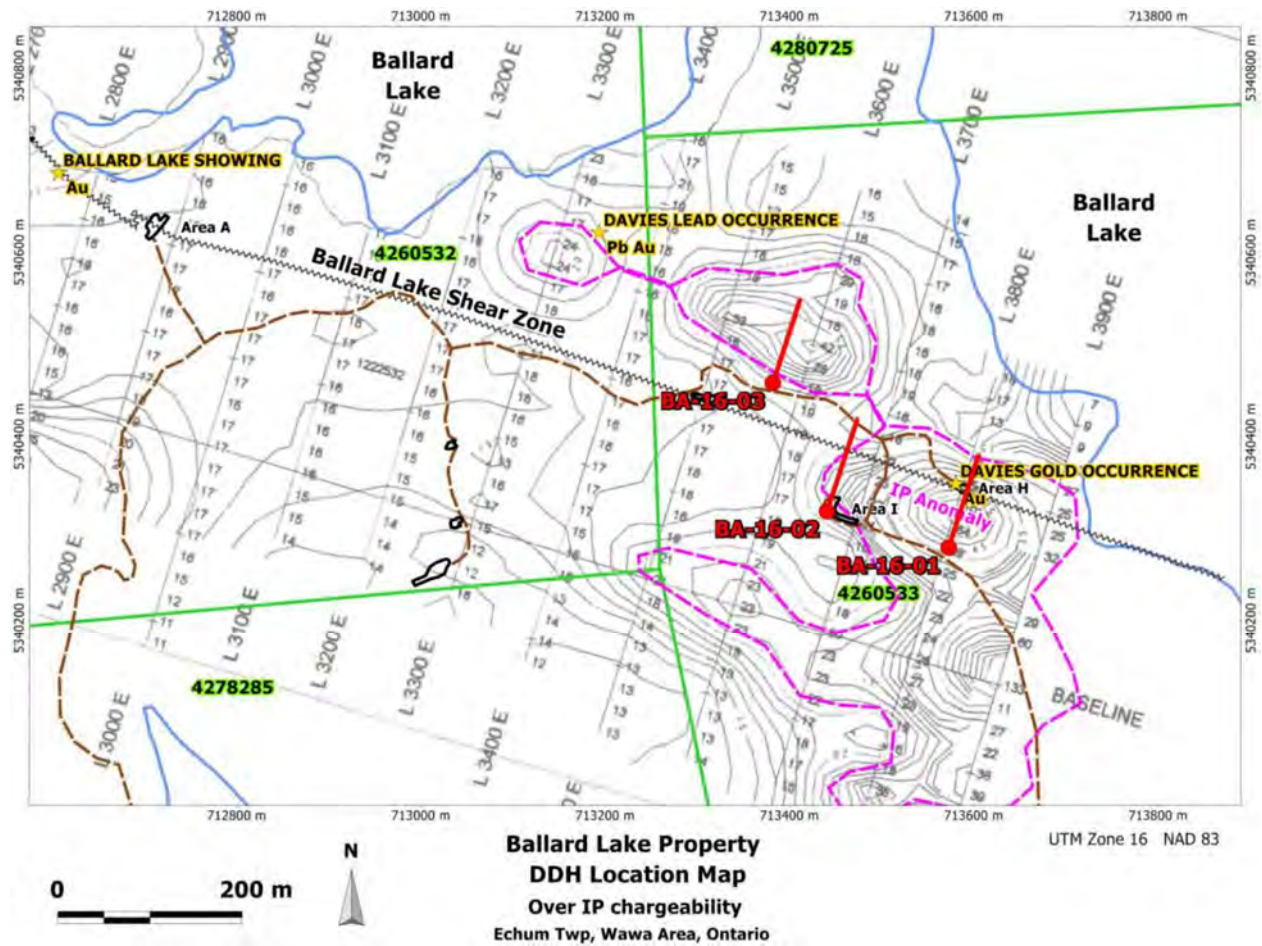
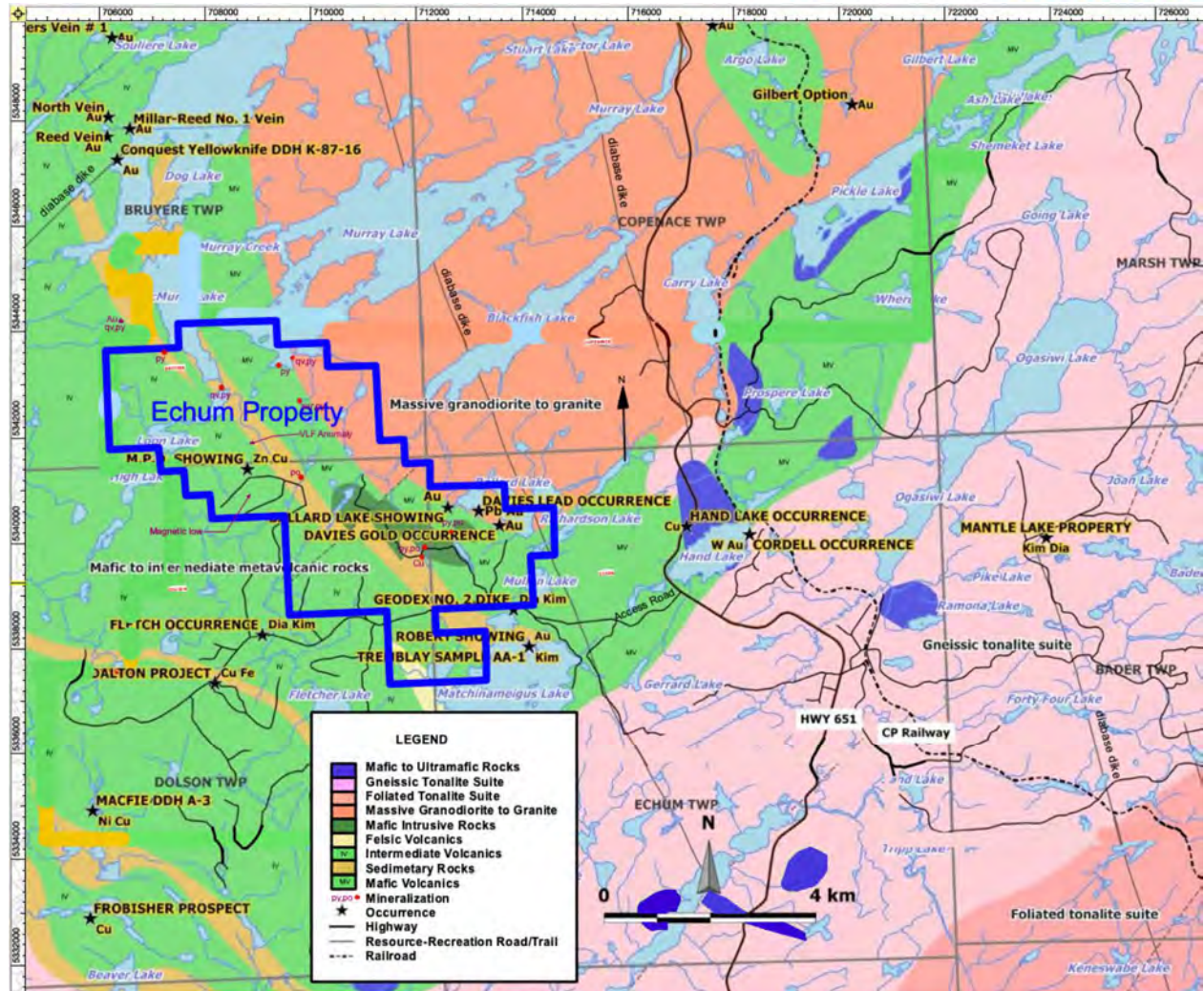


Figure 2. RT Minerals Corp. 2016 Drill Hole Locations showing the earlier claim fabric held by RT Minerals Corp over IP chargeability. (from Figure 5 of Cullen, D., Clark Garry, 2017.)



### 2.1.2 Geophysical context

Geotech conducted a VTEM and magnetometer helicopter survey over the Echum Property in February 2021. A total magnetic intensity map is shown below. In addition, an interpretive map showing a VTEM B-Field Z Component Profiles of Time Gates 0.220-7.036ms over the Total Magnetic Intensity is displayed along with the known occurrences on the Property.



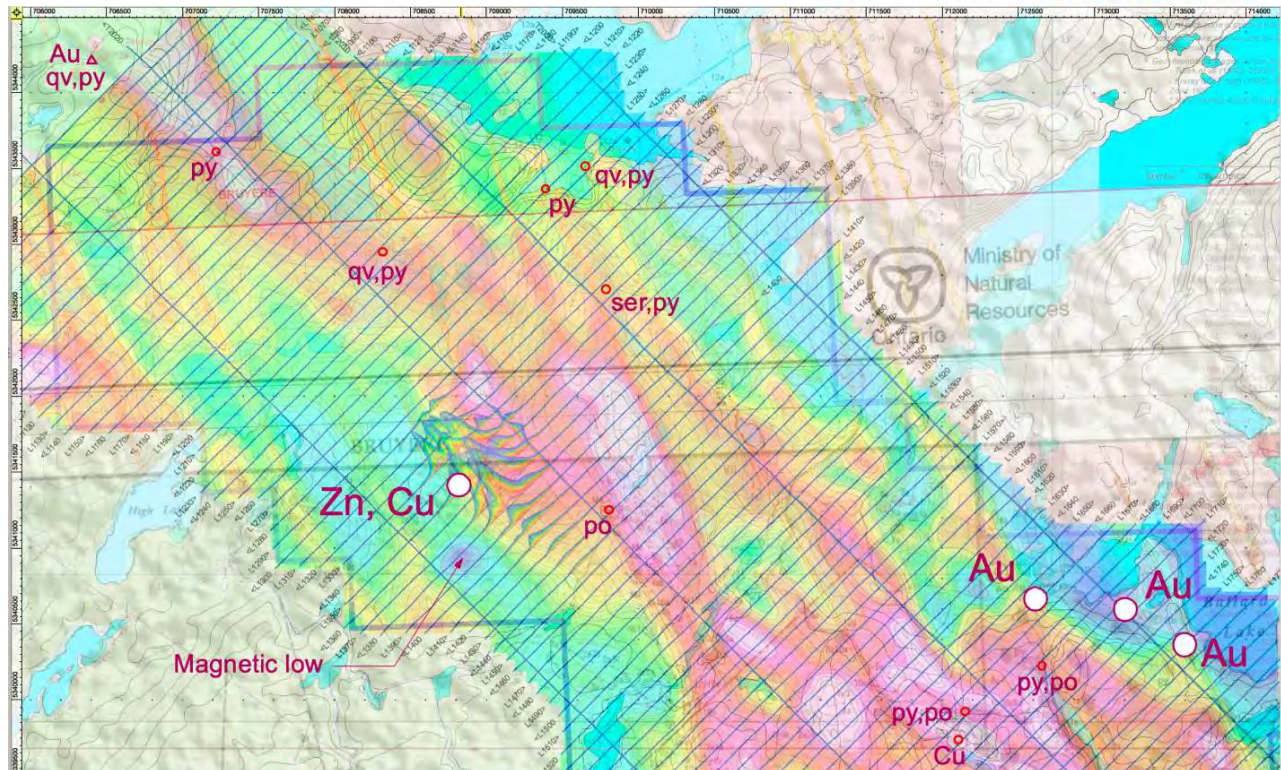


Figure 4. Geophysical map of TMI data (color map) and Bz profiles with known mineral occurrences.

Furthermore, a map with ground-based chargeability anomalies from the southeast part of the survey was also provided (Figure 2). These can be used to correlate airborne chargeability with ground chargeability. This is examined in more detail in the discussion section.

## 2.2 Data Provided by Kingsview to TechnoImaging

TechnoImaging received the following digital archive datasets from Kingsview that included logistics reports, a detailed description of the VTEM and TMI system and survey specifications of the VTEM<sup>TM</sup> and Horizontal Magnetic Gradient System. Also included were shape files of surface lithological boundaries and interpreted fault locations.

- VTEM<sup>TM</sup> Data
  - *GL200223\_Report.pdf*: Report on a helicopter-borne Versatile Time Domain ElectroMagnetic (VTEM<sup>TM</sup> plus) and Horizontal Magnetic Gradiometer geophysical survey
  - *GL200223\_Digital Archives: Database (.gdb), Grids (.grd & .tif), Maps(.map & .pdf), RDI's (data bases, depth slices, section grids, voxels, .pdf), waveform (.gdb)*

- Geological Data
  - *43-101 Technical Report on the Echum Property, Bruyere, Dolson and Echum Townships, Sault Ste. Marie Mining Division, Ontario, Canada, Prepared by: Robert. G Komarechka, P.Geo., Bedrock Research Corp., April 23, 2021*
  - *Echum geophysics program: Part 1 & 2*
  - *Echum past assessment work*

### 2.3 Echum Project

In 2021, Geotech collected approximately 387 line-km of VTEM and TMI data at 100 m line spacing in an NE-SW direction and 1 km tie lines in a NW-SE direction. TechnoImaging inverted the VTEM and TMI data set, which covers approximately 34 square km, 54 km ENE of the town of Wawa in Northwestern, Ontario. Figure 5 shows the full VTEM survey location in red and its approximate location. Figure 6 shows the VTEM survey flight path in red, plotted on a Google Earth image.



Figure 5. Echum Project VTEM survey location shown in red on a Google Earth image.



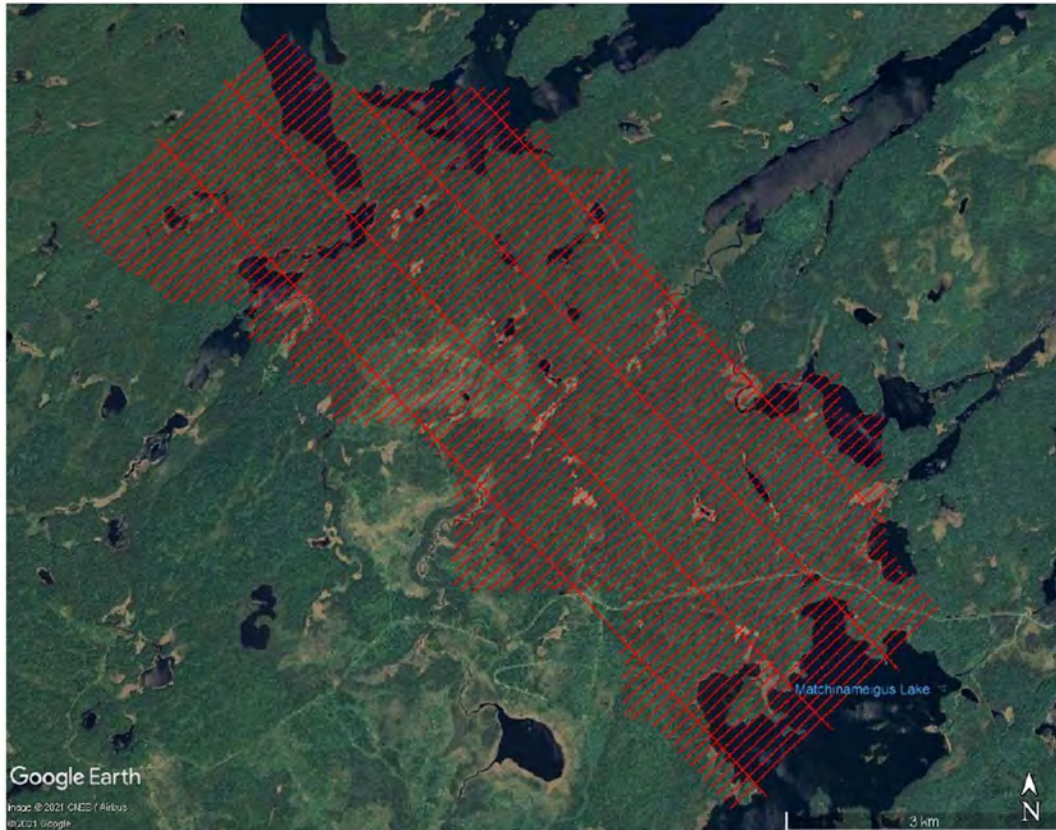


Figure 6. Echum project VTEM flight path plotted on a Google Earth Image

### 3 Data Collection

The survey was flown between January 31st and February 12th, 2021, employing 100 m spaced flight lines at 045°/225° and 1 km tie lines at 135°/315° at right angles to the flight lines. The Echum project area covered 387 line-km of data that were inverted in 3D. The VTEM waveform, time gates, and system geometry were taken from the geophysical survey report by Geotech “Geophysical Report on a helicopter-borne Versatile Time Domain ElectroMagnetic (VTEM™ plus) and Horizontal Magnetic Gradiometer geophysical survey.” A photograph of the system in flight is shown in Figure 7.

### 3.1 VTEM™ Plus with Horizontal Cross-Line Magnetic Gradiometer

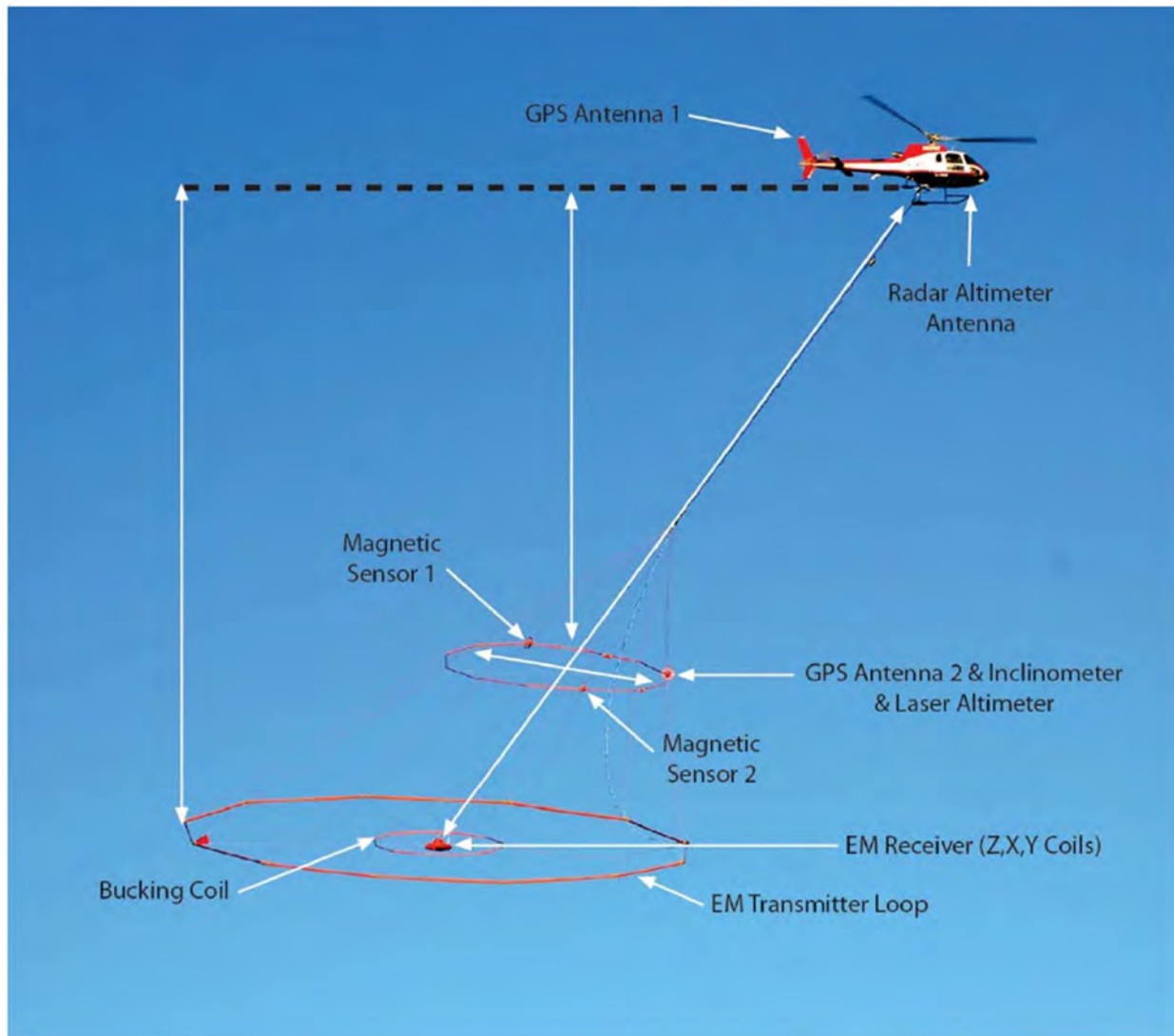


Figure 7: VTEM™ plus towed beneath an AS350B3 Helicopter

During the survey, the helicopter was maintained at a mean altitude of 108 meters above the ground with an average survey speed of 78 km/hour. This allowed for an actual average Transmitter receiver loop terrain clearance of 64 meters and a magnetic sensor clearance of 74 meters. The receiver coil is located at the center of a 26 m diameter transmitter loop and is located on the same transmitter plane as the transmitter loop. The receiver measures two components of dB/dt in the horizontal (X along line) and vertical (Z) directions. The real time navigation GPS antenna is on the tail boom of the helicopter. A radar altimeter was used to record terrain clearance of the helicopter and the antenna was mounted beneath the bubble of the helicopter cockpit. A second GPS antenna was attached to the front edge of the magnetic gradiometer to give positional information. An inclinometer and laser altimeter were also mounted on the magnetometer loop to give tilt information and terrain clearance, respectively.

Figure 8 shows the observed TMI data overlain on a property and geology occurrence map.



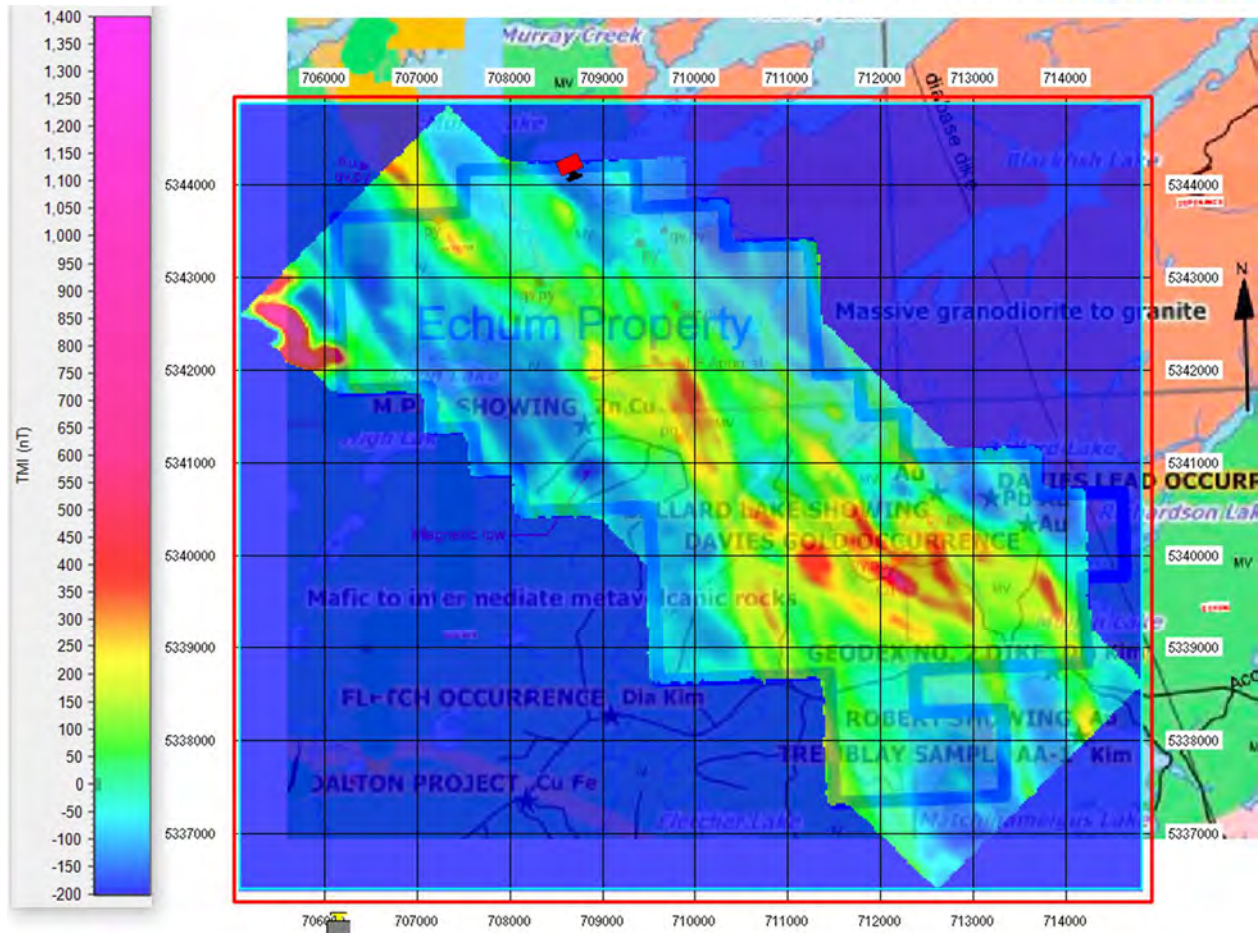


Figure 8: Echum TMI Map: From 2021 Geotech helicopter Survey. Co-ordinates are shown in NAD 83 Zone 16N.

### 3.1.1 VTEM System parameters

The electromagnetic system was a Geotech Time Domain EM (VTEM™ Plus) full receiver-waveform streamed data recorded system. The “full waveform VTEM system” uses the streamed half-cycle recording of transmitter and receiver waveforms to obtain a complete system response calibration throughout the entire survey flight. A horizontal loop transmitter produced an approximate vertical magnetic dipole for the source fields. The measured fields were vertical and inline dB/dt fields. The receiver is located in the center of the transmitter loop. VTEM with the serial number 18 had been used for the survey. The VTEM™ transmitter current waveform is shown diagrammatically in Figure 9. The VTEM™ Receiver and transmitter coils were in concentric-coplanar and Z-direction oriented configuration. The receiver system for the project also included a coincident-coaxial X-direction coil to measure the inline dB/dt and calculated B-Field responses. The Transmitter-receiver loop was towed at a mean distance of 44 meters below the aircraft as shown in Figure 7.

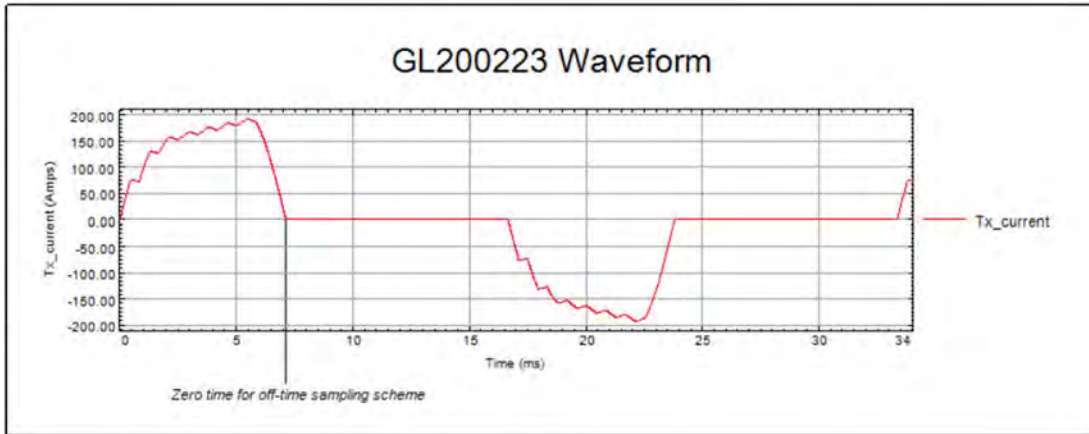


Figure 9: VTEM™ Transmitter Current Waveform

The VTEM™ decay sampling scheme is shown in Table 1 below. Forty-three-time measurement gates were archived by Geotech in the database in the range from 0.021 to 8.083 msec. Zero time for the off- time sampling scheme is equal to the current pulse width and is defined as the time near the end of the turn-off ramp where the  $dI/dt$  waveform falls to 1/2 of its peak value.

Table 1: Off-Time Decay Sampling Scheme

VTEM™ Decay Sampling Scheme				
Index	Start	End	Middle	Width
Milliseconds				
4	0.018	0.023	0.021	0.005
5	0.023	0.029	0.026	0.005
6	0.029	0.034	0.031	0.005
7	0.034	0.039	0.036	0.005
8	0.039	0.045	0.042	0.006
9	0.045	0.051	0.048	0.007
10	0.051	0.059	0.055	0.008
11	0.059	0.068	0.063	0.009
12	0.068	0.078	0.073	0.010
13	0.078	0.090	0.083	0.012
14	0.090	0.103	0.096	0.013

15	0.103	0.118	0.110	0.015
16	0.118	0.136	0.126	0.018
17	0.136	0.156	0.145	0.020
18	0.156	0.179	0.167	0.023
19	0.179	0.206	0.192	0.027
20	0.206	0.236	0.220	0.030
21	0.236	0.271	0.253	0.035
22	0.271	0.312	0.290	0.040
23	0.312	0.358	0.333	0.046
24	0.358	0.411	0.383	0.053
25	0.411	0.472	0.440	0.061
26	0.472	0.543	0.505	0.070
27	0.543	0.623	0.580	0.081
28	0.623	0.716	0.667	0.093
29	0.716	0.823	0.766	0.107
30	0.823	0.945	0.880	0.122
31	0.945	1.086	1.010	0.141
32	1.086	1.247	1.161	0.161
33	1.247	1.432	1.333	0.185
34	1.432	1.646	1.531	0.214
35	1.646	1.891	1.760	0.245
36	1.891	2.172	2.021	0.281
37	2.172	2.495	2.323	0.323
38	2.495	2.865	2.667	0.370
39	2.865	3.292	3.063	0.427
40	3.292	3.781	3.521	0.490
41	3.781	4.341	4.042	0.560

42	4.341	4.987	4.641	0.646
43	4.987	5.729	5.333	0.742
44	5.729	6.581	6.125	0.852
45	6.581	7.560	7.036	0.979
46	7.560	8.685	8.083	1.125

The Z component was measured during the time gates from 4 – 46. The X component measurements started at time gate 20 and went through 46.

Figures 10 to 13 show examples of the collected data. Three vertical (Z) components channels are one inline (X) component channel are shown. Note the X only shows a geologic response above background over a localized strong bedrock anomaly.

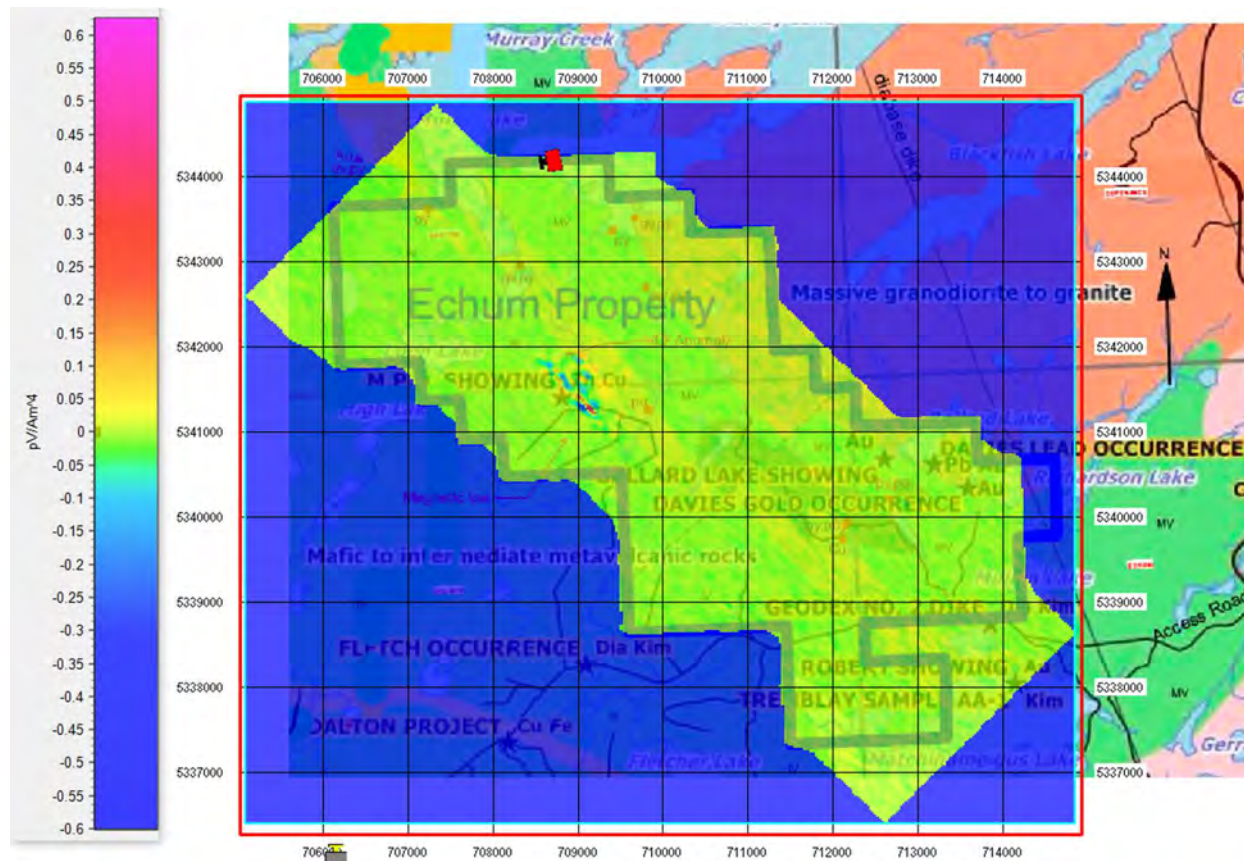


Figure 10. Echum North VTEM dbX/dt Field Map Channel 20. Chan 20 is the earliest channel and with the best signal to noise ratio. The area near 70900mE and 534100mN shows a significant response above noise level. The rest of the survey area is near noise level.



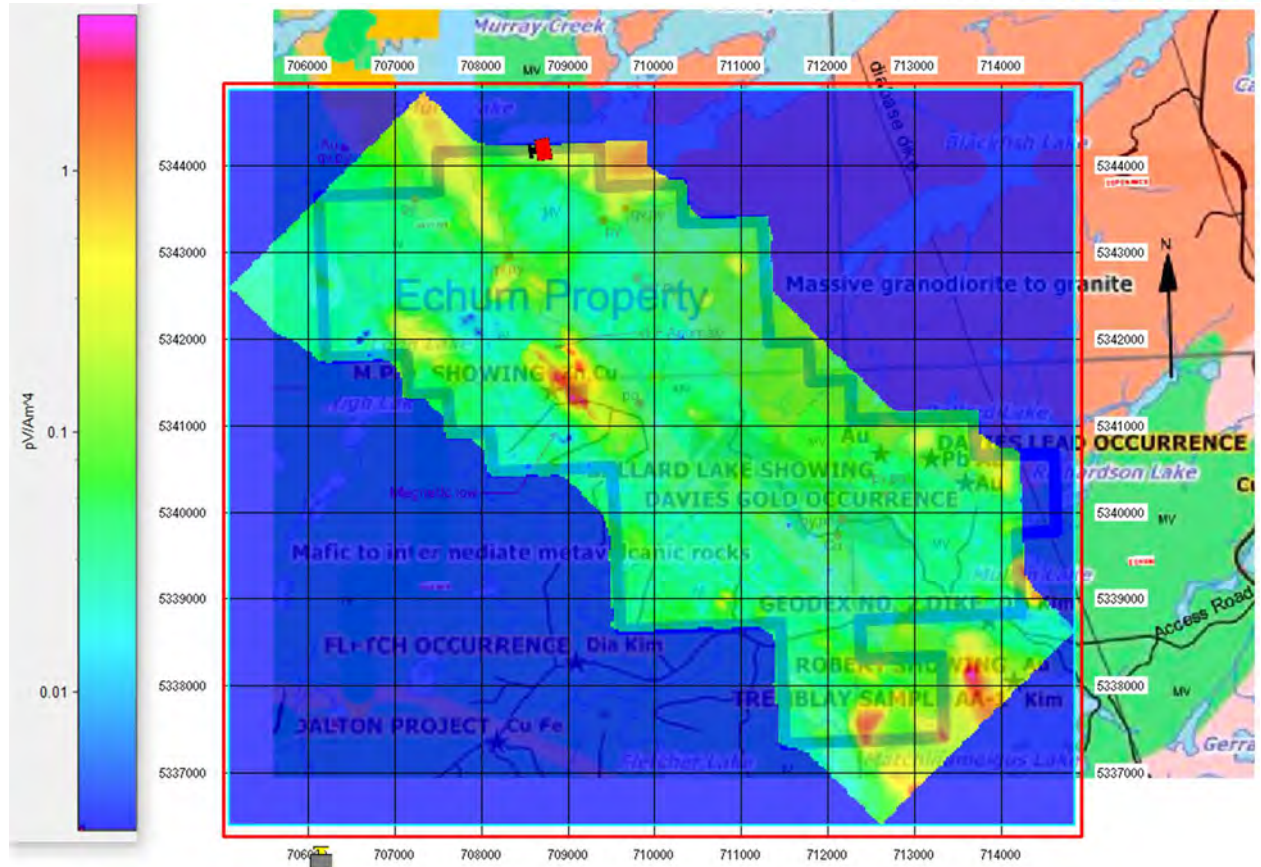


Figure 11. Echum North VTEM dbZ/dt Field Map Channel 10. Variations in overburden thickness and conductivity, plus a few bedrock conductors are seen in this channel.

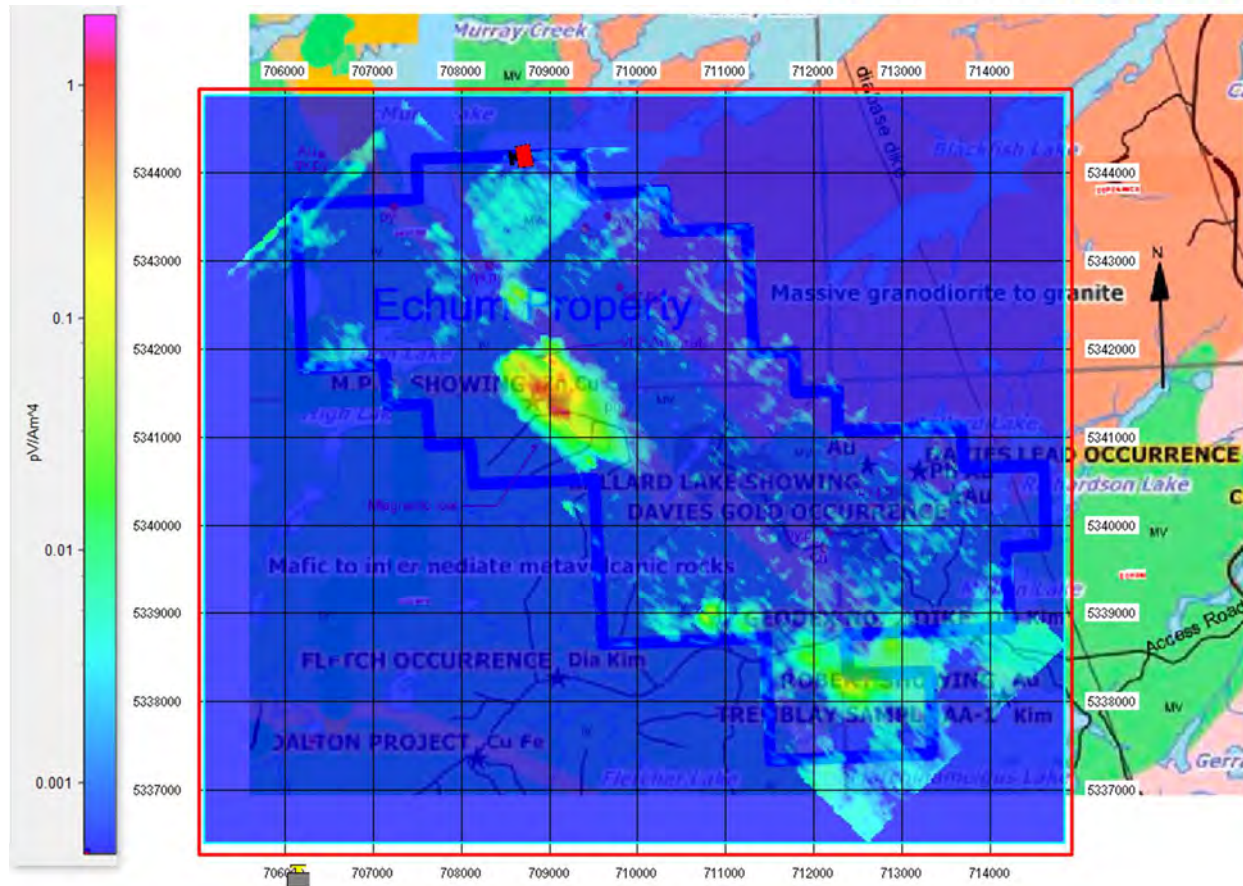


Figure 12. Echum North VTEM dbZ/dt Field Map Chan 20. Stronger bedrock conductors are seen in this channel.



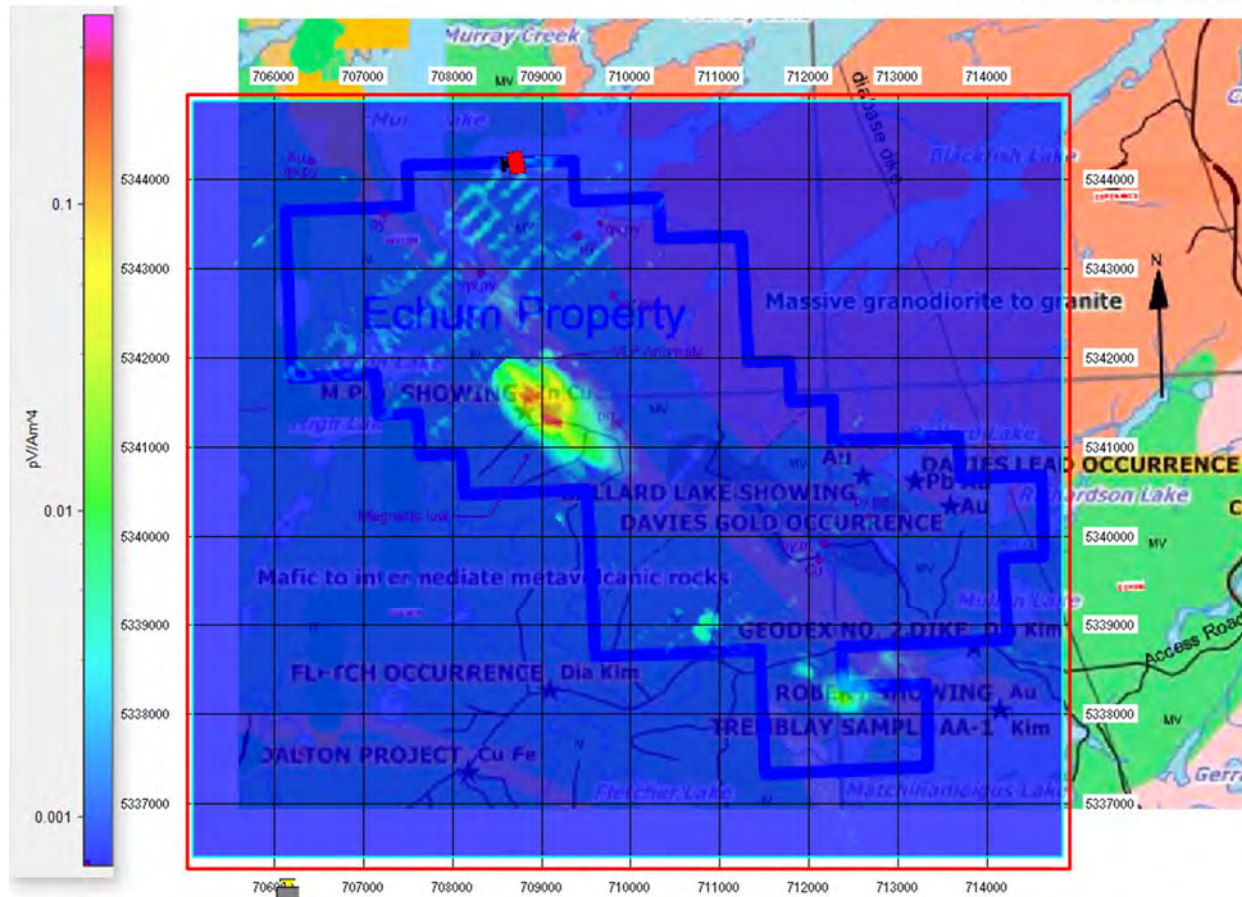


Figure 13. Echum North VTEM dbZ/dt Field Map Channel 31 (~1ms). Strong bedrock conductors are seen in this channel.

## 4 Overview of the Modeling and Inversion Algorithms

### 4.1 Modeling of VTEM data

TechnoImaging uses both one dimensional (1D) and three-dimensional (3D) inversions to process the data. In our standard workflow, 1D inversion is used to QC the data and create an approximate background model, while 3D inversion is used for final, higher accuracy inversion runs. One-dimensional inversion is typically faster than 3D inversion and can create accurate models in areas where the earth is laterally invariant. The 1D approximation is used to speed up calculations and makes the assumption that the earth is layered and these layers extend to infinity horizontally. Each transmitter-receiver position, or sounding location, has a 1D earth under it which is recovered during inversion. These are then gridded into a 3D model to create a more realistic earth picture, but the modeling and physics are not accurate. Only the Z (vertical) component can be used, because a 1D earth does not create an electromagnetic field in the X (inline) direction with a coincident system like VTEM. Hence, with 1D inversion, half the data must be ignored, and this is the half of the data that responds best to lateral variations in conductivity and produces high resolution images.

In contrast, 3D inversion considers all the geometry of the targets of the earth and can use both X and Z components to the data. The recovered models are thus much more accurate, especially in

areas which have complex geometry and geology, but this is at the expense of slower and much more complex algorithms. Therefore, most contractors do not perform full 3D inversions. TechnoImaging has multiple drivers for the 3D inversions, please see Cox et al (2015) for details.

#### 4.1.1 Modeling Checks

TechnoImaging performs a variety of checks on the forward modeling response and approximations used in the inversion to determine the accuracy and increases modeling accuracy if needed when the assumptions do not hold.

#### 4.2 VTEM™ plus Inversion

All inversions were carried out using TechnoImaging's proprietary Glass Earth® technology and EMVision® software package. The software uses a robust and stable method to solve for the 3D physical parameter distribution in the earth. Fast and accurate algorithms are used to model the physics, and flexibility in the software allows a wide selection of stabilizers, a priori models, and cooperative inversion techniques. The inversion method uses data weights to ensure fitting of the data to the appropriate noise level and model weights to normalize sensitivities of the data for increased depth resolution and stability.

The data weights for inversion are based on a two-part model: an absolute error plus a relative error. The absolute noise level considers the instrument noise floor and prevents small data values close to 0 from being overly important. The relative error level represents errors such as tilt and flight height errors. The estimate errors are listed for each survey individually. The inverse of these errors is used as data weights. Ideally, the inversion is run to a normalized  $\chi^2$  of 1:

$$\chi^2 = \frac{1}{N} \sum \left( \frac{d_i^p - d_i^o}{\varepsilon_i} \right)^2 \quad (1)$$

where  $d^p$  is the predicated data,  $d^o$  is the observed data, and  $\varepsilon_i$  is the estimated error in the  $i^{th}$  data point. The value of  $\chi^2 = 1$  indicates an optimal data fit when the prediction errors are equal to the noise level in the observed data.

However, these errors should not be taken as exactly the error levels in the data, because these are also adjusted to change the fit and convergence of the inversion during the inversion parameter testing phase. The errors should be taken as an approximate (order of magnitude) estimate.

#### 4.3 TMI Inversion

All inversions were carried out using TechnoImaging's proprietary Glass Earth® technology. A few technical highlights are detailed here.

##### 4.3.1 Magnetic vector properties and susceptibility

In mineral exploration, magnetic data have traditionally been inverted to produce magnetic susceptibility models, which represent magnetization induced by the current magnetic field. This does not take into account the remanent magnetization of the rocks produced by the ancient magnetic field. More information about rock formations and geological processes can be obtained by inverting magnetic data for magnetization vector, as opposed to magnetic susceptibility only. This is demonstrated in Figure 14, which is an example taken from the Thunderbird V-Ti-Fe deposit in Ontario, Canada. All TechnoImaging's magnetic inversions include inversions for both these properties. For more technical details, please refer to Jorgensen and Zhdanov (2021).

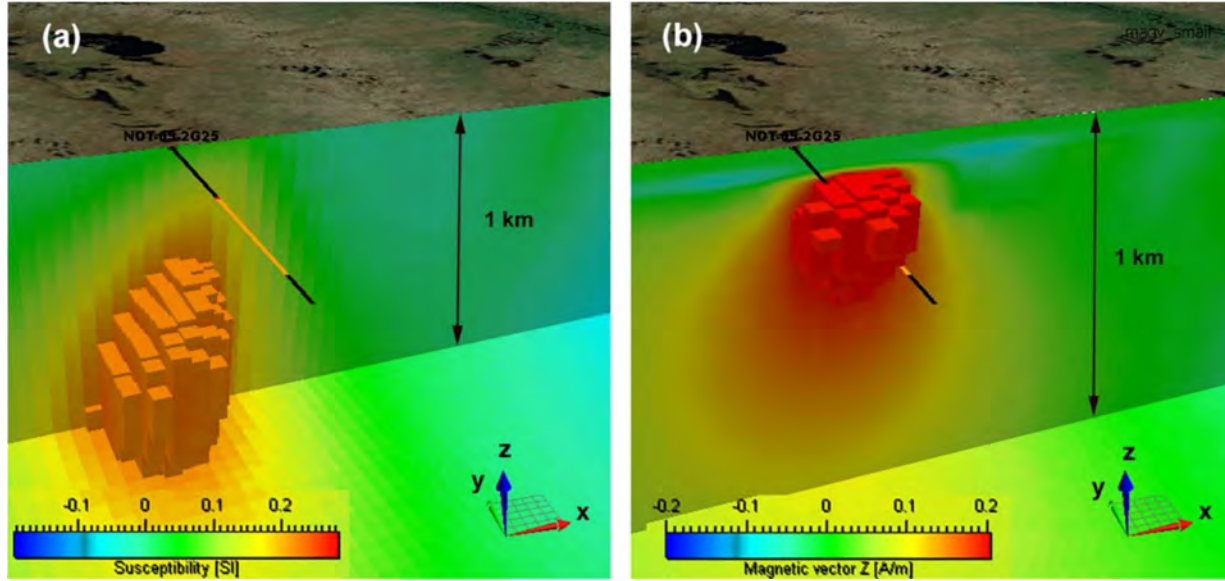


*Figure 14. Comparison of 3D inverse models with drilling results. Left panel (a) shows the volume image of the inverse susceptibility model. Right panel (b) presents the volume image of the vertical component of the magnetization vector. The black–yellow–black solid line shows the location of the borehole drilled in the survey area. The yellow color indicates the mineralization zone confirmed by drilling. The recovered magnetic vector matches the drilling much better than the susceptibility only inversion.*

#### 4.3.2 Focusing regularization

Potential field data are finite and noisy. Their inversion is inherently non-unique, meaning that there is an infinite number of source distributions that can equally satisfy the observed data. In order to solve this inverse problem, regularization must be introduced. Regularization aims to recover the most geologically plausible solutions from the infinite number of mathematically equivalent solutions. As we generalized our inversion methodology for gravity data, we describe our model parameters by vector  $\mathbf{m}$ , of length  $N_m$ . Regardless of the iterative scheme used, most regularized inversions seek to minimize the Tikhonov parametric functional,  $P^\alpha(\mathbf{m})$ :

$$P^\alpha(\mathbf{m}) = \phi(\mathbf{m}) + \alpha s(\mathbf{m}) \rightarrow \min, \quad (8)$$

where  $\phi(\mathbf{m})$  is a misfit functional of the observed and predicted potential field data,  $s(\mathbf{m})$  is a stabilizing functional, and  $\alpha$  is the regularization parameter that balances the misfit and stabilizing functional (Zhdanov, 2002). Data and model weights can be introduced to equation (8) through data and model weighting matrices. We can also re-weight the inverse problem in logarithmic space in order to reduce the dynamic range of both the data and model parameters.

In our implementation, all weighting functions are selected based upon their integrated sensitivity (Zhdanov, 2002). Our weighting functions provide equal sensitivity of the observed data to cells located at different depths and at different horizontal positions. Thus, our weighting functions

automatically introduce appropriate corrections for the vertical and horizontal distribution of the density.

All geological constraints manifest themselves as regularization that can be quantified through a choice of data weights, model upper and lower bounds, model weights, an a priori model, and the type of stabilizing functional. The latter incorporates information about the class of models used in the inversion. The choice of stabilizing functional should be based on the user's geological knowledge and prejudice. In this section, we will briefly describe different smooth and focusing stabilizers.

A minimum norm (MN) stabilizer will seek to minimize the norm of the difference between the current model and an a priori model:

$$s(\mathbf{m}) = \iiint (\mathbf{m} - \mathbf{m}_{apr})^2 dv, (9)$$

and usually produces a relatively smooth model.

The Occam (OC) stabilizer implicitly introduces smoothness with the first derivatives of the model parameters:

$$s(\mathbf{m}) = \iiint (\nabla \mathbf{m} - \nabla \mathbf{m}_{apr})^2 dv, (10)$$

and can result in spurious oscillations and artifacts when the model parameters are discontinuous. A combination of stabilizers, (9) and (10), is often used (e.g., Li and Oldenburg, 1996, 1998).

Very little geology exhibits smooth density distributions. Usually, geology is characterized by sharp boundaries of contrasting density, for example, between an ore deposit and host rock, or across a discontinuity. As such, stabilizers (9) and (10) or their combinations produce results that bear no physical relevance to the actual geology. Portniaguine and Zhdanov (1999) introduced focusing stabilizers that make it possible to recover models with sharper boundaries and contrasts. We briefly describe these stabilizers here and refer the reader to Zhdanov (2002) for further details. First, we present the minimum support (MS) stabilizer:

$$s_{MS}(\mathbf{m}) = \iiint \frac{(\mathbf{m} - \mathbf{m}_{apr})^2}{(\mathbf{m} - \mathbf{m}_{apr})^2 + e^2} dv, (11)$$

where  $e$  is a focusing parameter introduced to avoid singularity when  $\mathbf{m} = \mathbf{m}_{apr}$ . The minimum support stabilizer minimizes the volume with non-zero departures from the a priori model, effectively recovering compact bodies. Thus, a smooth distribution of all model parameters with a small deviation from the a priori model is penalized. A focused distribution of the model parameters is penalized less. Similarly, we present the minimum gradient support (MGS) stabilizer:

$$s_{MGS}(\mathbf{m}) = \iiint \frac{\nabla(\mathbf{m} - \mathbf{m}_{apr}) \cdot \nabla(\mathbf{m} - \mathbf{m}_{apr})}{\nabla(\mathbf{m} - \mathbf{m}_{apr}) \cdot \nabla(\mathbf{m} - \mathbf{m}_{apr}) + e^2} dv. (12)$$

which minimizes the volume with non-zero gradients, i.e., sharp transitions in the model parameters are penalized less than smooth transitions.

While variations of equations (11) and (12) were derived in Zhdanov (2009), we base our solution on the re-weighted regularized conjugate gradient (RRCG) method (Zhdanov, 2002), which is easier to implement numerically. This method iteratively updates the vector of model parameters  $\mathbf{m}$  so as to minimize the vector of residual errors,  $\mathbf{r}$ , akin to:



$$\mathbf{m}_{i+1} = \mathbf{m}_i + k \mathbf{A}^T \mathbf{r} \text{ subject to } \mathbf{r}_i \rightarrow \min, (13)$$

where  $k_i$  is a step length and  $\mathbf{A}^T$  is the conjugate transpose of the matrix of the gravity linear operator. The inversion proceeds to iterate in a manner similar to equation (13) until the residual error reaches a preset threshold, or a maximum number of iterations is reached. Upon completion, the quality of the inversion is appraised by the data misfit and visual inspection of the model.

#### 4.3.3 The moving sensitivity domain approach

In principle, the regularized inversion outlined above can be applied to large-scale problems. Numerically, however, the computational complexity increases linearly with the size of the problem, meaning large-scale 3D inversion faces two major obstacles. First is the large amount of computer memory required for storing the kernels of the forward modeling operators, which double as sensitivities for linear problems. Even a small-sized 3D inversion of thousands of data to 3D earth models of hundreds of thousands of cells can exceed the memory available for desktop computers. The second obstacle is a large amount of CPU time required to apply the dense matrix of the forward modeling operators to data and model vectors. One may store the matrices outside RAM or generate them at the time of processing. An alternative approach has been to exploit the translational invariance of the kernels to reduce the matrices to Toeplitz block structure and use FFTs for matrix-vector multiplication (e.g., Pilkington, 1997; Zhdanov et al., 2004). Such strategies alleviate memory limitations and reduce the CPU time dramatically. However, these methods require the data to lie over a regular grid on a flat surface above the topography. Although applicable in some special cases, it cannot address the aforementioned difficulties for topography and variable altitude.

In potential fields, the sensitivity of the data to the density variations is expressed via the appropriate kernel functions of the forward modeling operators, i.e., via the corresponding Green's functions. It was demonstrated that at some limited distance, which we call the *sensitivity domain*, the receiver is no longer sensitive to the 3D earth model. Typically, the size of the sensitivity domain is less than the size of an airborne survey. The size of the sensitivity domain for gravity fields is proportional to  $1/r^2$ ; for gravity gradiometry fields it is proportional to  $1/r^3$ .

Cox and Zhdanov (2007) introduced the concept of the moving sensitivity domain for 3D inversion of airborne electromagnetic (AEM) data. They showed that there was no need to calculate the responses or sensitivities beyond the AEM's sensitivity domain for a single transmitter-receiver pair. The sensitivity matrix for the entire 3D earth model could be constructed as the superposition of the sensitivity domain from all transmitter-receiver pairs. Zhdanov et al. (2010) also introduced the sensitivity approach for the large-scale 3D inversion of the magnetotelluric (MT) data. The framework of this approach can be described as follows: for a given receiver, compute and store the Fréchet derivative for those inversion cells within a predetermined horizontal distance from this receiver, i.e., the sensitivity domain. The radius of the sensitivity domain is based on the rate of sensitivity attenuation.

## 5 Inversion of Echum Project Area

### 5.1 VTEM Inversion Specifications

#### 5.1.1 Data processing

Powerlines and cultural features were not present in the area to an extent which required further processing or even rejecting data.

#### 5.1.2 Components

All available X channels were used for inversion. The inversion used all Z channels from channel 8 (42  $\mu$ s) a later. The earlier channels could not be fit to a reasonable level without corrupting the near surface conductivity, and the early channels are not required for exploration at depth. The Y component channels were not used because of poor signal to noise ratios in most areas.

#### 5.1.3 Inversion parameters and workflow

The final workflow for the inversion was to run the 1D inversion using EMVision® on the Z component data. This initial inversion step uses 1D sensitivities, but full 3D stabilizers and runs on a voxel discretization of the model exactly as the 3D inversion. The model for the 1D inversion was discretized into 50 m x 50 m cells in the inline and cross-line directions horizontally, and vertically discretized into 14 cells from 10 m thick at the surface to 60 m thick at depth. The total thickness of the inversion domain was 680 m. These 1D inversions were used for initial quality control of the model. The -together results of 1D inversions were smoothed by a 3 x 3 x 1 (x by y by z) cell size boxcar function. The resulting 3D model was used as a variable background conductivity model and initial conductivity model for the full rigorous 3D inversion.

Conductivity, chargeability, and time constant were all inverted for during the 1D inversion using the generalized effective-medium model of induced polarization (GEMTIP model- Zhdanov, 2008, 2018). A simplified version of this model parameterizes the conductivity as a function of frequency to describe the observed induced polarization effect by the following equation:

$$\sigma(\omega) = \sigma_0 \left( 1 + \eta \left[ 1 - \frac{1}{1 + (i\omega\tau)^C} \right] \right)$$

where  $\sigma_0$  is the DC conductivity,  $\eta$  is the chargeability,  $\tau$  is the time constant, and  $C$  is the relaxation coefficient. The relaxation coefficient was fixed at 0.5 for the entire inversion process.

The 3D inversion used a minimum norm stabilizer combined with a 2<sup>nd</sup> derivative in the crossline and vertical directions. The stabilizer ensures the algorithm finds a geologically reasonable model which also satisfies the observed data. A 1e-4 S/m (10,000 Ohm-m) hard lower bound was used in the inversion. No upper bound was needed.

After analysis of the background 1D result and further testing, it was determined that the optimal horizontal cell sizes for the full 3D inversion were 25 m x 50 m in the inline and cross-line directions, and the same vertical discretization was used as for the 1D model. The errors used for the error model in the inversion are given in Table II. The percent and absolute errors are combined into a total error by the following equation:

$$e^t = |d_o| * \frac{e^p}{100} + e^a.$$

Table II: Estimated error levels used to compute the data weights.

Datum	Relative Error (%)	Absolute Error (pV/Am <sup>4</sup> )
db <sub>x</sub> /dt	15	0.005
db <sub>z</sub> /dt	15	0.001

## 5.2 TMI Inversion

### 5.2.1 System parameters

The horizontal magnetic gradiometer consists of two Geometrics split-beam field magnetic sensors with a sampling interval of 0.1 seconds. These sensors are mounted 12.5 meters apart on a separate loop, 10 meters above the VTEM Transmitter-receiver loop. The average terrain clearance for the TMI survey was 74 m. A GPS and tilt help to determine the positions and tilt of the gradiometer. The data from the two magnetometers are corrected for position and orientation variations and for the diurnal variations using the base station data. Only one of the magnetometer data sets was used for the inversions.

### 5.2.2 Data processing

A second-degree polynomial was used to high pass filter the data and remove regional trends. No other processing was required. The data were microleveled by Geotech. Figure 15 shows the microleveled data as supplied from Geotech. Figure 16 shows the inversion-ready data after filtering.

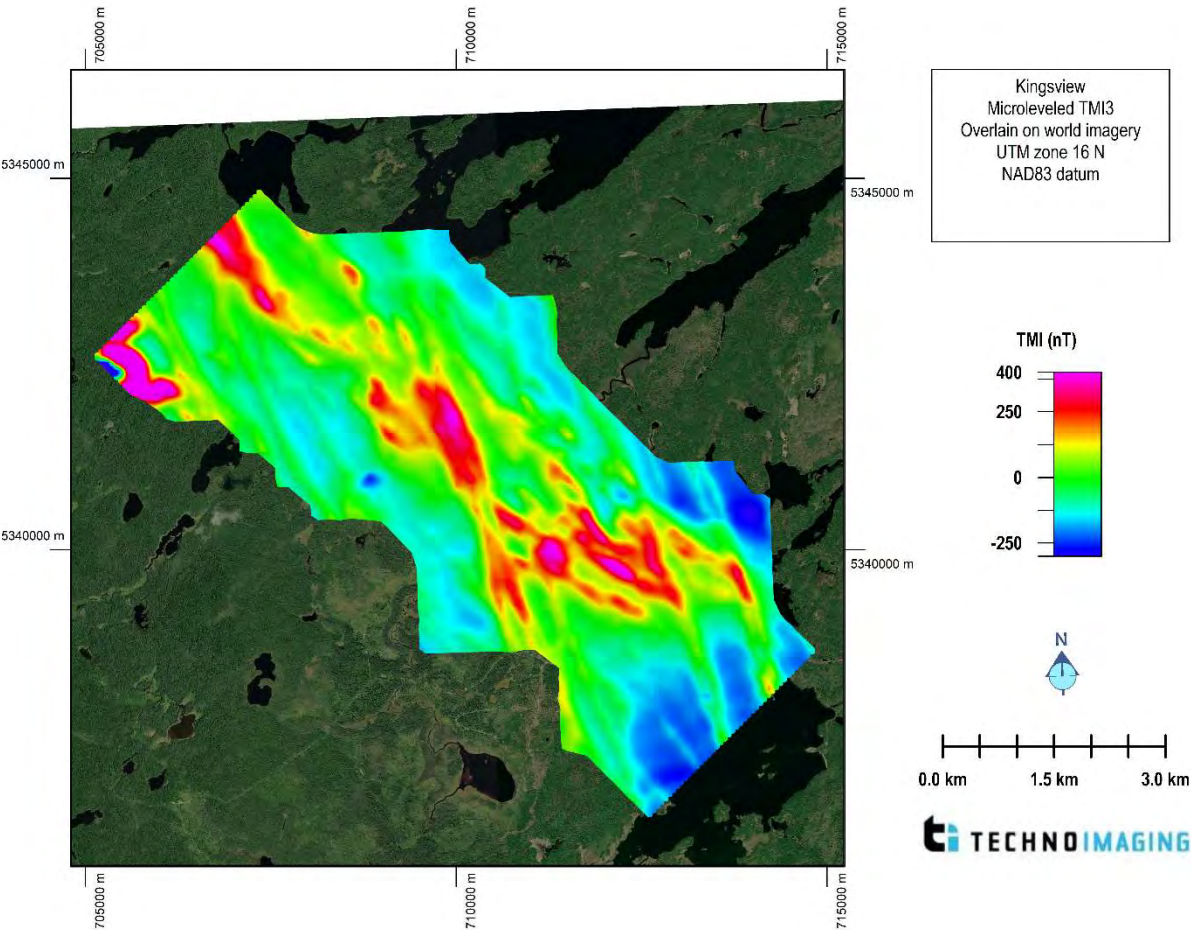


Figure 15: TMI data supplied by Geotech.



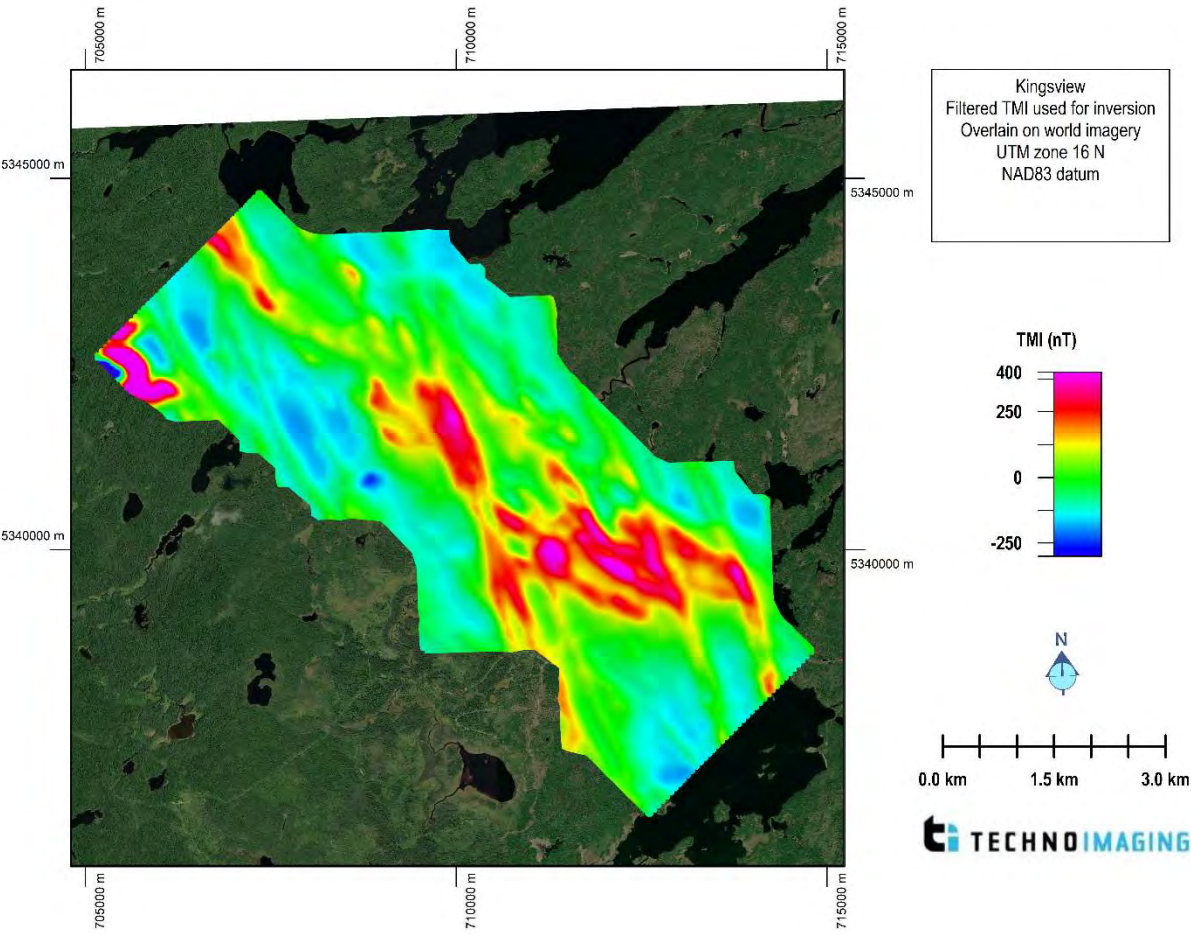


Figure 16: Filtered TMI data used in the inversion.

### 5.2.3 Inversion parameters and workflow

The 3D inversion domain was discretized into 25 m x 50 m cells in the inline and crossline directions horizontally, and vertically discretized into 36 cells from 25 m thick at the surface to 300 m at depth. The total depth of the inversion domain was about 4000 m below the surface. The horizontal cell size of 50 m in the crossline direction is adequate due to the 100 m spaced flight lines. The errors used for the error model in the inversion are given in Table III. The final misfit converged to 5% globally and fit the data to the estimated error levels.

*Table III: Estimated error levels in the Kingsview TMI survey used to compute the data weights.*

Datum	Relative Error (%)	Absolute Error (nT)
Filtered TMI	5	0.02

The 3D inversion was run using a homogeneous half-space as the reference and initial model. The stabilizing constraint (stabilizer) used to ensure a robust inversion was the minimum norm of the departure of the model parameters from the reference model and the first derivative in the horizontal and vertical directions.

## 6 Discussion of the results

The 3D inversions results are presented here. This section presents our first observations, and we give examples of what can be done with this data set. This data set is very rich in information, and it should be approached as a model that will continue to be queried for months or years, and new geological and drill hole information becomes available. The 3D model files can be viewed in various ways, from map views, profile views, voxels, and isosurfaces. The interpretation needs to be done with a solid background understanding of the geology of the area and targets. TechnoImaging can aid with this interpretation and work with an area geologist or geophysicist to help get the process started.

### 6.1 VTEM Inversion Results

The VTEM data were inverted to a chargeability and conductivity model. Several methods were used to produce the best final models. Images of these results are shown in Figures 17 – 30.

Figure 17-19 show an overview of the recovered conductivity models at depths of 20, 150, and 350 meters below the surface, respectively. The conductivity in the survey area varies from around 1 S/m (1 Ohm-m) to 1e-4 S/m (10,000 Ohm-m), although most of the terrain was quite resistive (>1000 Ohm-m). The images show conductive and resistive lineaments running roughly northwest to southeast. Some mild line stripping is also apparent in the figures, especially in the northwest. This is due to uneven sensitivities from the 100 m flight lines. The most obvious feature in the data is the MPD Zinc Copper showing. Another similar but smaller and weaker anomaly is seen at 711000 mE and 5339000 mN. This is shown in more detail in Figure 20. It is nearly a single line anomaly, but neighboring lines also show a small response from this target, and it is not noise.

Figure 21 shows the conductivity at a depth of 100 m below the surface on a compressed color

scale from  $2e-3$  S/m to  $1e-4$  S/m. The geologic units at 100 m depth can be inferred from this map.

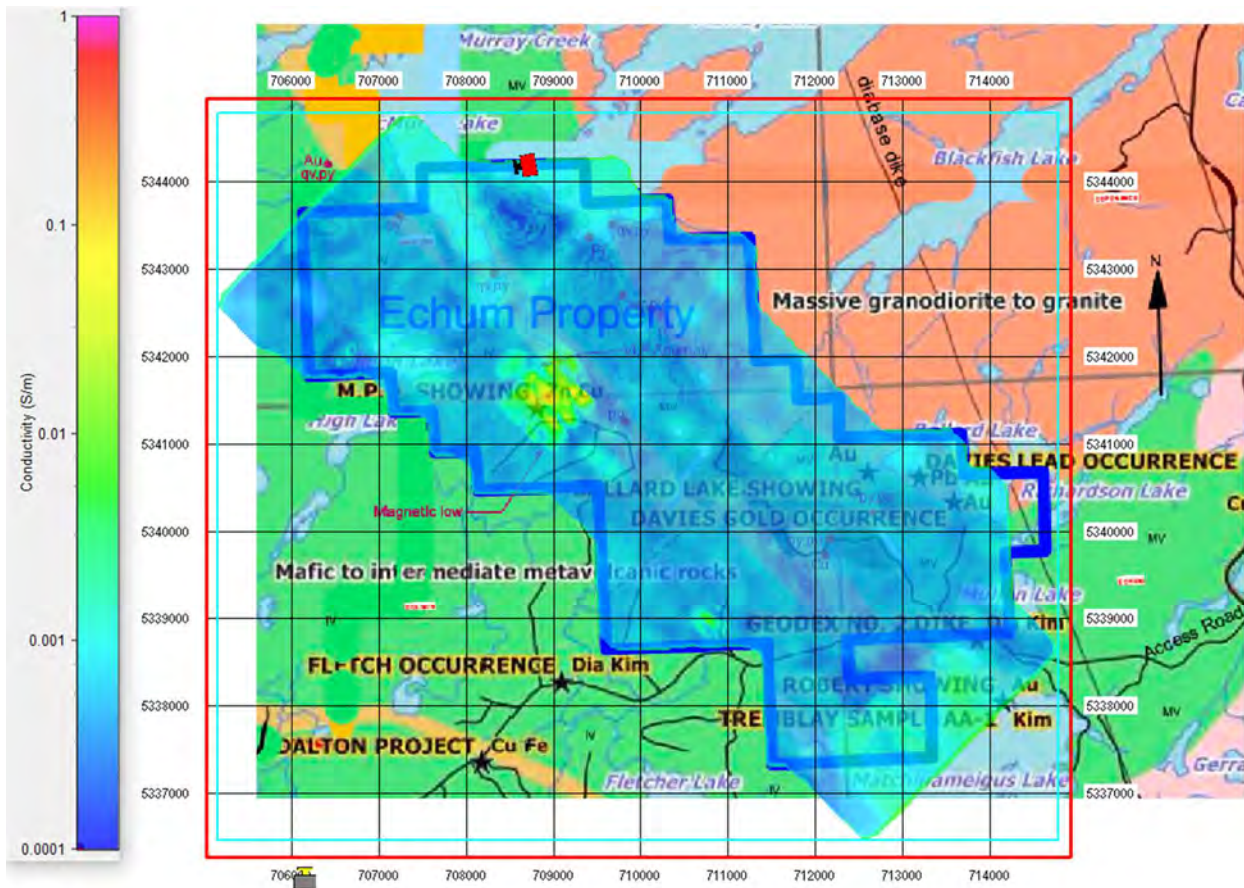


Figure 17. Conductivity inversion results at a depth of 20 m below the surface.



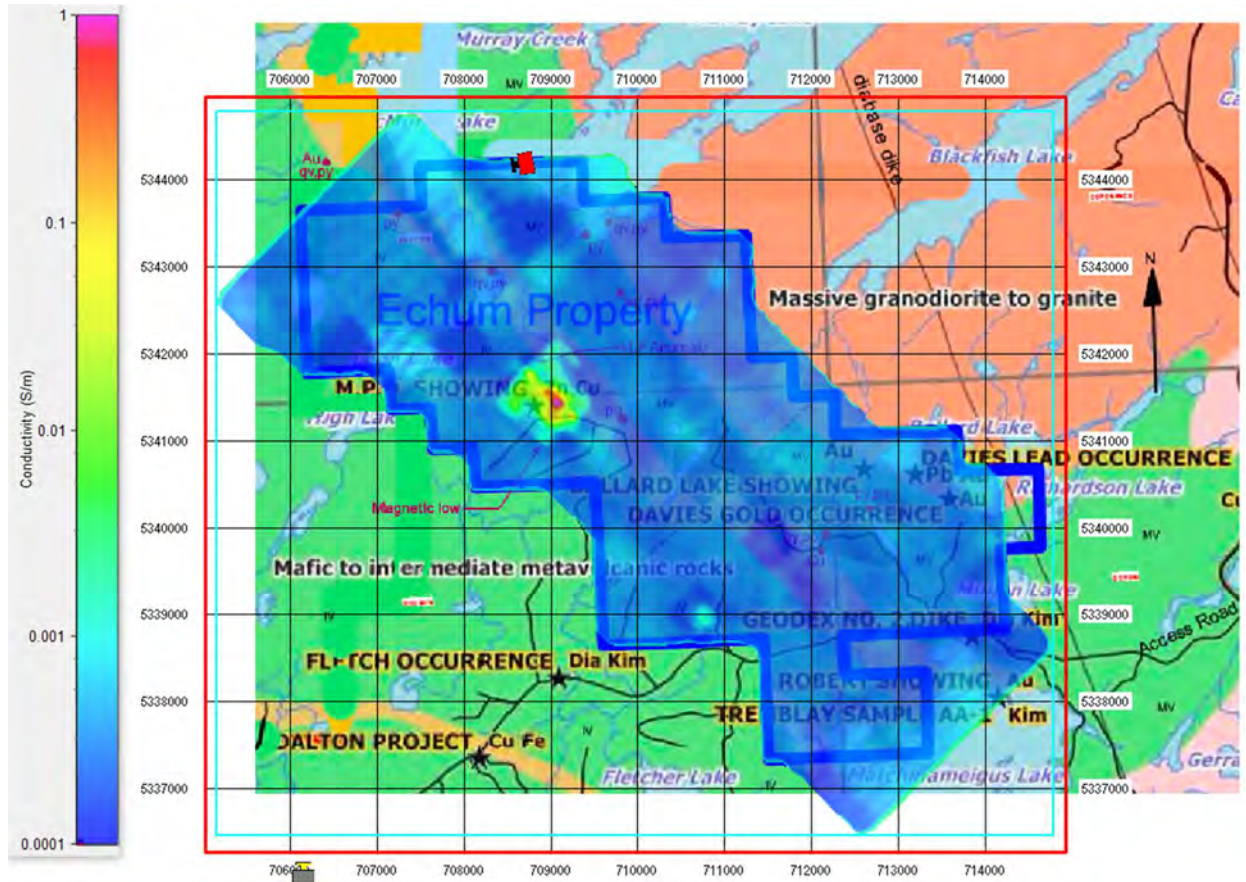


Figure 18. Conductivity inversion results at a depth of 150 m below the surface. Note the known Zinc-Copper deposition clearly imaged at 709000 mE and 5341500 mN.

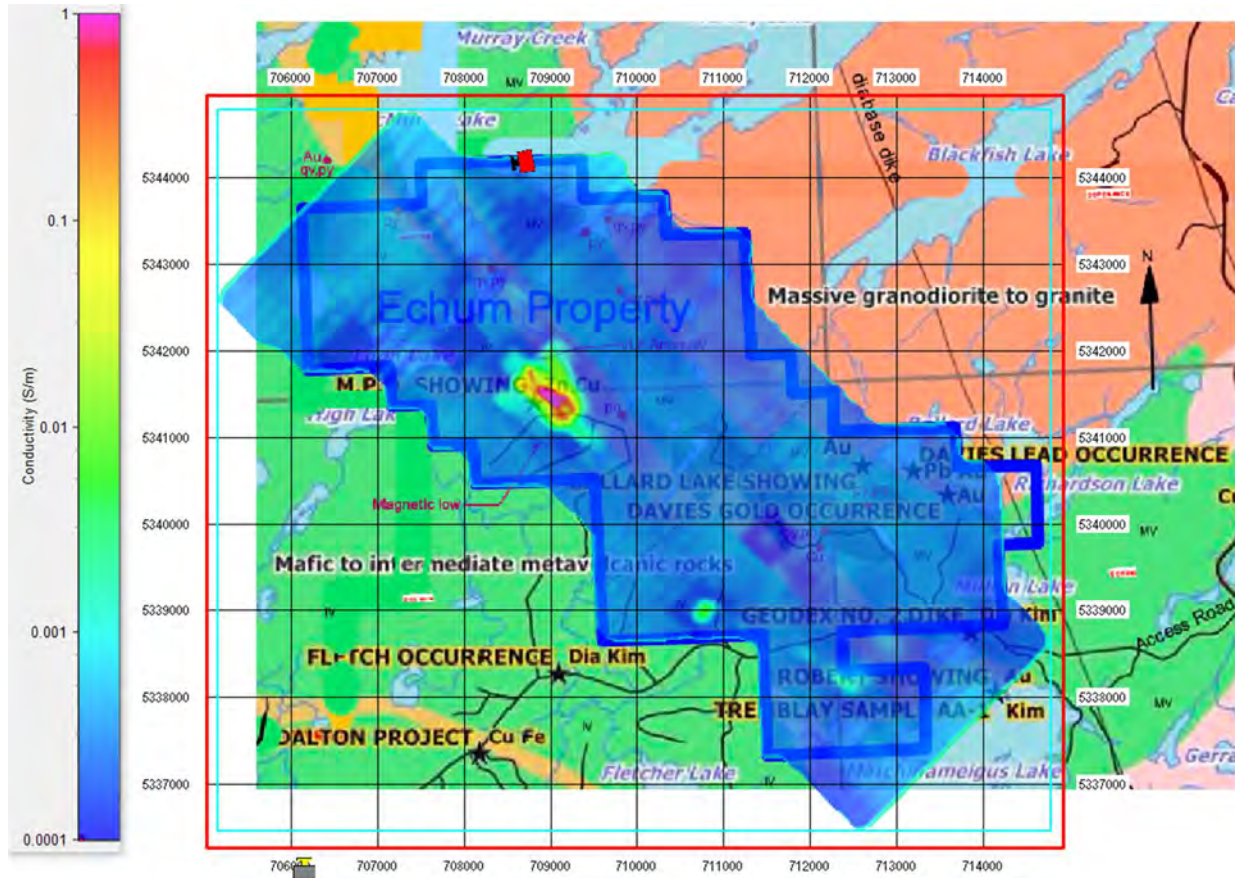


Figure 19. Conductivity inversion results at a depth of 350 m below the surface. Note the known Zinc-Copper deposition clearly imaged as a strong conductor at 709000 mE and 5341500 mN. Another weaker and smaller, but very similar conductor, is shown at 711000 mE and 5339000 mN.



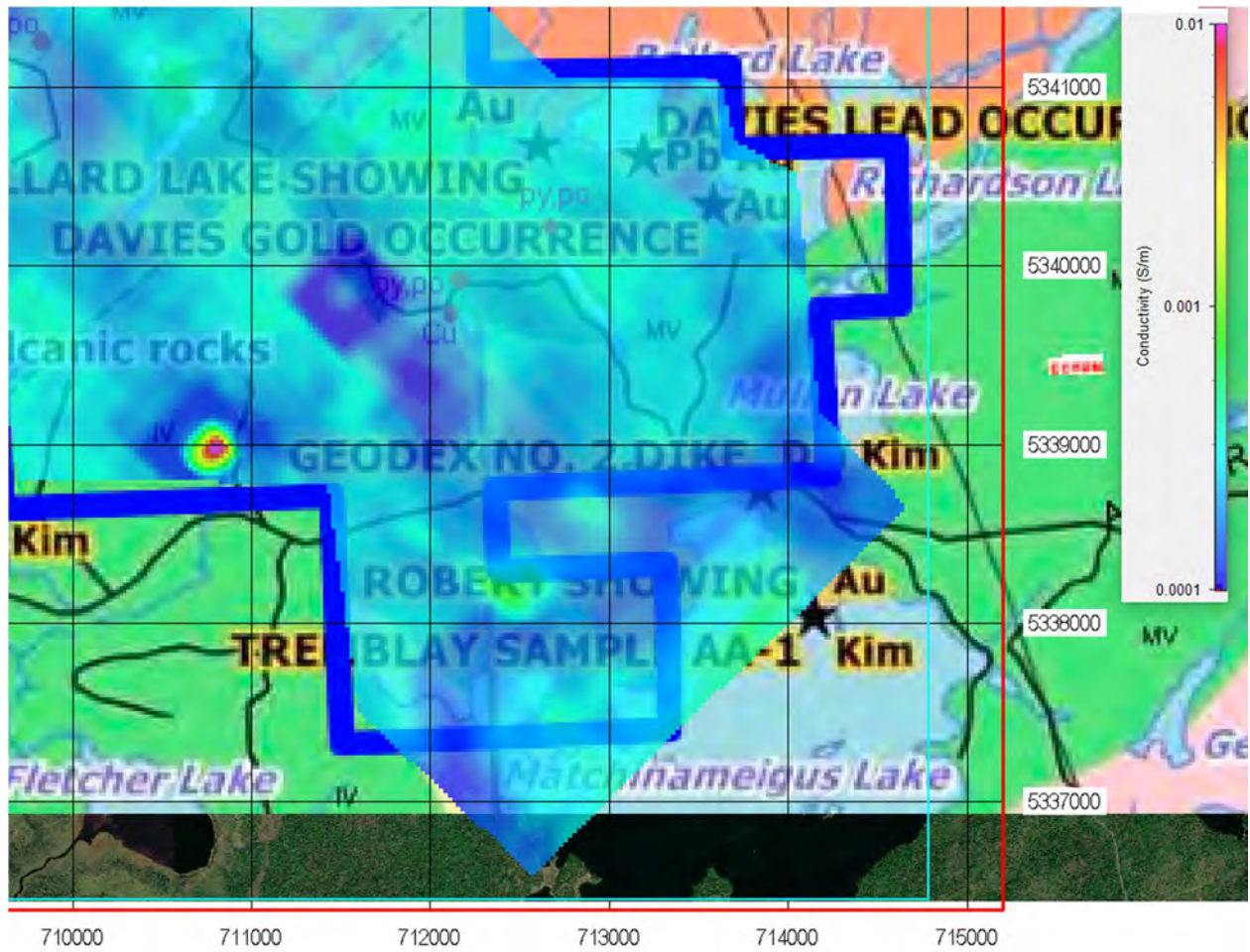


Figure 20. Conductivity inversion results at a depth of 250 m below the surface. The smaller unmapped conductive feature is shown at 711000 mE and 5339000 mN.

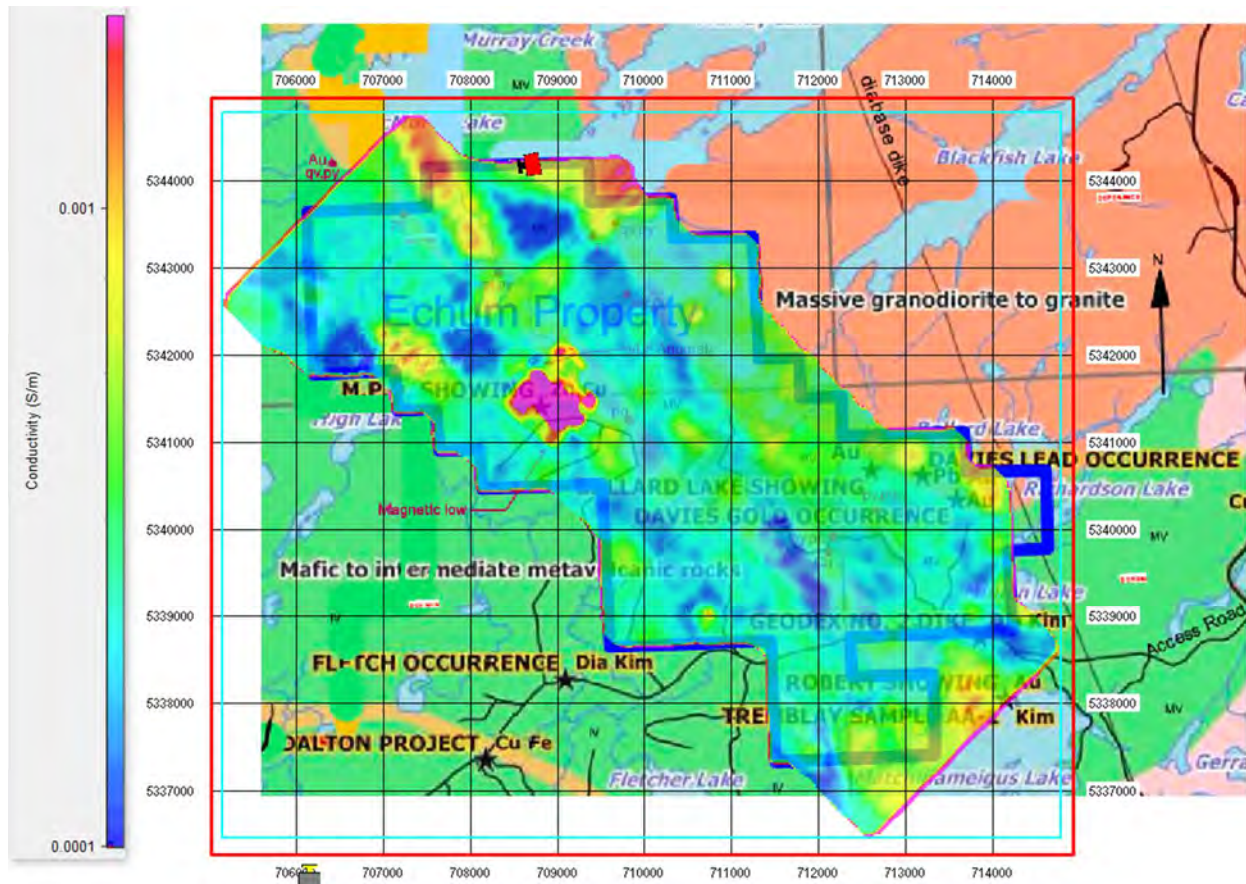


Figure 21. Conductivity inversion results on a compressed color scale to bring out details at a depth of 100 m below the surface. Trends in the conductivity can be clearly seen which relative to the geology.

Figures 22 and 23 show the MPD shown in detail. Both vertical planes of conductivity, plus isosurfaces at a constant conductivity are shown in the figures. Figure 22 shows the body with a isosurface at 0.1 S/m, and Figure 23 shows the same view but with a surface of 0.5 S/m depicting the more conductive core of the body. The geometry of the body can be clearly seen in these figures.



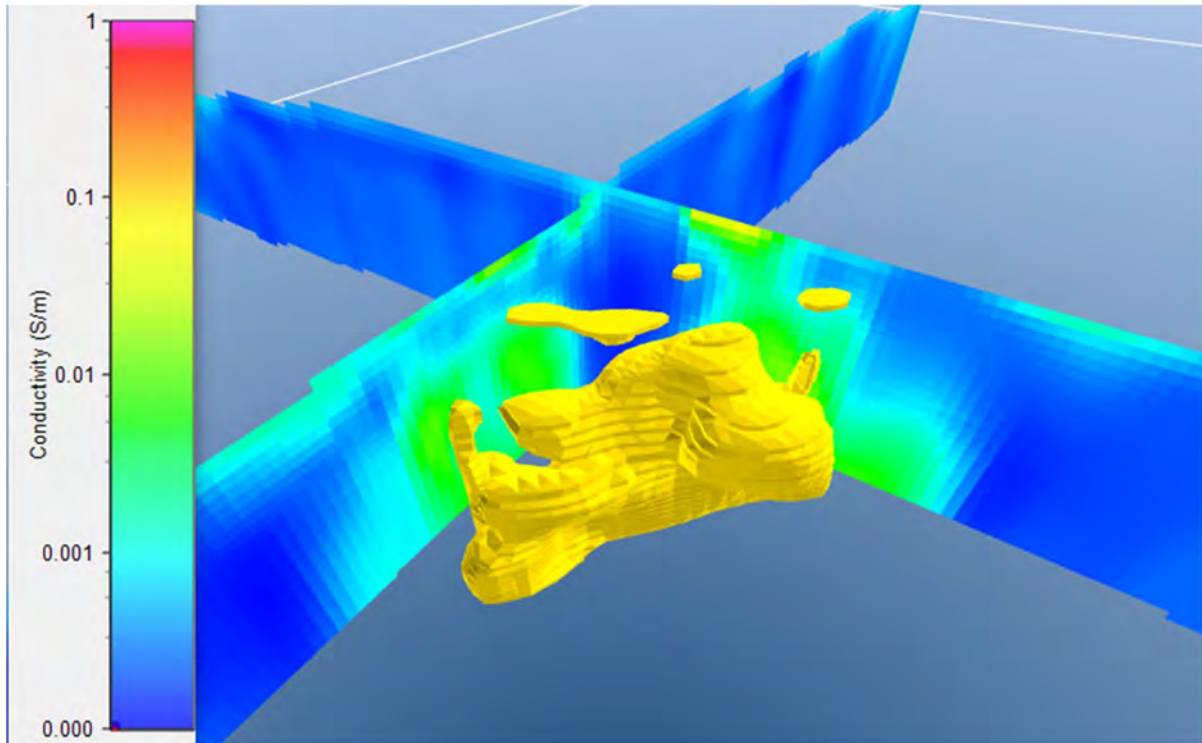


Figure 22. Detail of Zinc-Copper mineralization looking northeast. The isosurface is shown at 0.1 S/m. The body is about 600 m in length and 100 m below the surface. The full section depth extent is about 500 m. There is no vertical exaggeration.

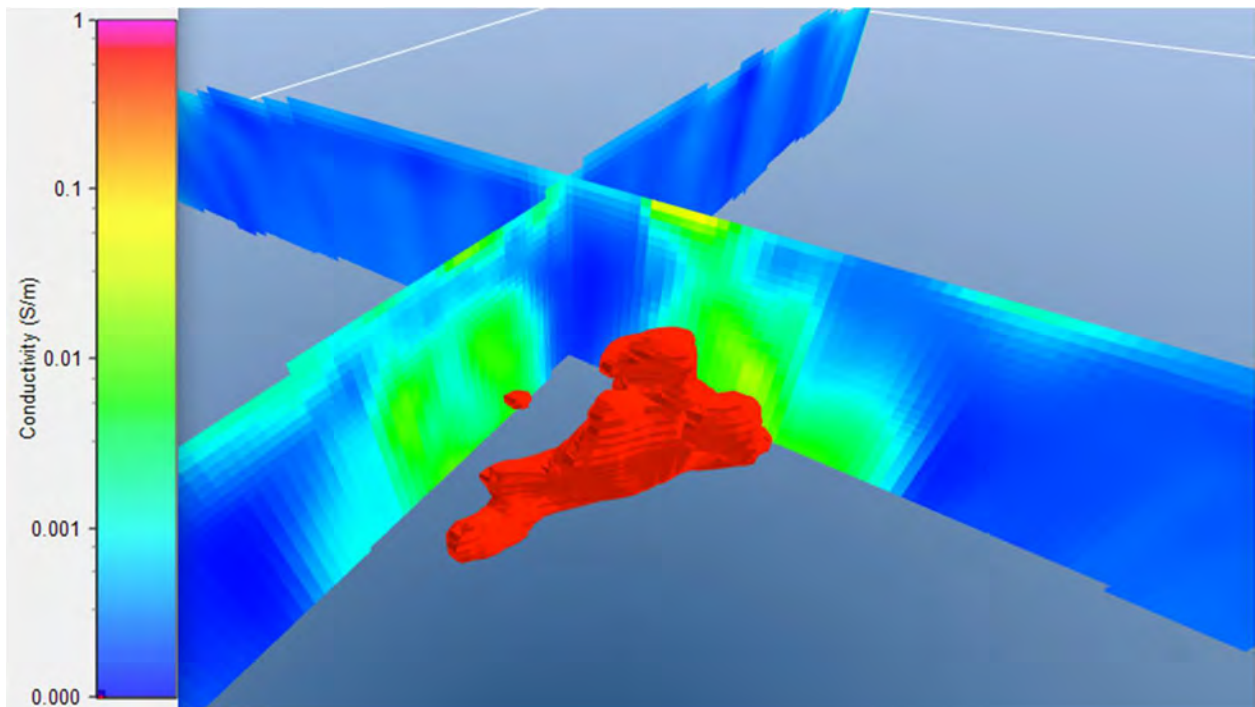


Figure 23. Detail of Zinc Copper mineralization looking northeast. The isosurface is shown at 0.5 S/m. At this cutoff the body is about 600 m in length and 150 m below the surface.



### 6.1.1 3D Versus 1D Inversion

Figures 24 and 25 show the MPD body in profile view. The top panel of both figures shows observed and predicted inline X-components of the dB/dt data. The observed data are shown as solid lines with circles, while the predicted data are shown as dotted lines. The lower panel show the recovered conductivity model from inversion.

Figure 24 show the conductivity model recovered from 1D inversion. As described in the inversion theory section, this approximation assumes that the conductivity structure is simple layered earth under each transmitter-receiver pair. Thus each layer extends horizontally to infinity for modeling purposes. The inversion is run, and a best fitting layered earth is found for each sounding location; then each of these 1D models is then placed under the transmitter-receiver pair and gridded into a 3D model. The results are typically quite diffuse, low resolution, and can have artifacts which make them very inaccurate.

The data shown in Figure 24 uses full 3D modeling on the 1D inversion results to produce the data observed over the body. In Figure 24, it is clear the model data do not reproduce the observed data at all, which means the body is incorrect.

Contrast this with Figure 25, which shows a profile through the MPD body as recovered from full 3D inversion. Again, the results are much sharper and with higher conductivity contrast. The data fit from the inversion is also very good, which shows that the recovered body is much more representative of the subsurface than the image produced by the 1D inversion, shown in Figure 24.

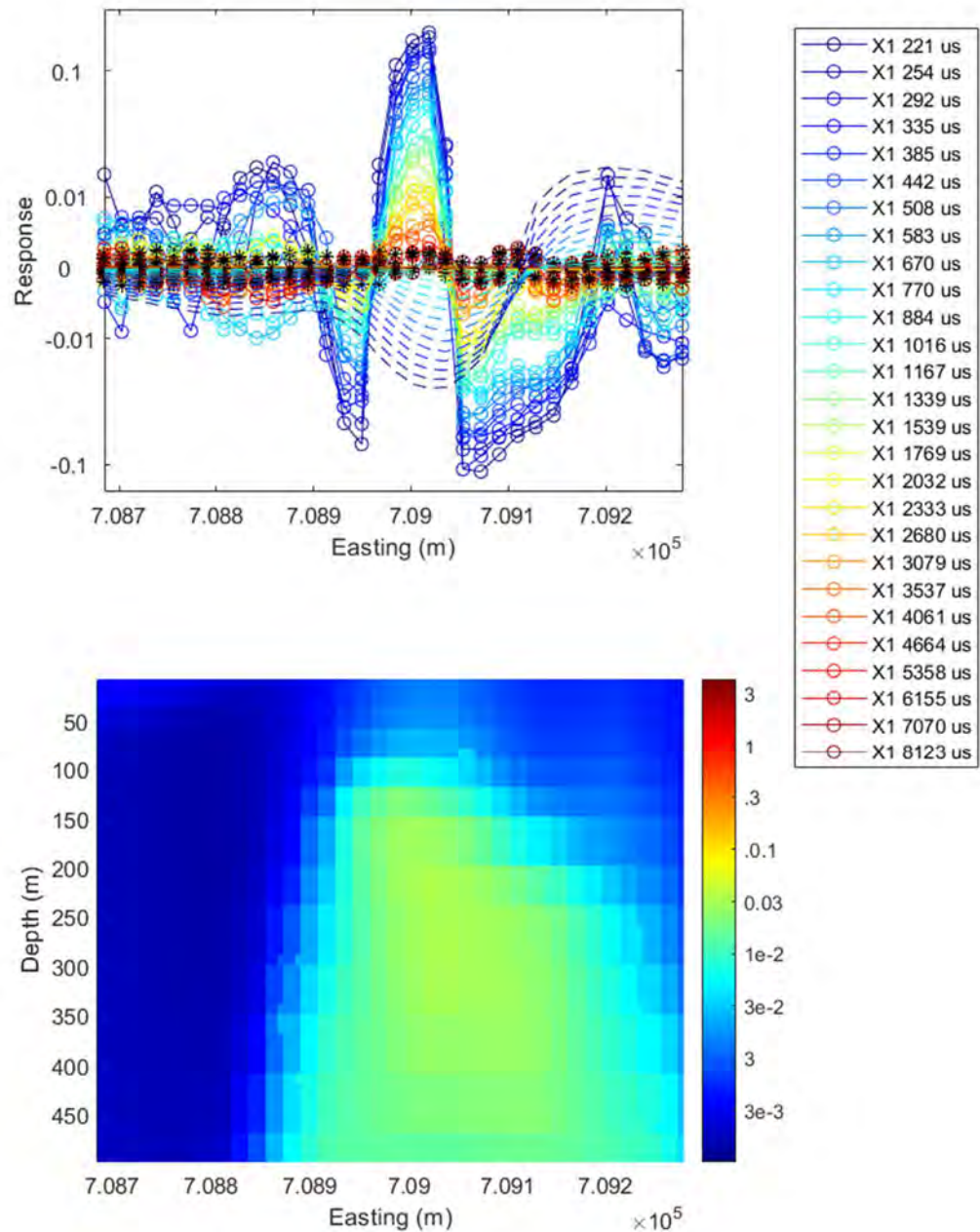


Figure 24. Example of X-component data fit (top panel) and recovered conductivity in S/m (bottom panel) along L1360 from full 1D inversion. The observed data are shown with the solid lines and circles, while the predicted data are shown with dotted lines. The data are modeled in full 3D from the 1D inversion result derived from the Z-component data. The fit is very poor, indicating the recovered model from 1D does not accurately represent the subsurface. For steeply dipping conductors and confined conductors such as these, the results from the 1D inversion are useful only as a starting model for the full 3D inversion.

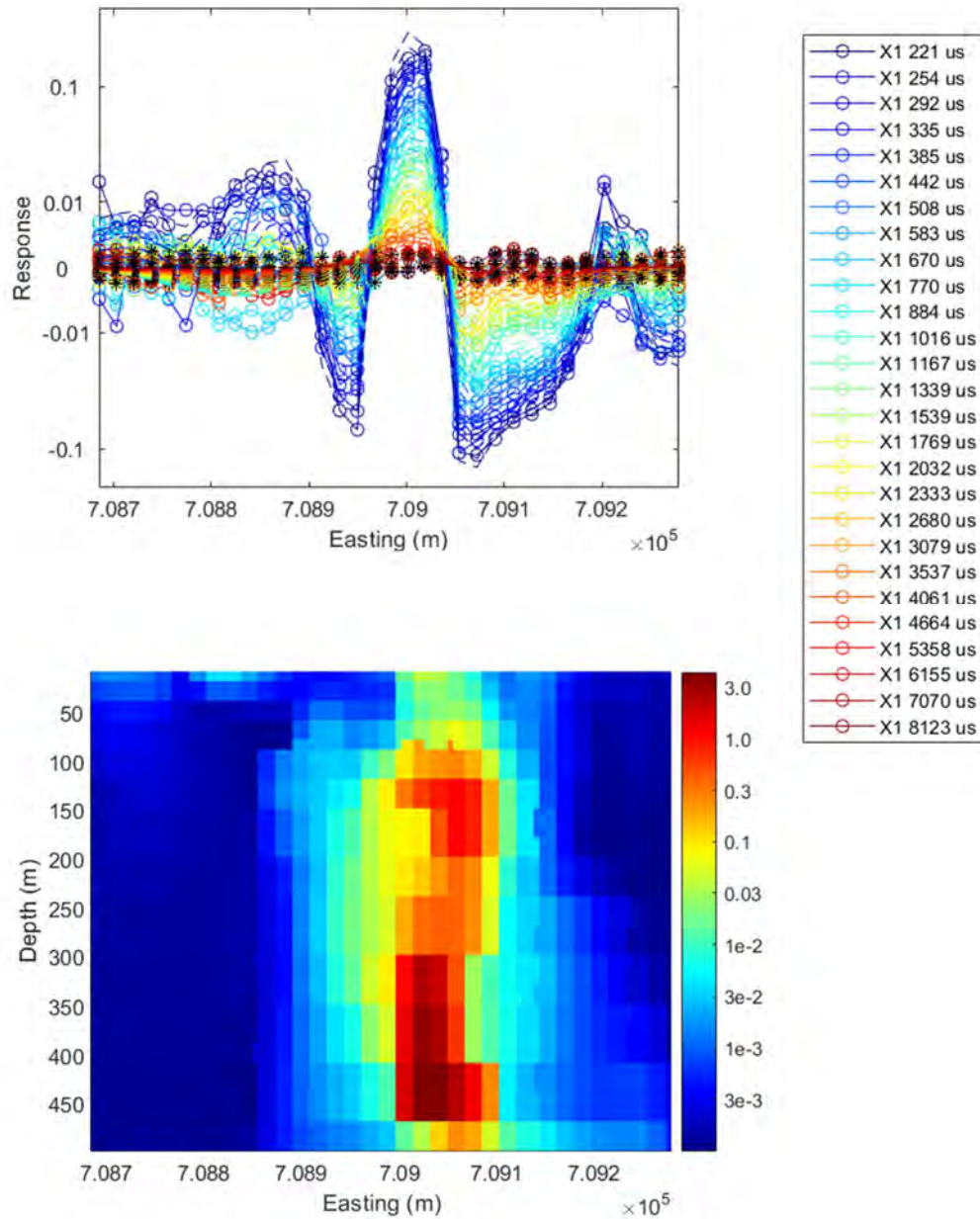


Figure 25. Example of X-component data fit (top panel) and recovered conductivity in S/m (bottom panel) along L1360 from full 3D inversion. The observed data are shown with the solid lines and circles, while the predicted data are shown with dotted lines. The fit is excellent.

### 6.1.2 Chargeability Inversion Results

The airborne derived chargeability results are illustrated here. The chargeability from the airborne inversion results typically do not and should not necessarily match with ground-based IP



measurements. We believe this is primarily because of the greatly different bandwidth of ground-based systems (~1/4 Hz) and airborne systems (30 Hz). This gives two orders of magnitude difference in the time constants of media that they image. However the information presented in the two is complementary, and the AEM systems provide useful chargeability measurements.

Images of the 3D chargeability distribution are shown in Figures 26-30. In the survey area, most of the chargeability anomalies align with lakes. The large conductors are shown as chargeability lows, largely because the coupled EM and IP responses lead the IP response to be covered in very conductive areas.

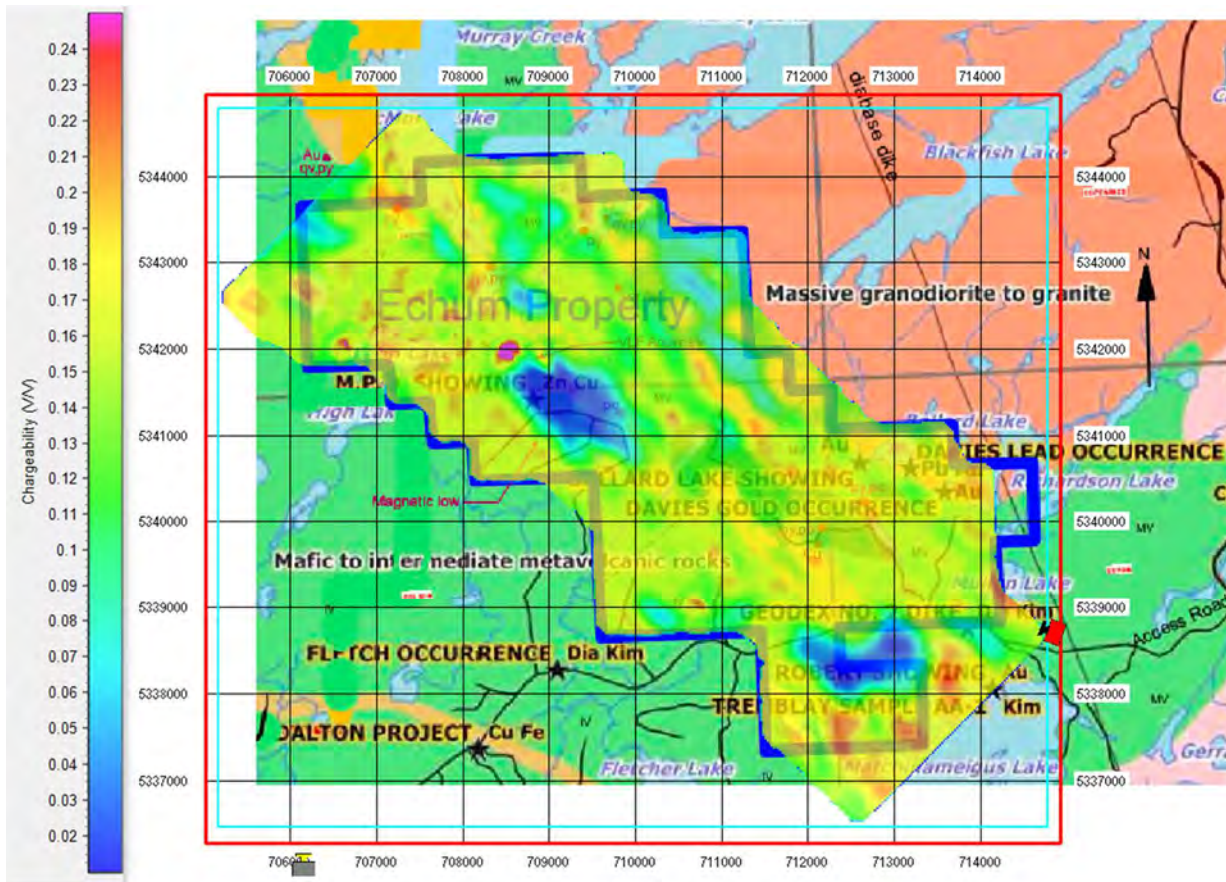


Figure 26. Chargeability inversion results at a depth of 20 m below the surface. Most of the chargeability anomalies are due to lake bottom sediments. Anomalies not associated with lakes are of interest.

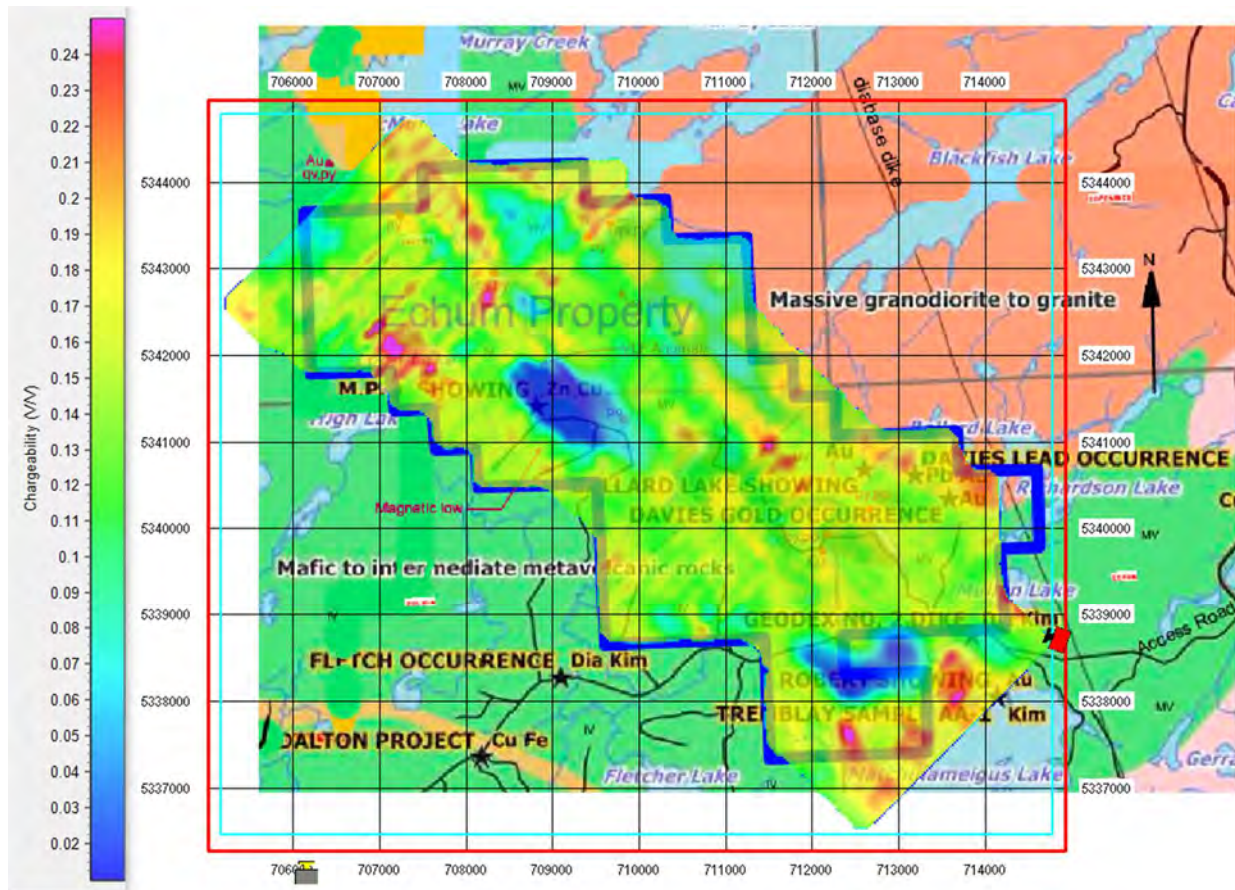


Figure 27. Chargeability inversion results at a depth of 150 m below the surface.

Figure 28 shows a detailed area near the Ballard Lake and Davies showing. The airborne-based chargeability in this area highlights lake bottom sediments, and not the ground IP anomalies shown. However, the AEM chargeability is mapping petrophysical properties and can be used for mapping. Figures 29 and 30 show chargeability overlain on satellite imagery and a geologic map. Figure 29 shows that most of the chargeability corresponds to lake bottom sediments, but areas such as around 711500 mE and 5341000 mN show chargeability that is not associated with a lake and is of interest. Also, there is an obvious chargeability low relative to background depicted in dark blue to the southeast that warrants further investigation.

Note that this anomaly corresponds to a major fault and contact between the mafic volcanics and granodiorite (Figure 30).



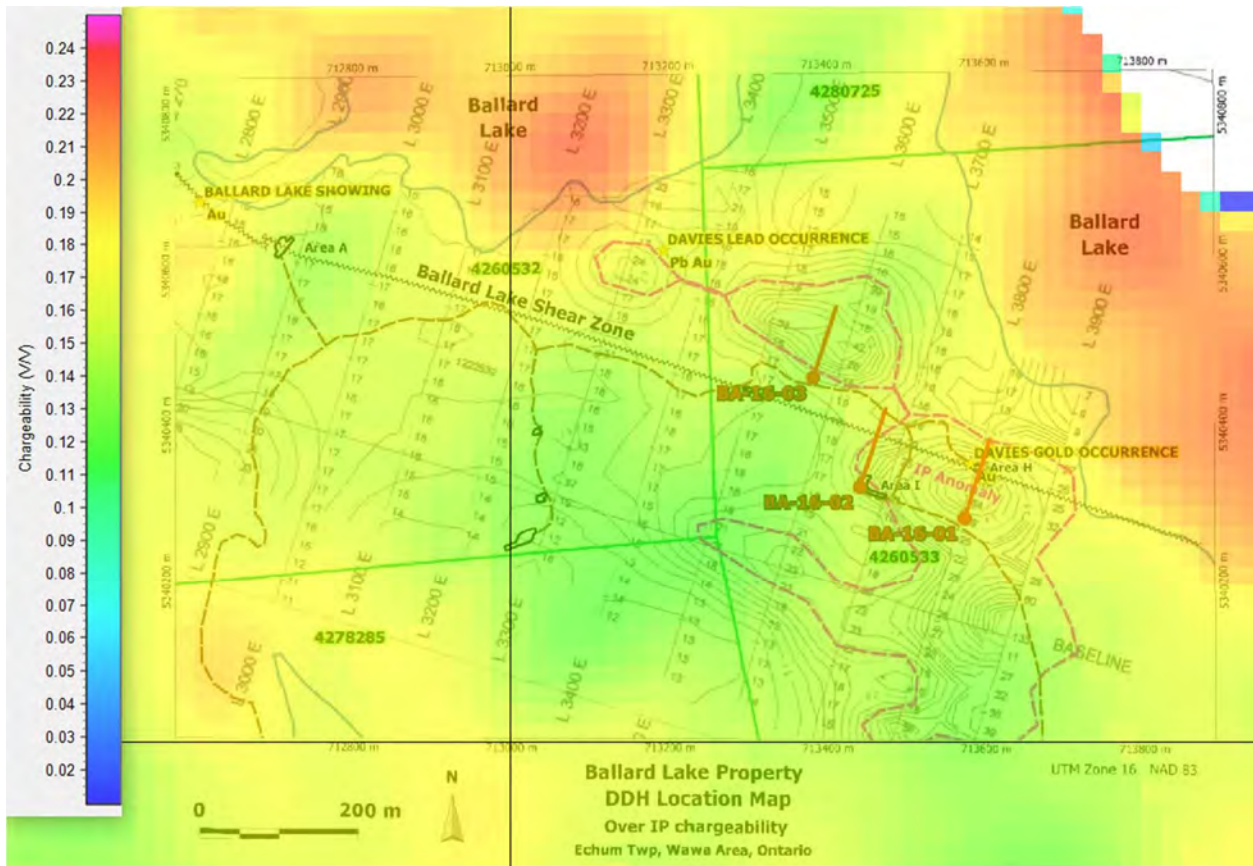


Figure 28. Airborne derived chargeability results overlain on ground chargeability. We see an excellent correlation of the airborne chargeability with lakes, as the sediment bottoms are likely filled with clay and respond well to the time constants that fall within the airborne bandwidth.



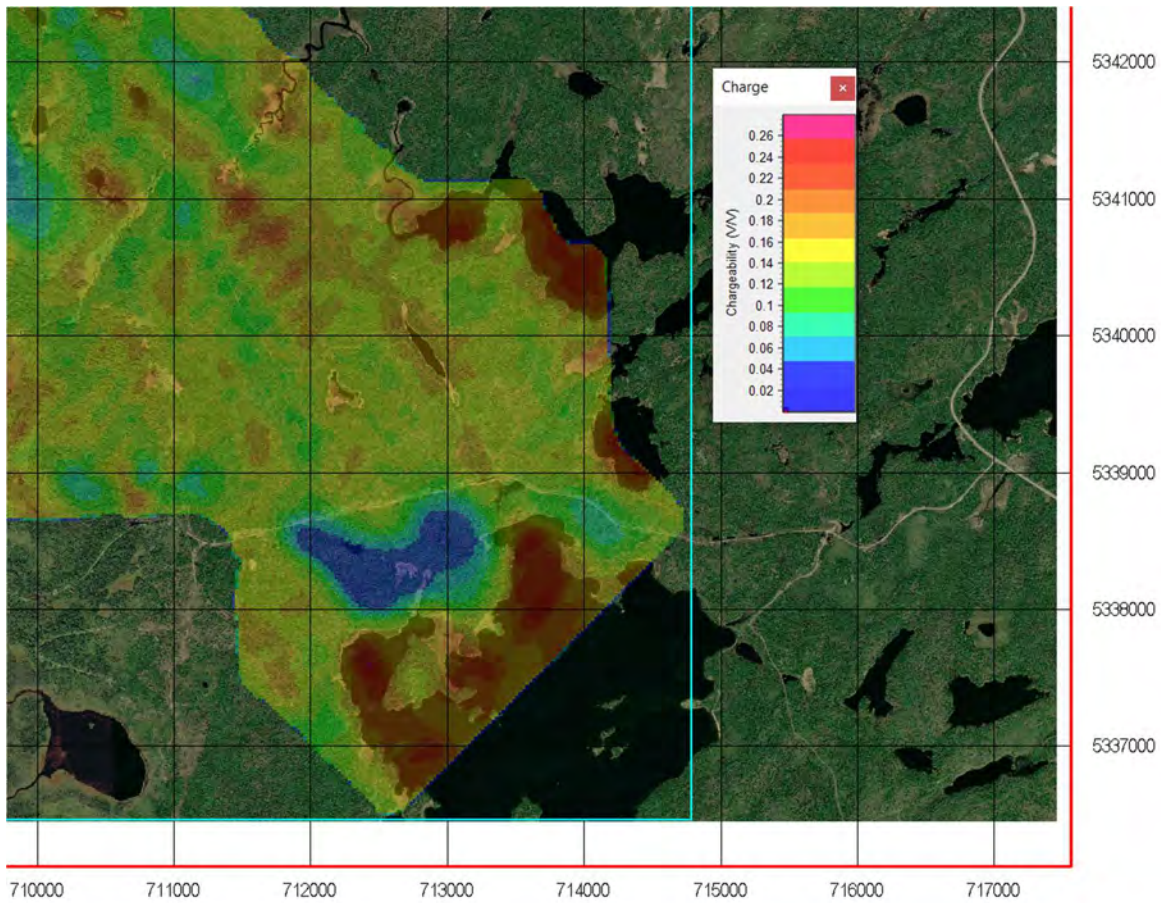


Figure 29. Chargeability at a depth of 150 m overlain on satellite imagery. The correlation between the lakes and the chargeability anomalies are apparent. However, a few anomalies, notable at 711500 mE and 5341000 mN show chargeability that is not associated with a lake. The cause of the obvious chargeability low relative to background in the southeast is unknown but warrants further investigation.

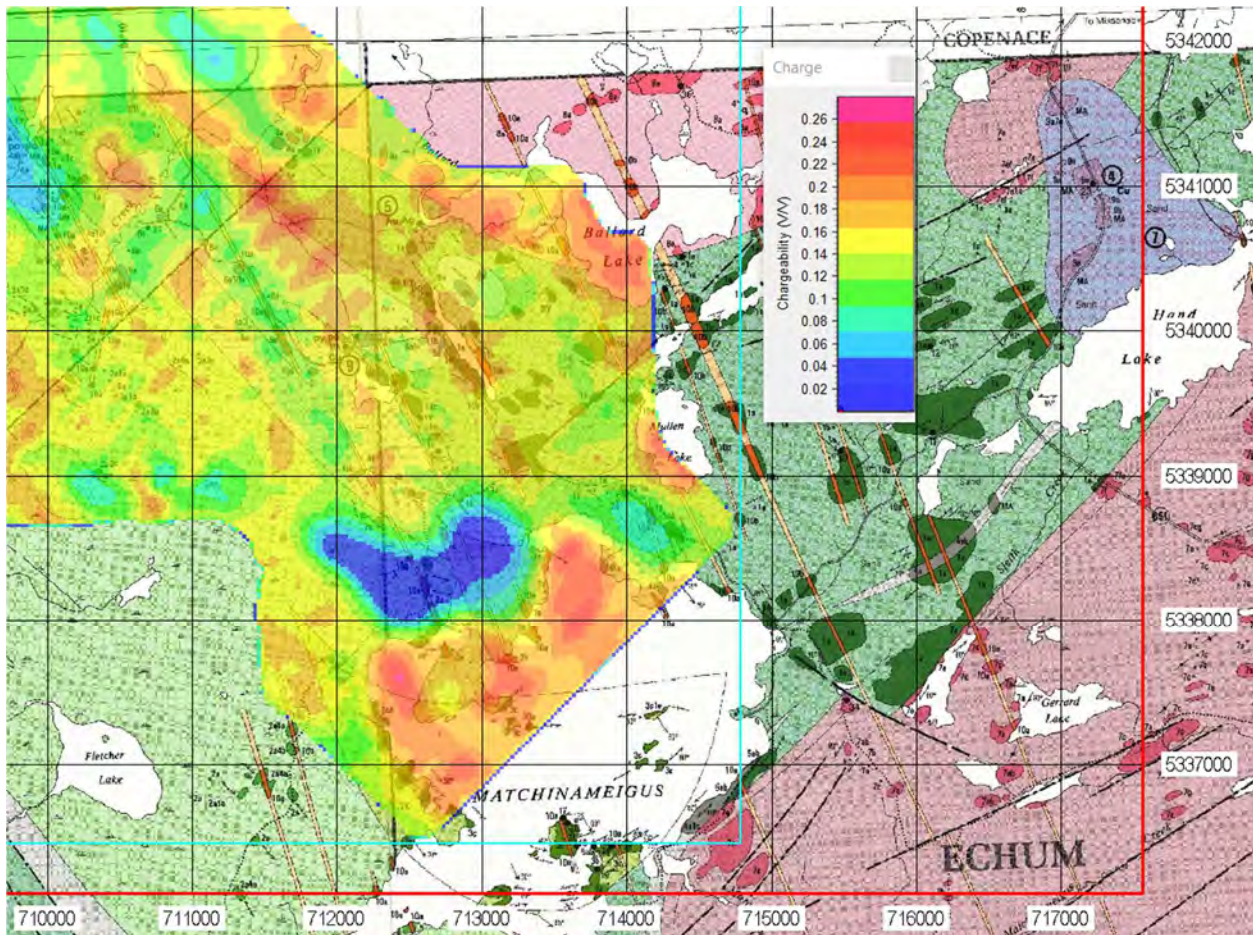


Figure 30. Chargeability at a depth of 150 m overlain on a geologic map. The chargeability anomaly at 711500 mE and 5341000 mN corresponds with a major fault and contact between the mafic volcanics and granodiorite.

## 6.2 TMI Inversion Results

The TMI data were inverted to both susceptibility and magnetic vector models. The susceptibility model is a standard product but cannot take into account remanent magnetization. The magnetic vector model considers both susceptibility and remanent magnetization and is the preferred product to study. However, the three vector components are more challenging to visualize than one scalar value. Figures 31 to 38 give overviews of the recovered magnetic models at depths of 20 m (near-surface lithologies) and 600 m (deep-seated structures). Structures, cross-cutting faults, and other areas of interest are shown in these images.

A magnetic low, which is imaged in the data, is clearly shown in Figure 33. This has the potential to be a kimberlite-like response. An isosurface view of this anomaly is shown in Figure 39, clearly detailing the geometry of the body.

In Figure 40, a detailed view of the z component of the magnetic vector in the southeast of the survey. Note the excellent correlation of the vertical component of magnetization with the copper and pyrite and pyrrhotite mineralization near 712000 mE and 5340000 mN. Similar responses are shown nearby, which, given a favorable geological setting, could be worth follow up work.



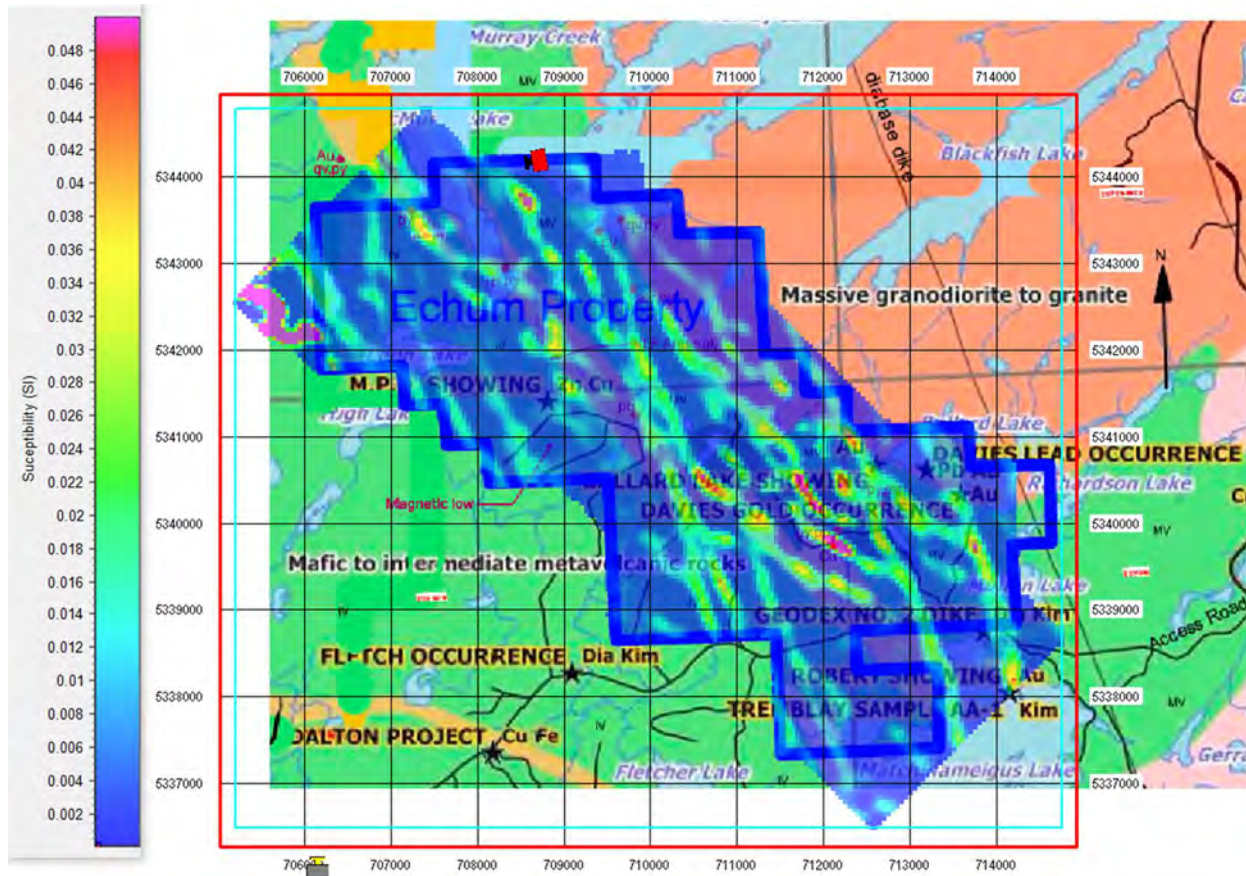


Figure 31. Horizontal section of magnetic susceptibility 20 m below the surface

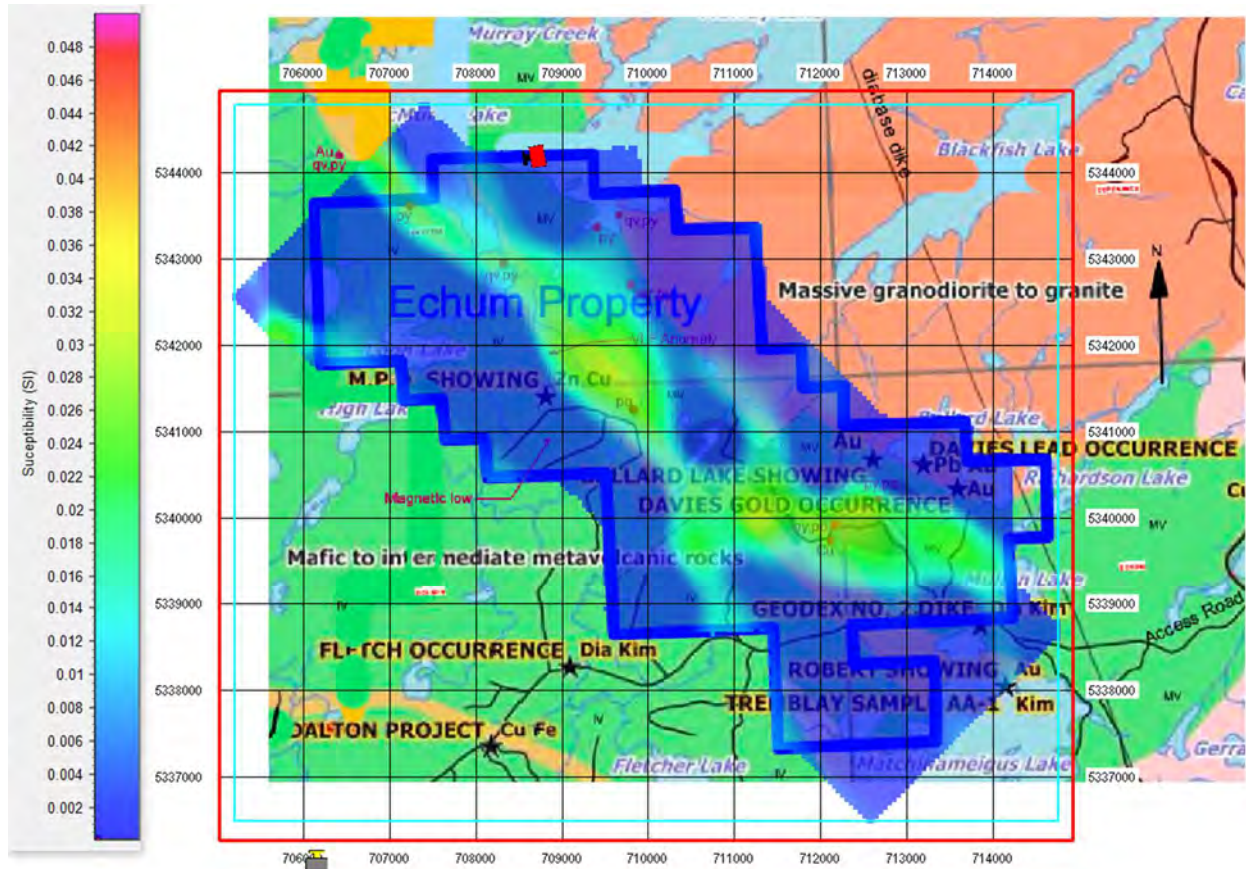


Figure 32. Horizontal section of magnetic susceptibility 600 m below the surface. The Davies and Ballard Lake showings are just to the northern boundary of the susceptibility high.



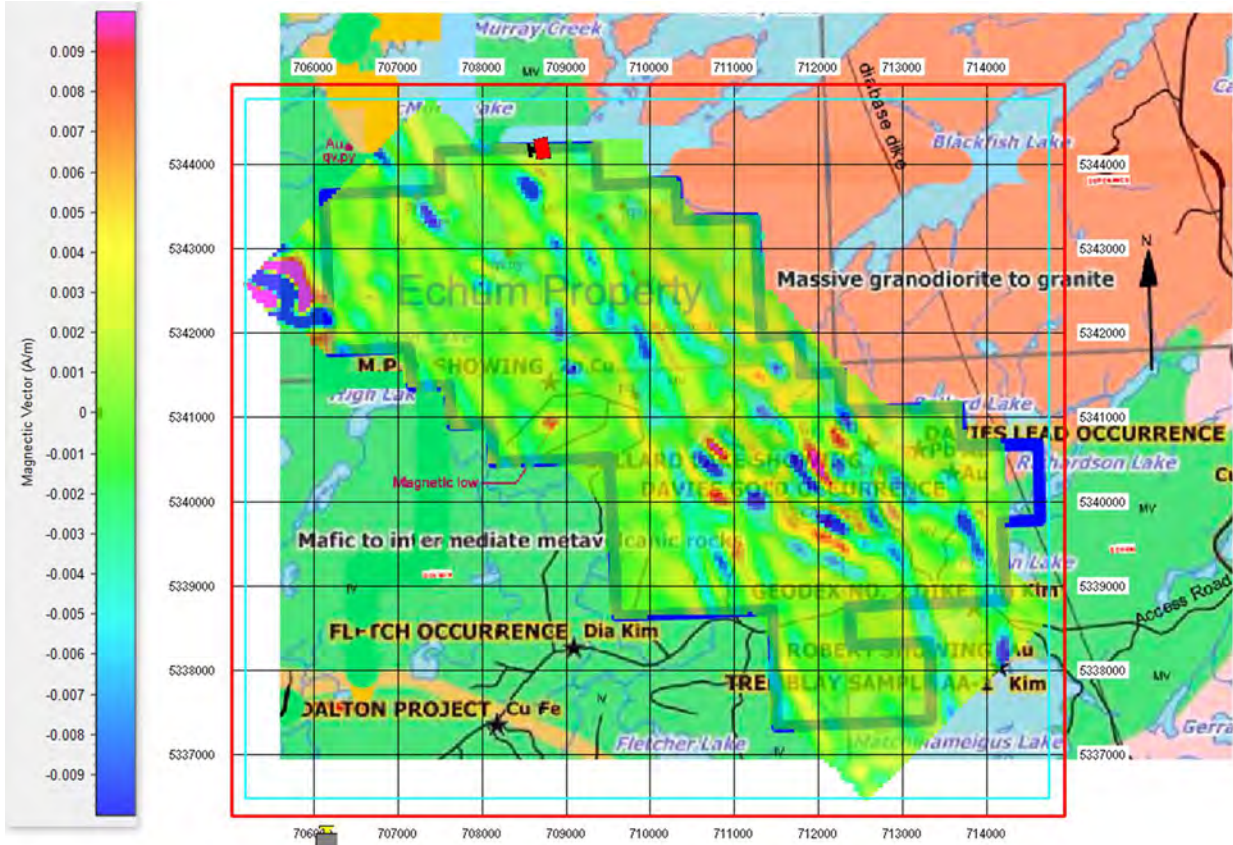


Figure 33. Horizontal section of the vertical (Z) component of the magnetic vector at 20 m below the surface. Just south of the MDP showing is a positive anomaly (~709000 mE, 5341000mN) that could be a kimberlite. This was noted as a magnetic low on the base map.

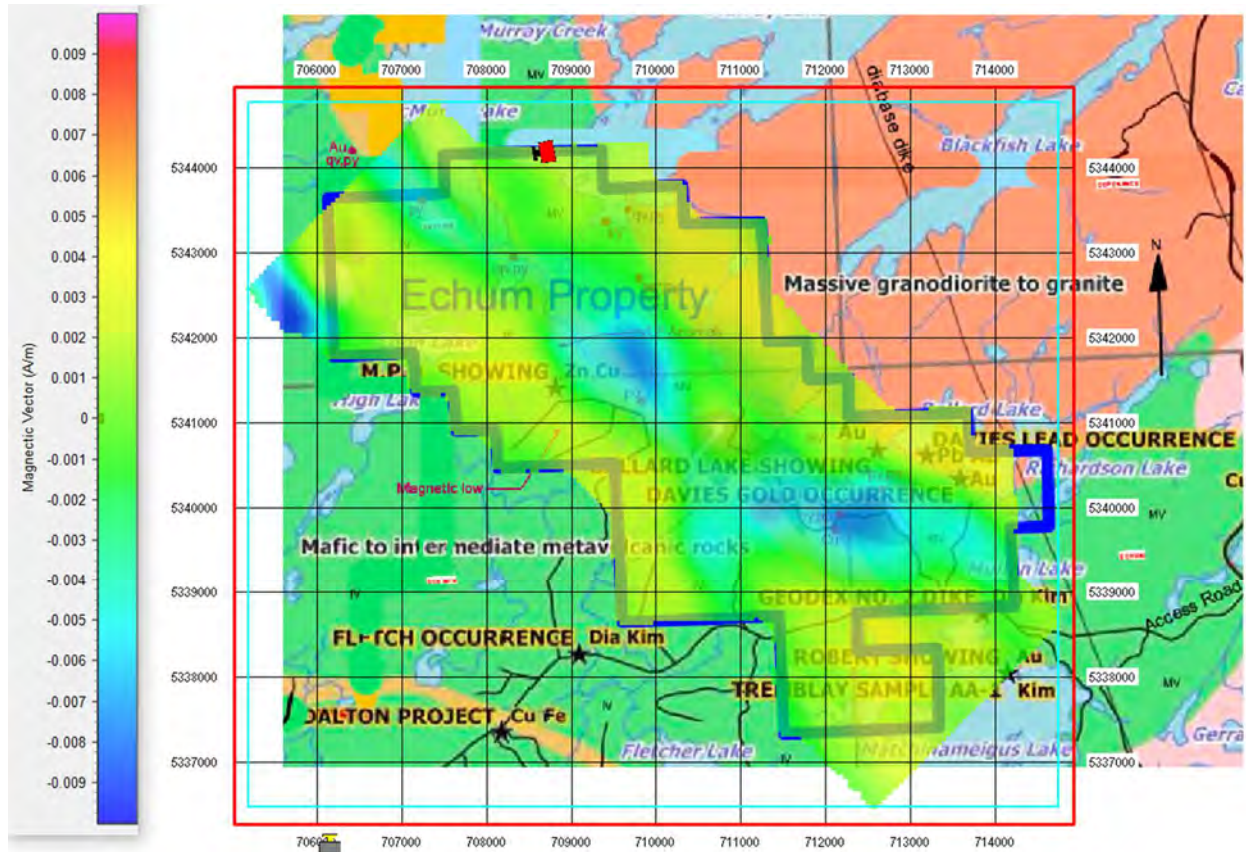


Figure 34. Horizontal section of the vertical (Z) component of the magnetic vector at 600 m below the surface.



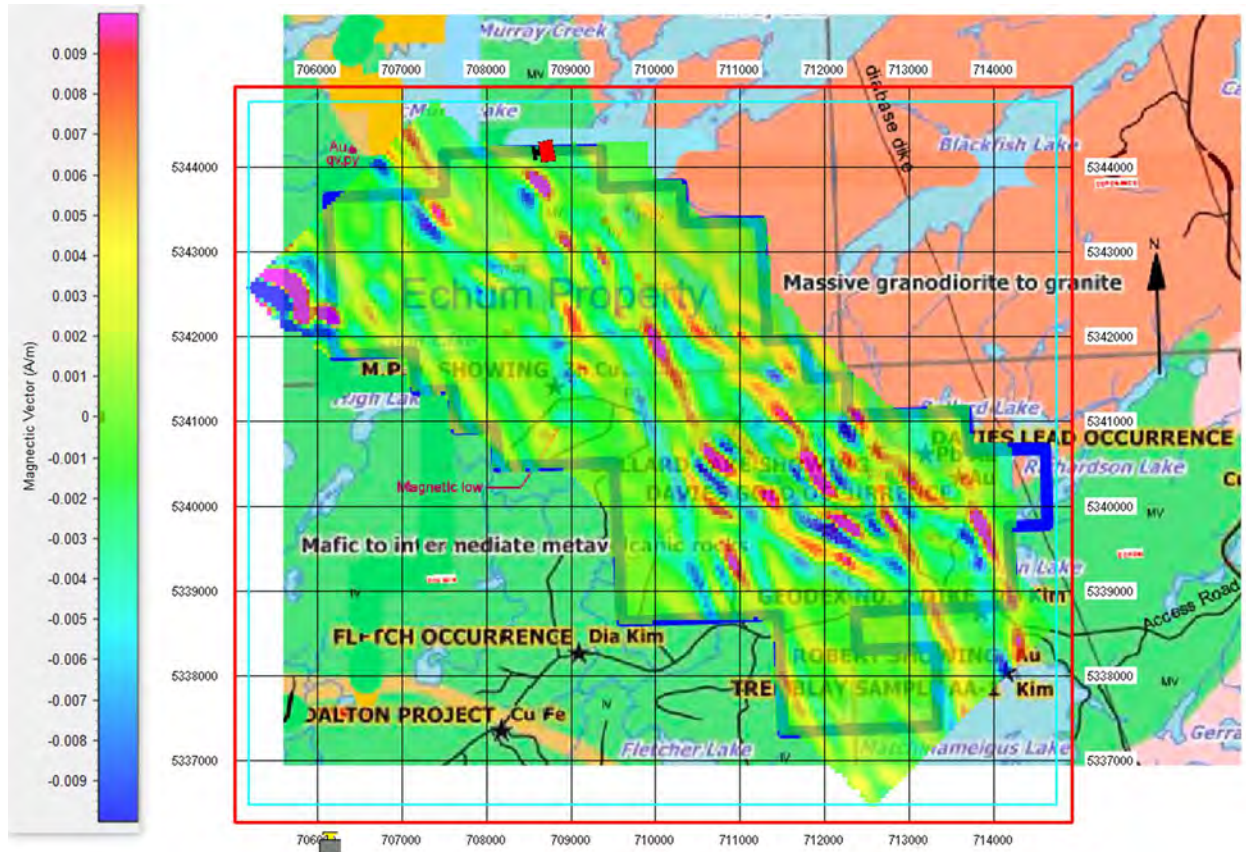


Figure 35. Horizontal section of the easting (X) component of the magnetic vector at 20 m below the surface.

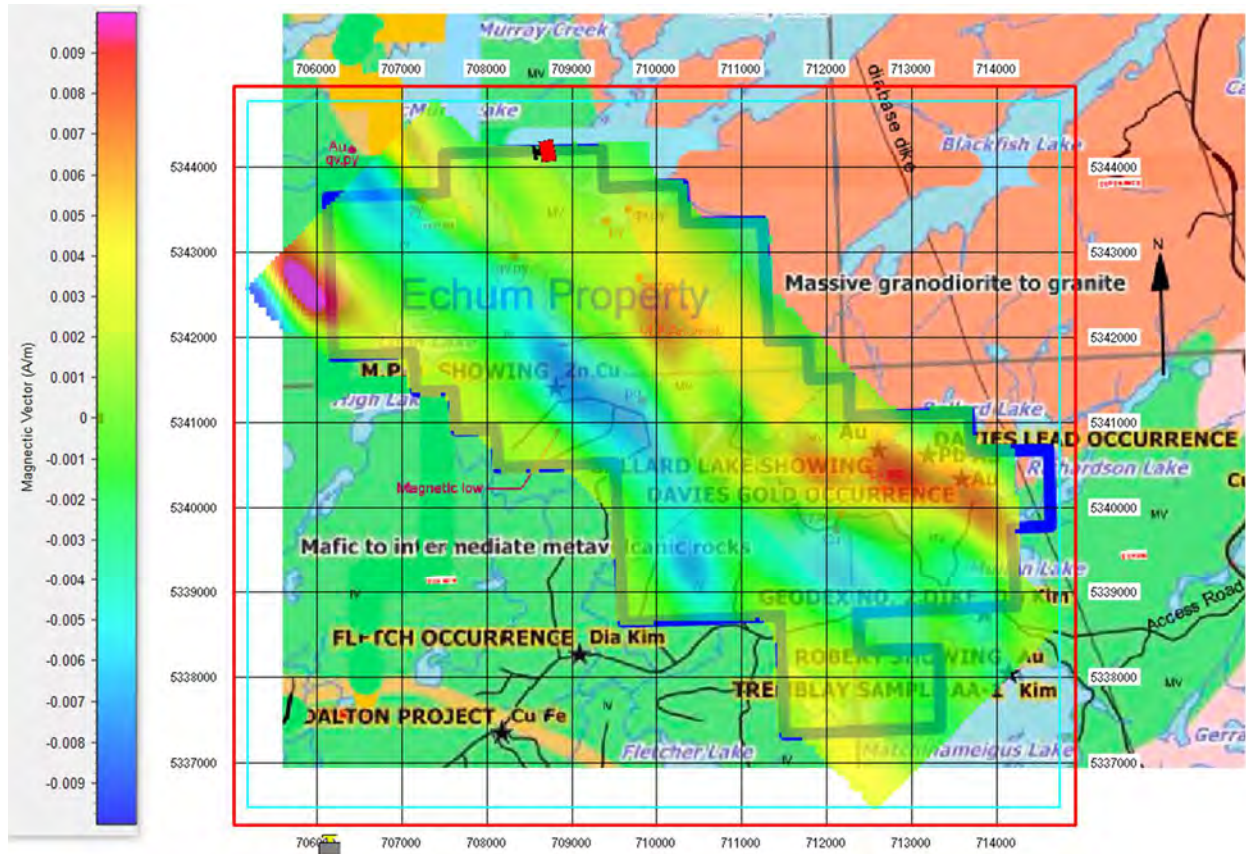


Figure 36. Horizontal section of the easting (X) component of the magnetic vector at 600 m below the surface.



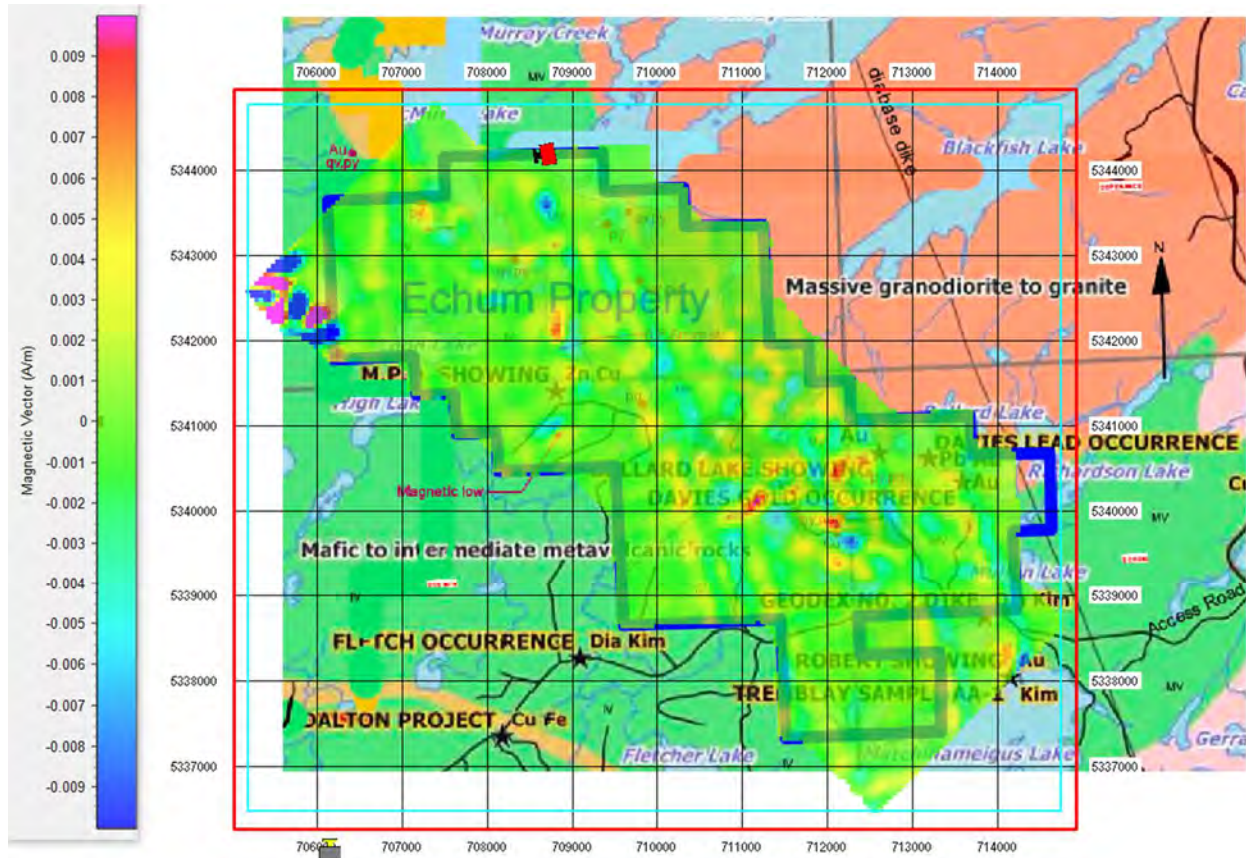


Figure 37. Horizontal section of the northing (Y) component of the magnetic vector at 20 m below the surface.

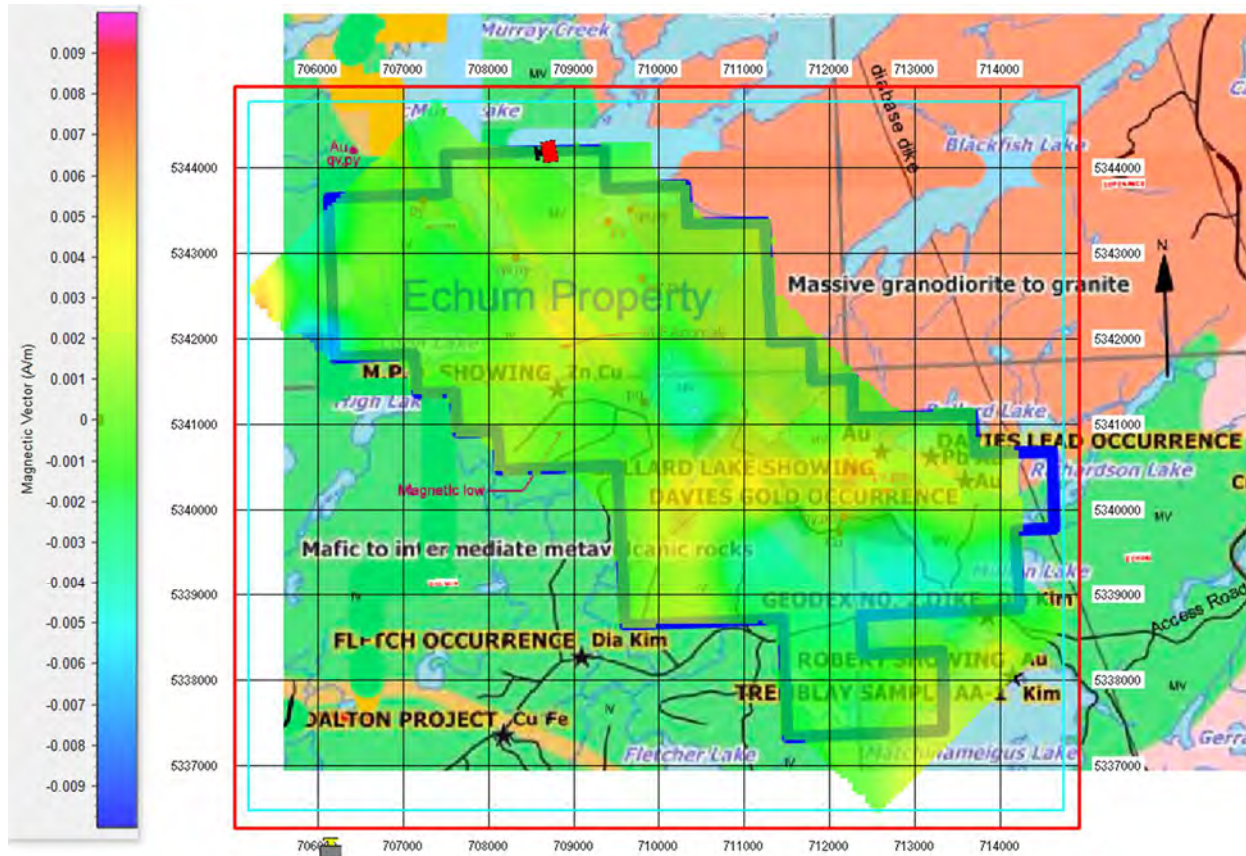


Figure 38. Horizontal section of the northing (Y) component of the magnetic vector at 600 m below the surface.

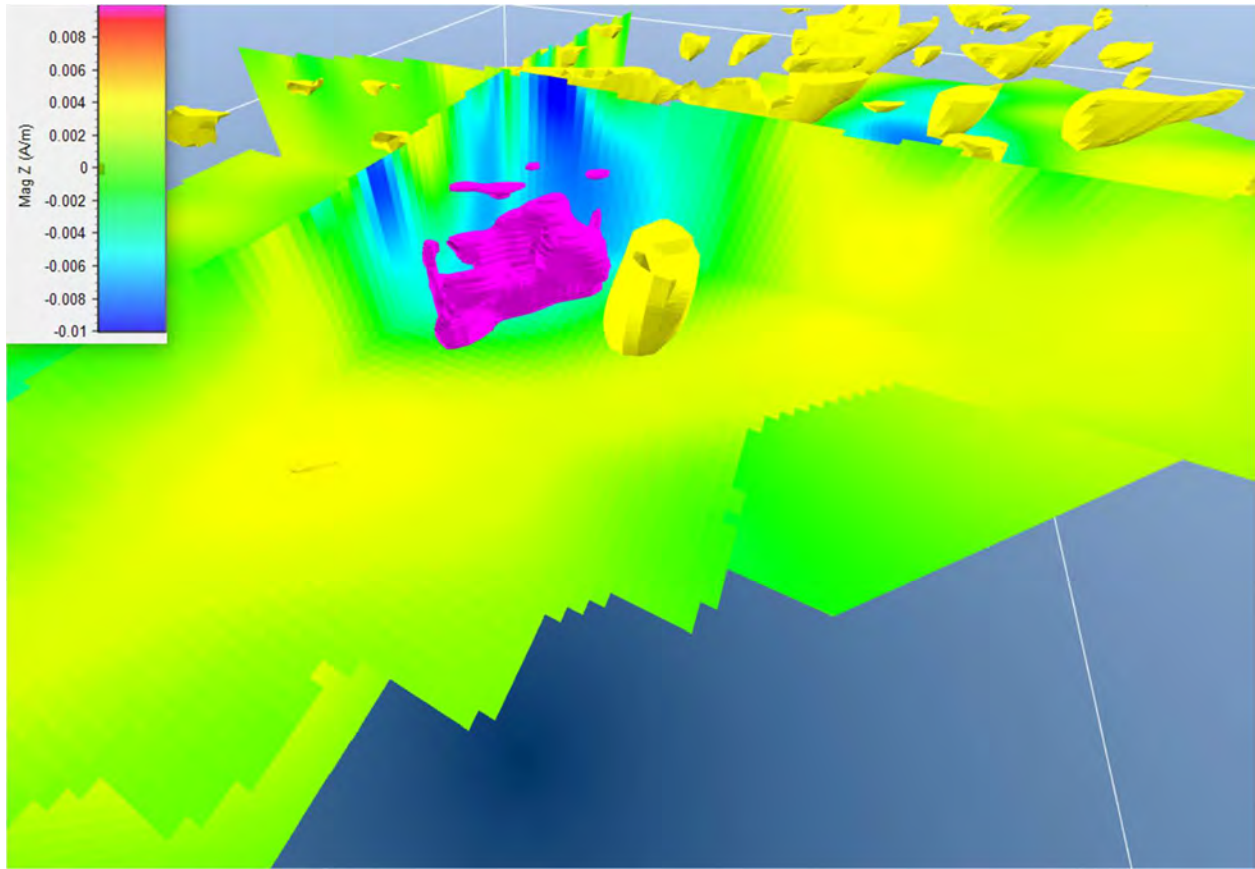


Figure 39. An isosurface view of the Z component of the magnetic vector looking southeast. The red body is the MPD body showing conductivities greater than 0.1 S/m. The yellow bodies are magnetic showing values greater than 0.004 A/m. The yellow body in the foreground is the postulated kimberlite.



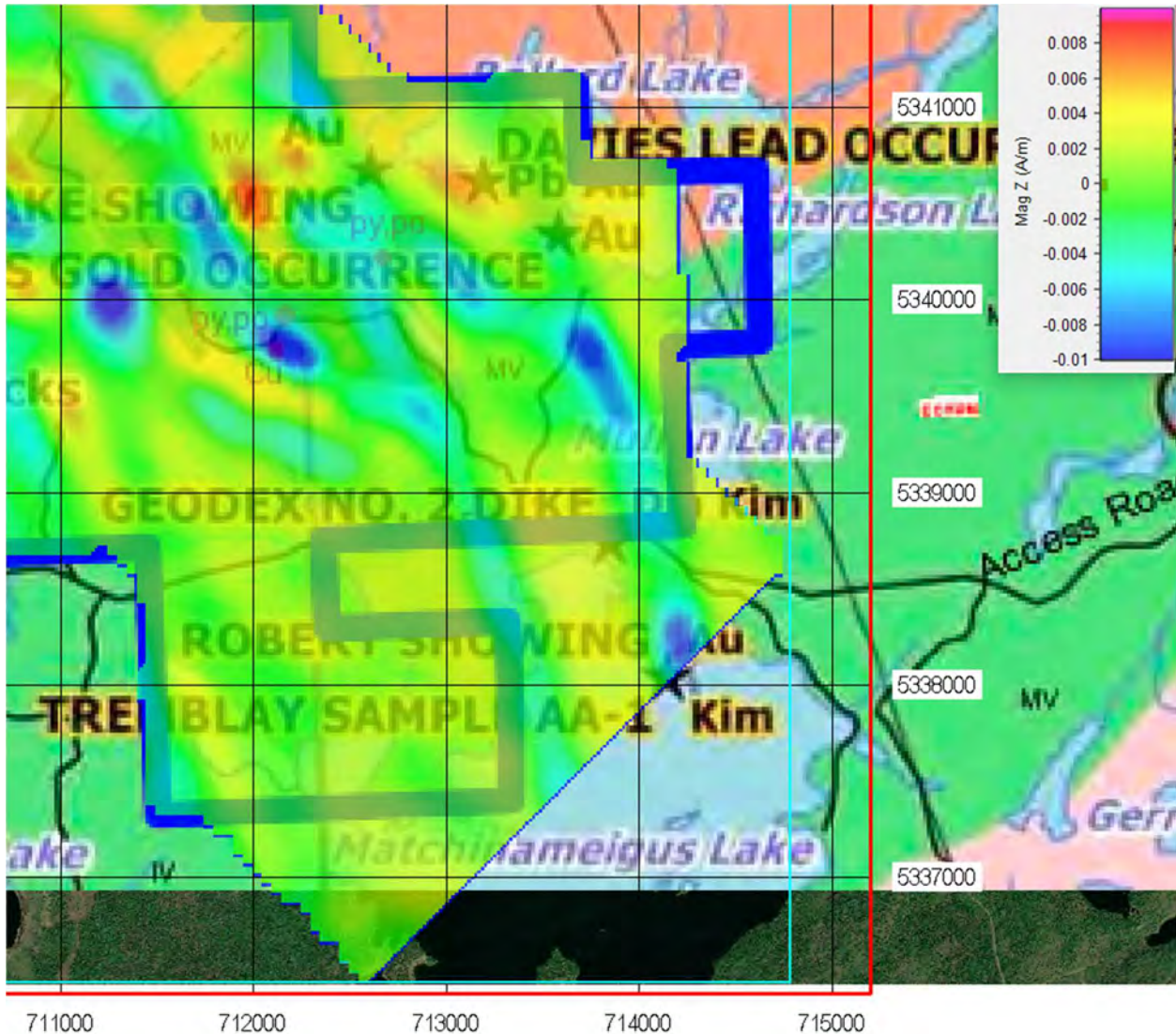


Figure 40: Closeup of the Z component of the magnetic vector on the southeast of the survey. Note the excellent correlation of the vertical component of magnetization with the copper and pyrite and pyrrhotite mineralization near 712000 mE and 5340000 mN.

## 7 Digital Deliverables

All models are delivered in msh/model format:

- 3D volume of resistivity derived from AEM data,
- 3D volume of chargeability derived from AEM data,
- 3D volume of magnetic susceptibility derived from TMI data,
- 3D volume of magnetization vector derived from TMI data,
- Final report in PDF format.

The coordinate system for all deliverables is UTM Zone 16 N with a NAD 83 datum. The units are meters for depth, elevation, and horizontal distance. The UBC msh/model file parameters and null values are specified in the readme file provided with the deliverables.



## 8 Recommendations for a Follow-up Study

TechnoImaging recommends the following additional work to assist Kingsview with their mineral exploration projects over the Echum Property.

- 1) Target generation based on follow-up interpretation of the data and inversion results which includes an enhanced study of prospective targets using constrained inversion over specific areas.
- 2) Conducting distributed ground Spectral IP surveys over selected areas and interpretation of their results by the GEMTIP model to provide additional critical information about the location of the targets and type of mineralization in the survey area.

## 9 Conclusions

This report provides a brief geological and geophysical setting for the work done on the Echum Project Area by TechnoImaging. In addition, it documents the data collection methods and gives an overview of the theoretical processing applied to the data to generate 3D models.

The field data collection was of high quality, and three-dimensional conductivity, chargeability, susceptibility, and magnetic vector property models have been produced from the provided field data. The results correlate well with the known geology in the area. Several examples of potential targets have been suggested based on our understanding of the area, and an abbreviated summary is listed below:

- Detailed 3D conductivity model of the VTEM data covering the MPD Zinc-Copper mineralization outlining a zone of the order of 600 m in length and 100m below surface. At least one other weaker and smaller, but very similar conductor was defined to the southeast.
- Although the airborne-based chargeability highlights lake bottom sediments in the project area, there are other chargeability anomalies in other areas that warrant further investigation for gold and disseminated sulphide mineralization.
- An isosurface view of the Z component of the magnetic vector defined the postulated kimberlite in 3D.
- There is an excellent correlation of the vertical component of the magnetization vector with copper, pyrite and pyrrhotite mineralization and similar responses in a favorable geological setting, which could be worth following up.

This report provides a high-level overview of what we see in the results, and it gives ideas on how to view and integrate the 3D models and suggestions on how to perform interpretation of the data. These models are rich with information, but a full interpretation of the geophysics requires a detailed geological understanding of the area and knowledge to build and test geological models.

TechnoImaging would be pleased to help direct these initial efforts in collaboration with staff geologists and geophysicists.

## 10 References

Alfouzan, F., Alotaibi, A., Cox, L., and Zhdanov, M. S., 2020, Spectral Induced Polarization Survey with Distributed Array System for Mineral Exploration: Case Study in Saudi Arabia: *Minerals*, 10, 769.

Combrinck, M., Cox, L.H., Wilson, G.A., Zhdanov M. S., 2012, 3D VTEM inversion for delineating sub-vertical shear zones in the West African gold belt, ASEG Extended Abstracts, 2012:1, 1-4.

Cox, L., Endo, M., & Zhdanov, M. (2015, June). 3D Inversion of AEM Data Based on a Hybrid IE-FE Method and the Moving Sensitivity Domain Approach with a Direct Solver. In 77th EAGE Conference and Exhibition 2015 (Vol. 2015, No. 1, pp. 1-5). European Association of Geoscientists & Engineers.

Cox, L. H., and Zhdanov, M. S., 2008, Advanced computational methods of rapid and rigorous 3-D inversion of airborne electromagnetic data: *Communications in Computational Physics*, 3 (1), 160-179.

Cox, L. H., Wilson, G. A., & Zhdanov, M. S. (2012), 3D inversion of airborne electromagnetic data. *Geophysics*, 77(4), WB59-WB69.

Čuma, M., and Zhdanov, M. S., 2014, Massively parallel regularized 3D inversion of potential fields on CPUs and GPUs: *Computers & Geosciences*, 62, 80-87.

Jorgensen, M., and Zhdanov, M. S., 2021, Recovering magnetization of rock formations by jointly inverting airborne gravity gradiometry and total magnetic intensity data: *Minerals*, 11 (4), 366.

Zhdanov, M.S., Cox, L., and Rudd, J., 2013, Paradigm change in 3D inversion of airborne EM surveys: case study for oil sands exploration near Fort McMurray, Alberta: *First Break*, 31 (4), 45-49.

Zhdanov, M. S., 2008, Generalized effective-medium theory of induced polarization: *Geophysics* 73, F197-F211

Zhdanov, M. S., 2015, *Inverse theory and applications in geophysics*. Elsevier.

Zhdanov, M.S., Zhu, Y., Endo, M., and Kinakin, Y., 2016, Novel approach to joint 3D inversion of EM and potential field data using Gramian constraints: *First Break*, 34, 59-64.

Zhdanov, M. S., 2018, *Foundations of geophysical electromagnetic theory and methods*. Elsevier.

Zhdanov M. S., F. A. Alfouzan, L. Cox, A. Alotaibi, M. Alyousif, D. Sunwall, and M. Endo, 2018, Large-Scale 3D Modeling and Inversion of Multiphysics Airborne Geophysical Data: A Case Study from the Arabian Shield, Saudi Arabia: *Minerals*, 8, 271.

Zhdanov M.S., Ellis R., and Mukherjee S., 2004, Three-dimensional regularized focusing inversion of gravity gradient tensor component data: *Geophysics*, 69 (4), 925-937

Zhu, Y., M.S. Zhdanov, and Čuma, M., 2015, Inversion of TMI data for the magnetization vector using Gramian constraints: 85th Annual International Meeting, SEG, Expanded Abstracts, 1602-1606.





# VTEM™ Plus

---

REPORT ON A HELICOPTER-BORNE VERSATILE  
TIME DOMAIN ELECTROMAGNETIC (VTEM™ Plus) AND  
HORIZONTAL MAGNETIC GRADIOMETER GEOPHYSICAL SURVEY

APRIL 2021

PROJECT:	ECHUM PROJECT
LOCATION:	WAWA, ON
FOR:	KINGSVIEW MINERALS LTD.
SURVEY FLOWN:	JANUARY - FEBRUARY 2021
PROJECT:	GL200223

Geotech Ltd.  
270 Industrial Parkway South  
Aurora, ON Canada L4G 3T9

Tel: +1 905 841 5004  
Web: [www.geotech.ca](http://www.geotech.ca)  
Email: [info@geotech.ca](mailto:info@geotech.ca)



# TABLE OF CONTENTS

<b>EXECUTIVE SUMMARY</b> .....	<b>3</b>
<b>1. INTRODUCTION</b> .....	<b>4</b>
1.1 General Considerations.....	4
1.2 Survey and System Specifications.....	5
1.3 Topographic Relief and Cultural Features.....	6
<b>2. DATA ACQUISITION</b> .....	<b>7</b>
2.1 Survey Area.....	7
2.2 Survey Operations.....	7
2.3 Flight Specifications.....	8
2.4 Aircraft and Equipment.....	8
2.4.1 Survey Aircraft.....	8
2.4.2 Electromagnetic System.....	8
2.4.3 Full Waveform VTEM™ Sensor Calibration.....	12
2.4.4 Horizontal Magnetic Gradiometer.....	12
2.4.5 Radar Altimeter.....	12
2.4.6 GPS Navigation System.....	12
2.4.7 Digital Acquisition System.....	12
2.5 Base Station.....	13
<b>3. PERSONNEL</b> .....	<b>14</b>
<b>4. DATA PROCESSING AND PRESENTATION</b> .....	<b>15</b>
4.1 Flight Path.....	15
4.2 Electromagnetic Data.....	15
4.3 Horizontal Magnetic Gradiometer Data.....	17
<b>5. DELIVERABLES</b> .....	<b>18</b>
5.1 Survey Report.....	18
5.2 Maps.....	18
5.3 Digital Data.....	19
<b>6. CONCLUSIONS AND RECOMMENDATIONS</b> .....	<b>23</b>

## LIST OF FIGURES

Figure 1: Survey location.....	4
Figure 2: Survey area location map on Google Earth.....	5
Figure 3: Echum Project flight paths over a Google Earth Image.....	6
Figure 4: VTEM™ Transmitter Current Waveform.....	8
Figure 5: VTEM™plus System Configuration.....	11
Figure 6: Z, X and Fraser filtered X (FFx) components for “thin” target.....	16

## LIST OF TABLES

Table 1: Survey Specifications.....	7
Table 2: Survey schedule.....	7
Table 3: Off-Time Decay Sampling Scheme.....	9
Table 4: VTEM™ System Specifications.....	11
Table 5: Acquisition Sampling Rates.....	13
Table 6: Geosoft GDB Data Format.....	19
Table 7: Geosoft Resistivity Depth Image GDB Data Format.....	21
Table 8: Geosoft database for the VTEM waveform.....	22

## APPENDICES

A.	Survey Location Maps.....	A1
B.	Survey Survey Area Coordinates .....	B1
C.	Geophysical Maps .....	C1
D.	Generalized Modelling Results of the VTEM System.....	D1
E.	TAU Analysis .....	E1
F.	TEM Resistivity Depth Imaging (RDI) .....	F1
G.	Resistivity Depth Images (RDI).....	F1



## EXECUTIVE SUMMARY

### ECHUM PROJECT WAWA, ON

Between January 31<sup>st</sup> and February 12<sup>th</sup>, 2021, Geotech Ltd. carried out a helicopter-borne geophysical survey over the Echum Project near Wawa, ON.

Principal geophysical sensors included a versatile time domain electromagnetic (VTEM™ Plus) system and a horizontal magnetic gradiometer with two caesium sensors. Ancillary equipment included a GPS navigation system and a radar altimeter. A total of 387 line-kilometres of geophysical data were acquired during the survey.

In-field data quality assurance and preliminary processing were carried out on a daily basis during the acquisition phase. Preliminary and final data processing, including generation of final digital data and map products were undertaken from the office of Geotech Ltd. in Aurora, Ontario.

The preliminary processed survey results are presented as the following maps:

- Electromagnetic stacked profiles of the B-field Z Component
- Electromagnetic stacked profiles of dB/dt Z Component
- B-Field Z Component Channel grid
- dB/dt Z Component Channel grid
- Fraser Filtered X Component Channel grid
- Total Magnetic Intensity (TMI)
- Magnetic Total Horizontal Gradient
- Magnetic Tilt Angle Derivative
- Calculated Time Constant (Tau) with Calculated Vertical Derivative of TMI contours
- Resistivity Depth Images (RDI) sections, depth-slices, and voxel are presented.

Digital data include electromagnetic and magnetic products, plus ancillary data including the waveform.

The survey report describes the procedures for data acquisition, equipment used, processing, final image presentation and the specifications for the digital data set.

# 1. INTRODUCTION

## 1.1 GENERAL CONSIDERATIONS

Geotech Ltd. performed a helicopter-borne geophysical survey over the Echum Project near Wawa, ON (Figure 1 & Figure 2).

Gary Handley represented Kingsview Minerals Ltd. during the data acquisition and data processing phases of this project.

The geophysical surveys consisted of helicopter borne EM using the versatile time-domain electromagnetic (VTEM™) plus system with Full-Waveform processing. Measurements consisted of Vertical (Z) and In-line Horizontal (X & Y) components of the EM fields using an induction coil and a horizontal magnetic gradiometer using two caesium magnetometers. A total of 387 line-km of geophysical data were acquired during the survey.

The crew was based out of Wawa, ON (Figure 2) for the acquisition phase of the survey. Survey flying started on February 1<sup>st</sup> and was completed on February 10<sup>th</sup>, 2021.

Data quality control and quality assurance, and preliminary data processing were carried out on a daily basis during the acquisition phase of the project. Final data processing followed immediately after the end of the survey. Final reporting, data presentation and archiving were completed in April 2021.



Figure 1: Survey location

## 1.2 SURVEY AND SYSTEM SPECIFICATIONS

The survey area is located approximately 46 km northeast of Wawa, ON (Figure 2).

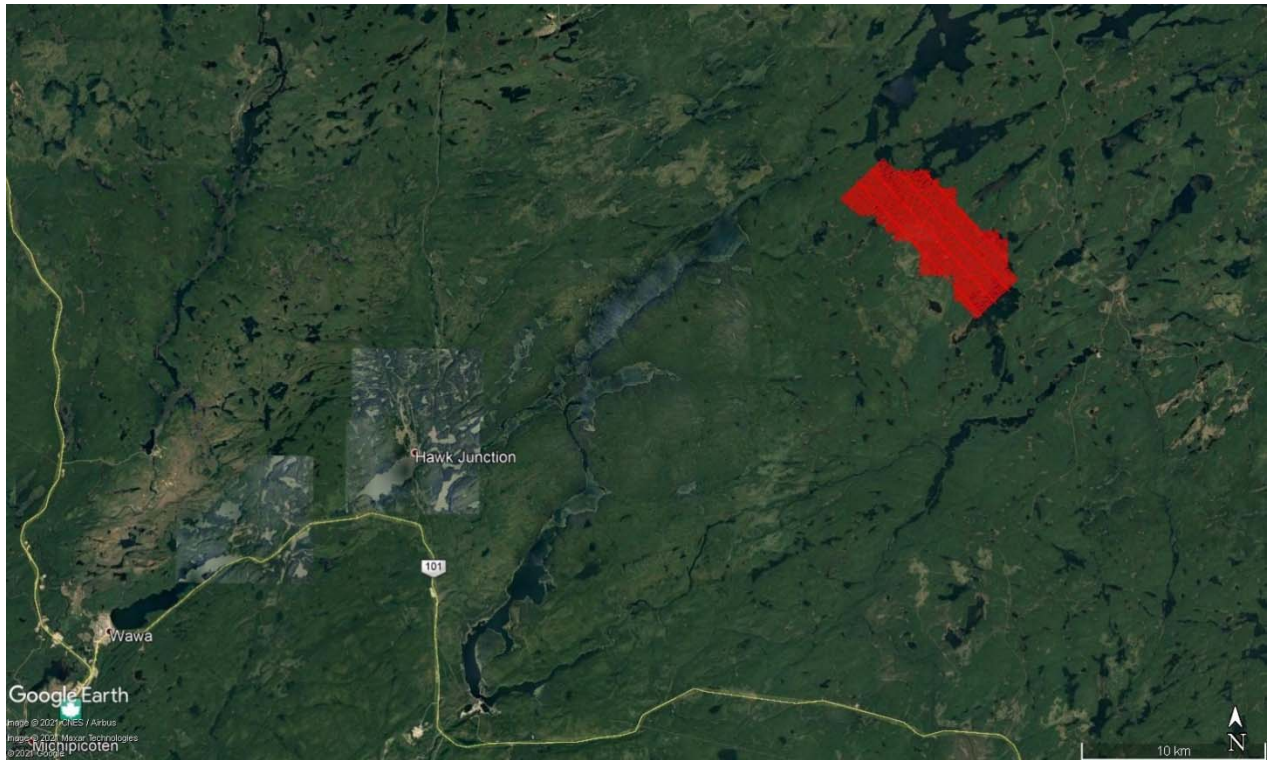


Figure 2: Survey area location map on Google Earth.

The Echum Project survey area was flown in a southwest to northeast ( $N 45^{\circ} E$  azimuth) direction with traverse line spacings of 100 metres, as depicted in Figure 3. Tie lines were flown perpendicular to traverse lines at 1000 metre line spacings. For more detailed information on the flight spacings and directions, see Table 1.



### 1.3 TOPOGRAPHIC RELIEF AND CULTURAL FEATURES

Topographically, the survey area exhibits relief with elevations ranging from 330 to 461 metres over an area of 34 square kilometres (Figure 3).

There are several lakes, rivers, and streams within the Echum Project area, along with visible signs of culture such as roads.

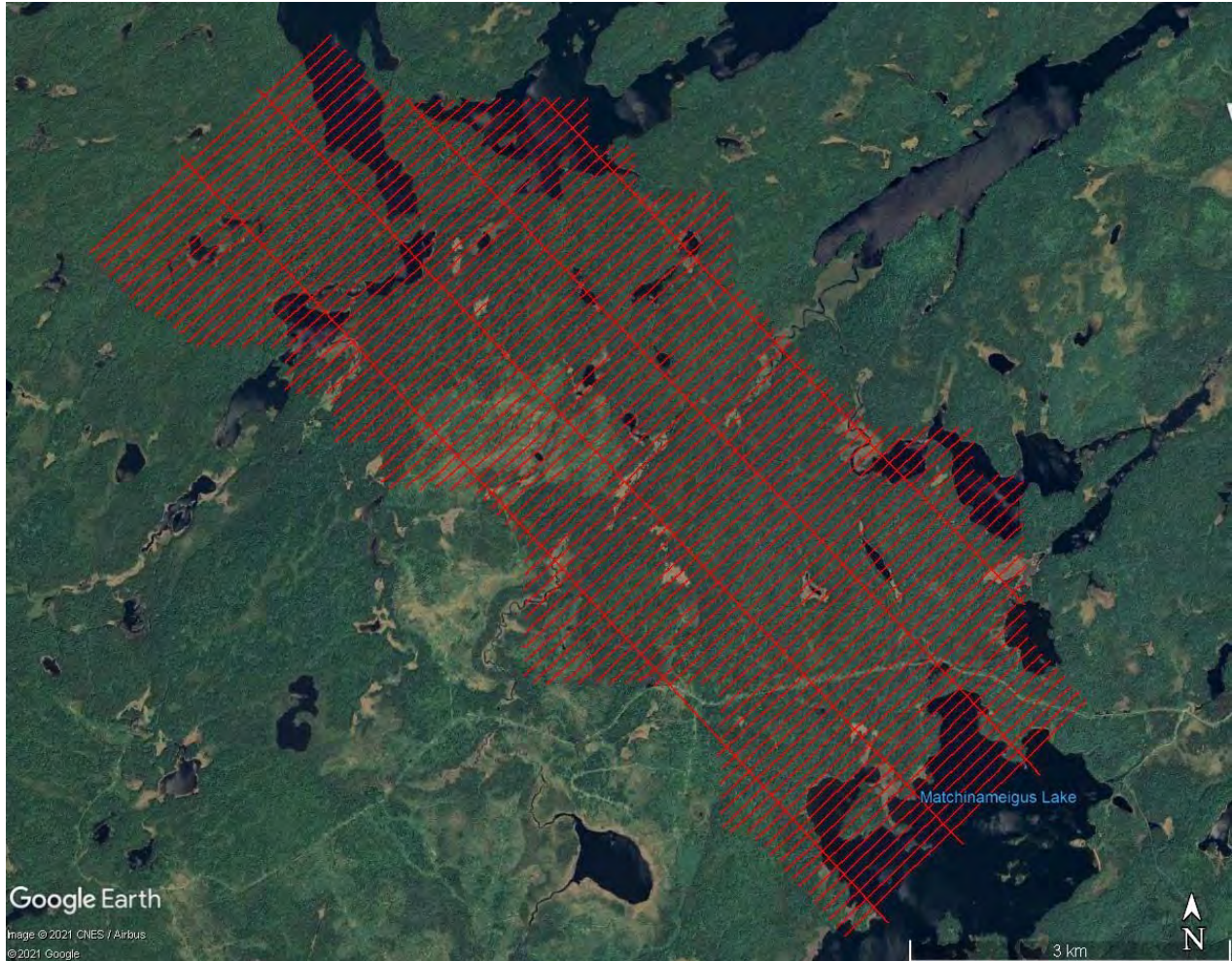


Figure 3: Echum Project flight paths over a Google Earth Image.

## 2. DATA ACQUISITION

### 2.1 SURVEY AREA

The survey area (see Figure 3 and Appendix A) and general flight specifications are as follows:

**Table 1:** Survey Specifications

Survey block	Line spacing (m)	Area (km <sup>2</sup> )	Planned <sup>1</sup> Line-km	Actual Line-km	Flight direction	Line numbers
Echum Project	Traverse: 100	34	366	387	N045°E / N225°E	L1000 – L1970
	Tie: 1000				N135°E / N315°E	T2000 – T2030
Total		34	366	387		

Survey area boundaries co-ordinates are provided in Appendix B.

### 2.2 SURVEY OPERATIONS

Survey operations were based out of Wawa, ON from January 31<sup>st</sup> to February 12<sup>th</sup>, 2021. The following table shows the timing of the flying.

**Table 2:** Survey schedule

Date	Comments
31-Jan	Mobilization to Wawa, local logistics
01-Feb	Production Flight - 96 km flown
02-Feb	Production Flight - 15 km flown
03-Feb	Production Flight - 125 km flown
04-Feb	Weather day
05-Feb	Weather day
06-Feb	Weather day
07-Feb	Production Flight - 44 km flown
08-Feb	Weather day
09-Feb	Weather day
10-Feb	Production Flight - 90 km flown
11-Feb	Commence Demobilization
12-Feb	Demobilization

<sup>1</sup> Note: Actual Line kilometres represent the total line kilometres in the final database. These line-km normally exceed the Planned Line-km, as indicated in the survey NAV files.

## 2.3 FLIGHT SPECIFICATIONS

During the survey, the helicopter was maintained at a mean altitude of 108 metres above the ground with an average survey speed of 78 km/hour. This allowed for an actual average Transmitter-receiver loop terrain clearance of 64 metres and a magnetic sensor clearance of 74 metres.

The on-board operator was responsible for monitoring the system integrity. He also maintained a detailed flight log during the survey, tracking the times of the flight as well as any unusual geophysical or topographic features.

On return of the aircrew to the base camp the survey data was transferred from a compact flash card (PCMCIA) to the data processing computer. The data were then uploaded via ftp to the Geotech office in Aurora for daily quality assurance and quality control by qualified personnel.

## 2.4 AIRCRAFT AND EQUIPMENT

### 2.4.1 SURVEY AIRCRAFT

The survey was flown using a Eurocopter Aerospatiale (A-Star) 350 B3 helicopter, registration C-GVMU. The helicopter is owned and operated by Geotech Aviation Ltd. Installation of the geophysical and ancillary equipment was carried out by a Geotech Ltd. crew.

### 2.4.2 ELECTROMAGNETIC SYSTEM

The electromagnetic system was a Geotech Time Domain EM (VTEM™ Plus) full receiver-waveform streamed data recorded system. The “full waveform VTEM system” uses the streamed half-cycle recording of transmitter and receiver waveforms to obtain a complete system response calibration throughout the entire survey flight. VTEM with the serial number 18 had been used for the survey. The VTEM™ transmitter current waveform is shown diagrammatically in Figure 4.

The VTEM™ Receiver and transmitter coils were in concentric-coplanar and Z-direction oriented configuration. The receiver system for the project also included coincident-coaxial X & Y-direction coils to measure the in-line dB/dt and calculate B-Field responses. The Transmitter-receiver loop was towed at a mean distance of 44 metres below the aircraft as shown in Figure 5.

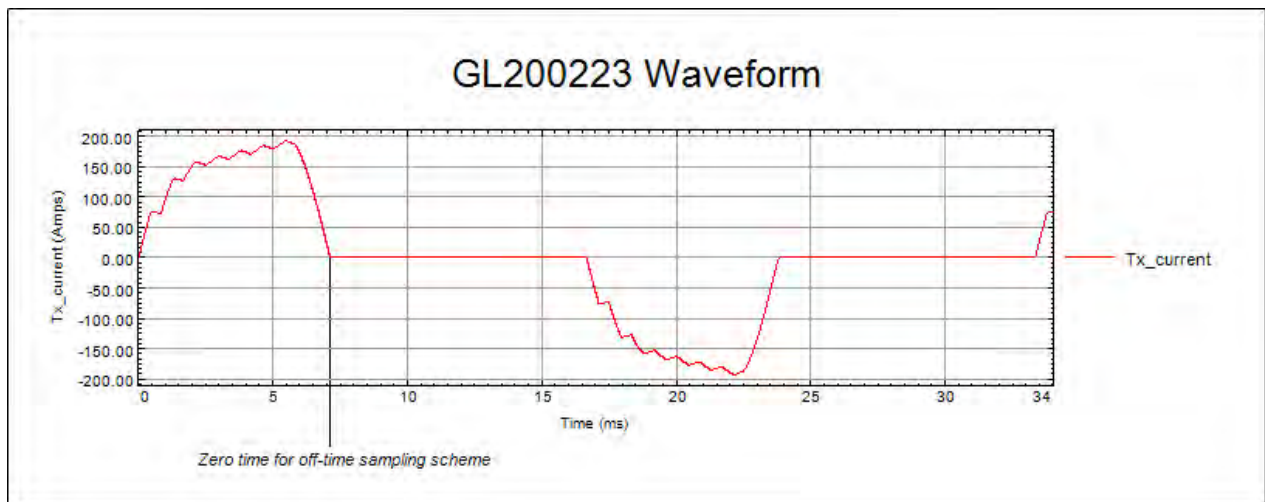


Figure 4: VTEM™ Transmitter Current Waveform



The VTEM™ decay sampling scheme is shown in Table 3 below. Forty-three time measurement gates were used for the final data processing in the range from 0.021 to 8.083 msec. Zero time for the off-time sampling scheme is equal to the current pulse width and is defined as the time near the end of the turn-off ramp where the dI/dt waveform falls to 1/2 of its peak value.

**Table 3:** Off-Time Decay Sampling Scheme

VTEM™ Decay Sampling Scheme				
Index	Start	End	Middle	Width
Milliseconds				
4	0.018	0.023	0.021	0.005
5	0.023	0.029	0.026	0.005
6	0.029	0.034	0.031	0.005
7	0.034	0.039	0.036	0.005
8	0.039	0.045	0.042	0.006
9	0.045	0.051	0.048	0.007
10	0.051	0.059	0.055	0.008
11	0.059	0.068	0.063	0.009
12	0.068	0.078	0.073	0.010
13	0.078	0.090	0.083	0.012
14	0.090	0.103	0.096	0.013
15	0.103	0.118	0.110	0.015
16	0.118	0.136	0.126	0.018
17	0.136	0.156	0.145	0.020
18	0.156	0.179	0.167	0.023
19	0.179	0.206	0.192	0.027
20	0.206	0.236	0.220	0.030
21	0.236	0.271	0.253	0.035
22	0.271	0.312	0.290	0.040
23	0.312	0.358	0.333	0.046
24	0.358	0.411	0.383	0.053
25	0.411	0.472	0.440	0.061
26	0.472	0.543	0.505	0.070
27	0.543	0.623	0.580	0.081
28	0.623	0.716	0.667	0.093
29	0.716	0.823	0.766	0.107
30	0.823	0.945	0.880	0.122
31	0.945	1.086	1.010	0.141
32	1.086	1.247	1.161	0.161
33	1.247	1.432	1.333	0.185
34	1.432	1.646	1.531	0.214
35	1.646	1.891	1.760	0.245
36	1.891	2.172	2.021	0.281
37	2.172	2.495	2.323	0.323
38	2.495	2.865	2.667	0.370

VTEM™ Decay Sampling Scheme				
Index	Start	End	Middle	Width
Milliseconds				
39	2.865	3.292	3.063	0.427
40	3.292	3.781	3.521	0.490
41	3.781	4.341	4.042	0.560
42	4.341	4.987	4.641	0.646
43	4.987	5.729	5.333	0.742
44	5.729	6.581	6.125	0.852
45	6.581	7.560	7.036	0.979
46	7.560	8.685	8.083	1.125

Z Component: 4 - 46 time gates  
X Component: 20 - 46 time gates  
Y Component: 20 - 46 time gates

**Table 4:** VTEM™ System Specifications

Transmitter	Receiver
<ul style="list-style-type: none"> <li>• Transmitter loop diameter: 26 m</li> <li>• Number of turns: 4</li> <li>• Effective Transmitter loop area: 2123.7 m<sup>2</sup></li> <li>• Transmitter base frequency: 30 Hz</li> <li>• Peak current: 193.0 A</li> <li>• Pulse width: 7.12 ms</li> <li>• Waveform shape: Bi-polar trapezoid</li> <li>• Peak dipole moment: 409,877 nIA</li> <li>• Average transmitter-receiver loop terrain clearance: 64 metres</li> </ul>	<ul style="list-style-type: none"> <li>• X-Coil diameter: 0.32 m</li> <li>• Number of turns: 245</li> <li>• Effective coil area: 19.69 m<sup>2</sup></li> <li>• Y-Coil diameter: 0.32 m</li> <li>• Number of turns: 245</li> <li>• Effective coil area: 19.69 m<sup>2</sup></li> <li>• Z-Coil diameter: 1.2 m</li> <li>• Number of turns: 100</li> <li>• Effective coil area: 113.04 m<sup>2</sup></li> </ul>

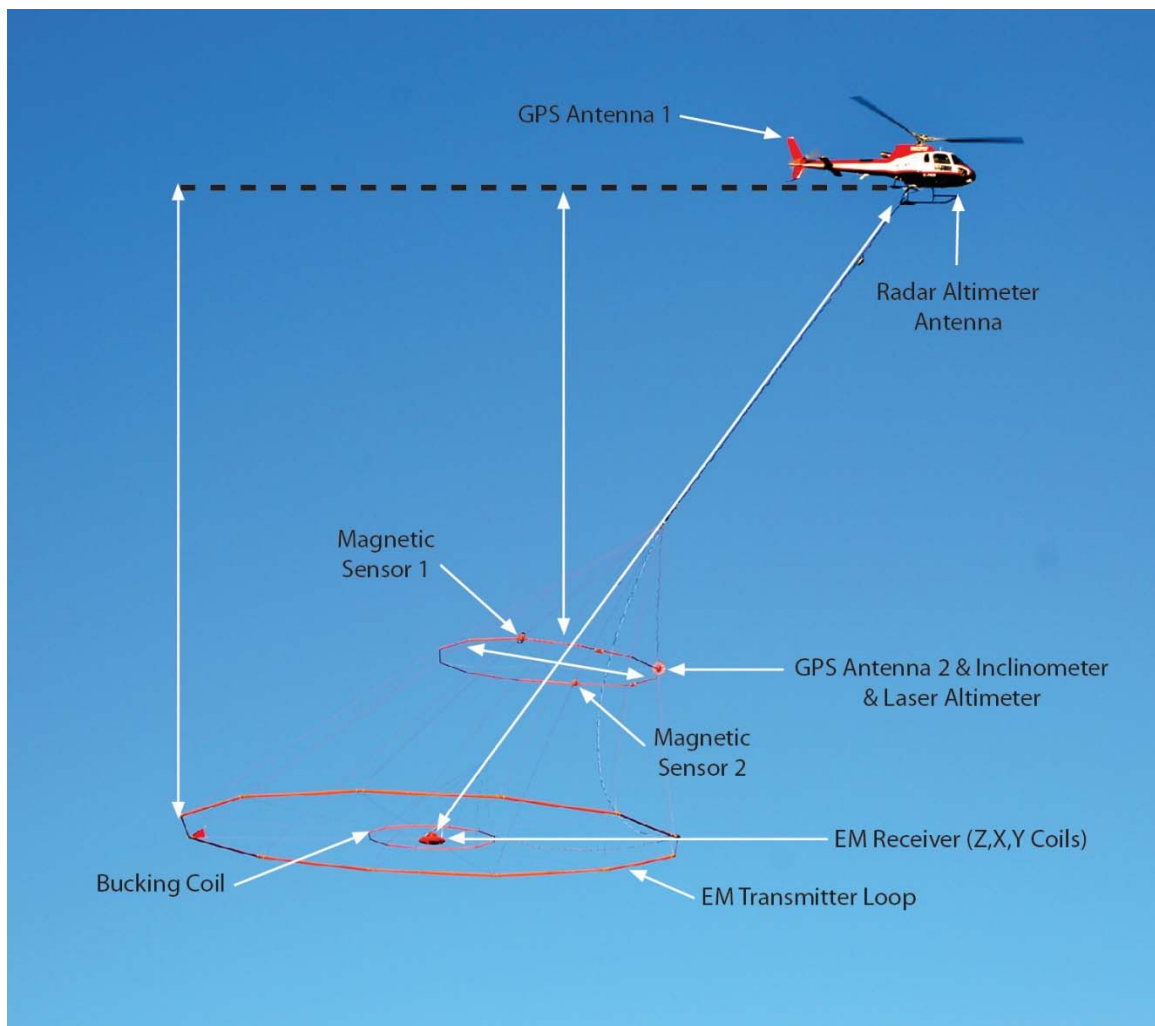


**Figure 5:** VTEM™plus System Configuration.



### 2.4.3 FULL WAVEFORM VTEM™ SENSOR CALIBRATION

The calibration is performed on the complete VTEM™ system installed in and connected to the helicopter, using special calibration equipment. This calibration takes place on the ground at the start of the project prior to surveying.

The procedure takes half-cycle files acquired and calculates a calibration file consisting of a single stacked half-cycle waveform. The purpose of the stacking is to attenuate natural and man-made magnetic signals, leaving only the response to the calibration signal.

This calibration allows the transfer function between the EM receiver and data acquisition system and the transfer function between the current monitor and data acquisition system to be determined. These calibration results are then used in VTEM full waveform processing.

### 2.4.4 HORIZONTAL MAGNETIC GRADIOMETER

The horizontal magnetic gradiometer consists of two Geometrics split-beam field magnetic sensors with a sampling interval of 0.1 seconds. These sensors are mounted 12.5 metres apart on a separate loop, 10 metres above the Transmitter-receiver loop. A GPS antenna and Gyro Inclinator is installed on the separate loop to accurately record the tilt and position of the magnetic gradiometer.

### 2.4.5 RADAR ALTIMETER

A Terra TRA 3000/TRI 40 radar altimeter was used to record terrain clearance. The antenna was mounted beneath the bubble of the helicopter cockpit (Figure 5).

### 2.4.6 GPS NAVIGATION SYSTEM

The navigation system used was a Geotech PC104 based navigation system utilizing a NovAtel's WAAS (Wide Area Augmentation System) enabled GPS receiver, Geotech navigate software, a full screen display with controls in front of the pilot to direct the flight and a NovAtel GPS antenna mounted on the helicopter tail (Figure 5). As many as 11 GPS and two WAAS satellites may be monitored at any one time. The positional accuracy or circular error probability (CEP) is 1.8 m, with WAAS active, it is 1.0 m. The coordinates of the survey area were set-up prior to the survey and the information was fed into the airborne navigation system. The second GPS antenna is installed on the additional magnetic loop together with Gyro Inclinator.

### 2.4.7 DIGITAL ACQUISITION SYSTEM

A Geotech data acquisition system recorded the digital survey data on an internal compact flash card. Data is displayed on an LCD screen as traces to allow the operator to monitor the integrity of the system. The data type and sampling interval as provided in Table 5

**Table 5:** Acquisition Sampling Rates

Data Type	Sampling
TDEM	0.1 sec
Magnetometer	0.1 sec
GPS Position	0.2 sec
Radar Altimeter	0.2 sec
Inclinometer	0.1 sec

## 2.5 BASE STATION

A combined magnetometer/GPS base station was utilized on this project. A Geometrics Caesium vapour magnetometer was used as a magnetic sensor with a sensitivity of 0.001 nT. The base station was recording the magnetic field together with the GPS time at 1 Hz on a base station computer.

The base station magnetometer sensor was installed in a secured location away from electric transmission lines and moving ferrous objects such as motor vehicles. The base station data were backed-up to the data processing computer at the end of each survey day.

### 3. PERSONNEL

The following Geotech Ltd. personnel were involved in the project.

#### FIELD:

Project Manager:	Adrian Sarmasag (Office)
Data QC:	Marta Orta
Crew chief:	Daniel Zatingh
Operator:	n/a

The survey pilot and the mechanical engineer were employed directly by the helicopter operator – Geotech Aviation Ltd.

Pilot:	Rob Girald
Mechanical Engineer:	n/a

#### OFFICE:

Preliminary Data Processing:	Marta Orta
Final Data Processing:	Zihao Han
Data QA/QC:	Emily Data Jean Legault
Reporting/Mapping:	Emily Data Moyosore Lanisa

Processing and Interpretation phases were carried out by Zihao Han under the supervision of Emily Data & Jean M. Legault, M.Sc.A, P.Eng, P.Geo – Chief Geophysicist. The customer relations were looked after by Paolo Berardelli.



## 4. DATA PROCESSING AND PRESENTATION

Data compilation and processing were carried out by the application of Geosoft OASIS Montaj and programs proprietary to Geotech Ltd.

### 4.1 FLIGHT PATH

The flight path, recorded by the acquisition program as WGS 84 latitude/longitude, was converted into the NAD83 Datum, UTM Zone 16N coordinate system in Oasis Montaj.

The flight path was drawn using linear interpolation between x, y positions from the navigation system. Positions are updated every second and expressed as UTM easting's (x) and UTM northing's (y).

### 4.2 ELECTROMAGNETIC DATA

The Full Waveform EM specific data processing operations included:

- Half cycle stacking (performed at time of acquisition).
- System response correction.
- Parasitic and drift removal.

A three-stage digital filtering process was used to reject major spheric events and to reduce noise levels. Local spheric activity can produce sharp, large amplitude events that cannot be removed by conventional filtering procedures. Smoothing or stacking will reduce their amplitude but leave a broader residual response that can be confused with geological phenomena. To avoid this possibility, a computer algorithm searches out and rejects the major spheric events.

The signal to noise ratio was further improved by the application of a low pass linear digital filter. This filter has zero phase shift which prevents any lag or peak displacement from occurring, and it suppresses only variations with a wavelength less than about 1 second or 15 metres. This filter is a symmetrical 1 sec linear filter.

The results are presented as stacked profiles of EM voltages for the time gates, in linear - logarithmic scale for the B-field Z component and dB/dt responses in the Z and X components. B-field Z component time channels recorded at 0.880 milliseconds after the termination of the impulse is also presented as a colour image. Calculated Time Constant (TAU) with Calculated Vertical Derivative contours is presented in Appendix C and E. Resistivity Depth Image (RDI) is also presented in Appendix G.

VTEM™ has three receiver coil orientations. Z-axis coil is oriented parallel to the transmitter coil axis and both are horizontal to the ground. The X-axis coil is oriented parallel to the ground and along the line-of-flight. The Y-axis coil is oriented parallel to the ground and perpendicular to the line-of-flight. The combination of the X, Y and Z coils configuration provides information on the position, depth, dip, and thickness of a conductor. Generalized modeling results of VTEM data, are shown in Appendix D.

In general X-component data produce cross-over type anomalies: from “+ to -” in flight direction of flight for “thin” sub vertical targets and from “- to +” in direction of flight for “thick” targets. Z component data produce double peak type anomalies for “thin” sub vertical targets and single peak for “thick” targets.

The limits and change-over of “thin-thick” depends on dimensions of a TEM system (Appendix D, Figure D-16).

Because of X component polarity is under line-of-flight, convolution Fraser Filter (Figure 6) is applied to X component data to represent axes of conductors in the form of grid map. In this case positive FF anomalies always correspond to “plus-to-minus” X data crossovers independent of the flight direction.

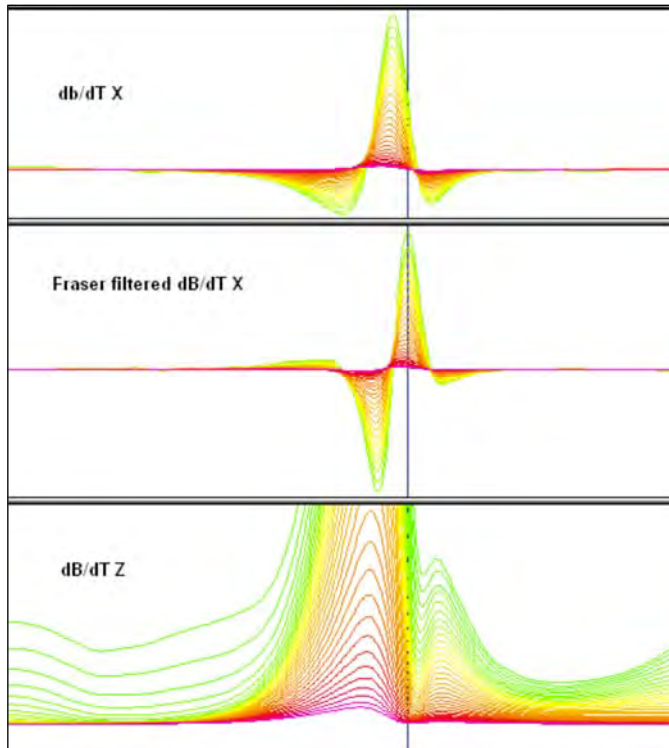


Figure 6: Z, X and Fraser filtered X (FFx) components for “thin” target.

### 4.3 HORIZONTAL MAGNETIC GRADIOMETER DATA

The horizontal gradients data from the VTEM™Plus are measured by two magnetometers 12.5 m apart on an independent bird mounted 10m above the VTEM™ loop. A GPS and a Gyro Inclinometer help to determine the positions and orientations of the magnetometers. The data from the two magnetometers are corrected for position and orientation variations, as well as for the diurnal variations using the base station data.

The position of the centre of the horizontal magnetic gradiometer bird is calculated from the GPS utilizing in-house processing tool in Geosoft. Following that total magnetic intensity is calculated at the center of the bird by calculating the mean values from both sensors. In addition to the total intensity advanced processing is done to calculate the in-line and cross-line (or lateral) horizontal gradient which enhance the understanding of magnetic targets. The in-line (longitudinal) horizontal gradient is calculated from the difference of two consecutive total magnetic field readings divided by the distance along the flight line direction, while the cross-line (lateral) horizontal magnetic gradient is calculated from the difference in the magnetic readings from both magnetic sensors divided by their horizontal separation.

Two advanced magnetic derivative products, the total horizontal derivative (THDR), and tilt angle derivative and are also created. The total horizontal derivative or gradient is defined as:

$THDR = \sqrt{H_x^2 + H_y^2}$ , where  $H_x$  and  $H_y$  are cross-line and in-line horizontal gradients.

The tilt angle derivative (TDR) is defined as:

$TDR = \arctan(V_z/THDR)$ , where THDR is the total horizontal derivative, and  $V_z$  is the vertical derivative.

Measured cross-line gradients can help to enhance cross-line linear features during gridding.

## 5. DELIVERABLES

### 5.1 SURVEY REPORT

The survey report describes the data acquisition, processing, and final presentation of the survey results. The survey report is provided in two paper copies and digitally in PDF format.

### 5.2 MAPS

Final maps were produced at scale of 1:15,000 for best representation of the survey size and line spacing. The coordinate/projection system used was NAD83 Datum, UTM Zone 16N. All maps show the flight path trace and topographic data; latitude and longitude are also noted on maps.

The results of the survey are presented as EM profiles, a late-time gate gridded EM channel, and a colour magnetic TMI contour map.

- Maps at 1:15,000 in Geosoft MAP format, as follows:

GL200223_15k_dBdt:	dB/dt profiles Z Component, Time Gates 0.220 – 7.036 ms in linear – logarithmic scale.
GL200223_15k_BField:	B-field profiles Z Component, Time Gates 0.220 – 7.036 ms in linear – logarithmic scale.
GL200223_15k_BFz30:	B-field Z Component Channel 30, Time Gate 0.880 ms colour image.
GL200223_15k_SFz25:	VTEM dB/dt Z Component Channel 25, Time Gate 0.440 ms colour image
GL200223_15k_SFxFF22:	Fraser Filtered dB/dt X Component Channel 22, Time Gate 0.290 ms colour image.
GL200223_15k_TMI:	Total Magnetic Intensity (TMI) colour image and contours.
GL200223_15k_TauSF_CVG:	dB/dt Calculated Time Constant (Tau) with Calculated Vertical Derivative contours
GL200223_15k_TotHG:	Magnetic Total Horizontal Gradient colour image.
GL200223_15k_TiltDrv:	Magnetic Tilt-Angle Derivative colour image

- Maps are also presented in PDF format.
- The topographic data base was derived from 1:50,000 CANVEC data. Background shading is derived from ASTER GDEM (<https://gdex.cr.usgs.gov/gdex/>). Inset data is from Geocommunities ([www.geocomm.com](http://www.geocomm.com))
- A Google Earth file *GL200223\_Kingsview.kmz* showing the flight path of the block is included. Free versions of Google Earth software from: <http://earth.google.com/download-earth.html>



### 5.3 DIGITAL DATA

Two copies of the data and maps on DVD were prepared to accompany the report. Each DVD contains a digital file of the line data in GDB Geosoft Montaj format as well as the maps in Geosoft Montaj Map and PDF format.

- DVD structure.

Data                    contains databases, grids and maps, as described below.  
 Report                 contains a copy of the report and appendices in PDF format.

Databases in Geosoft GDB format, containing the channels listed in Table 6.

**Table 6:** Geosoft GDB Data Format

Channel name	Units	Description
X	metres	Easting NAD83 Zone 16N
Y	metres	Northing NAD83 Zone 16N
Longitude	Decimal Degrees	WGS84 Longitude data
Latitude	Decimal Degrees	WGS84 Latitude data
Z	metres	GPS antenna elevation
Zb	metres	EM bird elevation
Radar	metres	Helicopter terrain clearance from radar altimeter
Radarb	metres	Calculated EM transmitter-receiver loop terrain clearance from radar altimeter
DEM	metres	Digital Elevation Model
Gtime	Seconds of the day	GPS time
Mag1L	nT	Measured Total Magnetic field data (left sensor)
Mag1R	nT	Measured Total Magnetic field data (right sensor)
Basemag	nT	Magnetic diurnal variation data
Mag2LZ	nT	Z corrected (w.r.t. loop center) and diurnal corrected magnetic field - left mag
Mag2RZ	nT	Z corrected (w.r.t. loop center) and diurnal corrected magnetic field - right mag
TMI2	nT	Calculated from diurnal corrected total magnetic field intensity of the centre of the loop
TMI3	nT	Microleveled total magnetic field intensity of the centre of the loop
Hginline		Calculated in-line gradient
Hgcxline		Measured cross-line gradients
CVG	nT/m	Calculated Magnetic Vertical Gradient of TMI
SFz[4]	pV/(A*m <sup>4</sup> )	Z dB/dt 0.021 millisecond time channel
SFz[5]	pV/(A*m <sup>4</sup> )	Z dB/dt 0.026 millisecond time channel
SFz[6]	pV/(A*m <sup>4</sup> )	Z dB/dt 0.031 millisecond time channel
SFz[7]	pV/(A*m <sup>4</sup> )	Z dB/dt 0.036 millisecond time channel
SFz[8]	pV/(A*m <sup>4</sup> )	Z dB/dt 0.042 millisecond time channel
SFz[9]	pV/(A*m <sup>4</sup> )	Z dB/dt 0.048 millisecond time channel
SFz[10]	pV/(A*m <sup>4</sup> )	Z dB/dt 0.055 millisecond time channel
SFz[11]	pV/(A*m <sup>4</sup> )	Z dB/dt 0.063 millisecond time channel
SFz[12]	pV/(A*m <sup>4</sup> )	Z dB/dt 0.073 millisecond time channel
SFz[13]	pV/(A*m <sup>4</sup> )	Z dB/dt 0.083 millisecond time channel
SFz[14]	pV/(A*m <sup>4</sup> )	Z dB/dt 0.096 millisecond time channel

Channel name	Units	Description
SFz[15]	pV/(A*m <sup>4</sup> )	Z dB/dt 0.110 millisecond time channel
SFz[16]	pV/(A*m <sup>4</sup> )	Z dB/dt 0.126 millisecond time channel
SFz[17]	pV/(A*m <sup>4</sup> )	Z dB/dt 0.145 millisecond time channel
SFz[18]	pV/(A*m <sup>4</sup> )	Z dB/dt 0.167 millisecond time channel
SFz[19]	pV/(A*m <sup>4</sup> )	Z dB/dt 0.192 millisecond time channel
SFz[20]	pV/(A*m <sup>4</sup> )	Z dB/dt 0.220 millisecond time channel
SFz[21]	pV/(A*m <sup>4</sup> )	Z dB/dt 0.253 millisecond time channel
SFz[22]	pV/(A*m <sup>4</sup> )	Z dB/dt 0.290 millisecond time channel
SFz[23]	pV/(A*m <sup>4</sup> )	Z dB/dt 0.333 millisecond time channel
SFz[24]	pV/(A*m <sup>4</sup> )	Z dB/dt 0.383 millisecond time channel
SFz[25]	pV/(A*m <sup>4</sup> )	Z dB/dt 0.440 millisecond time channel
SFz[26]	pV/(A*m <sup>4</sup> )	Z dB/dt 0.505 millisecond time channel
SFz[27]	pV/(A*m <sup>4</sup> )	Z dB/dt 0.580 millisecond time channel
SFz[28]	pV/(A*m <sup>4</sup> )	Z dB/dt 0.667 millisecond time channel
SFz[29]	pV/(A*m <sup>4</sup> )	Z dB/dt 0.766 millisecond time channel
SFz[30]	pV/(A*m <sup>4</sup> )	Z dB/dt 0.880 millisecond time channel
SFz[31]	pV/(A*m <sup>4</sup> )	Z dB/dt 1.010 millisecond time channel
SFz[32]	pV/(A*m <sup>4</sup> )	Z dB/dt 1.161 millisecond time channel
SFz[33]	pV/(A*m <sup>4</sup> )	Z dB/dt 1.333 millisecond time channel
SFz[34]	pV/(A*m <sup>4</sup> )	Z dB/dt 1.531 millisecond time channel
SFz[35]	pV/(A*m <sup>4</sup> )	Z dB/dt 1.760 millisecond time channel
SFz[36]	pV/(A*m <sup>4</sup> )	Z dB/dt 2.021 millisecond time channel
SFz[37]	pV/(A*m <sup>4</sup> )	Z dB/dt 2.323 millisecond time channel
SFz[38]	pV/(A*m <sup>4</sup> )	Z dB/dt 2.667 millisecond time channel
SFz[39]	pV/(A*m <sup>4</sup> )	Z dB/dt 3.063 millisecond time channel
SFz[40]	pV/(A*m <sup>4</sup> )	Z dB/dt 3.521 millisecond time channel
SFz[41]	pV/(A*m <sup>4</sup> )	Z dB/dt 4.042 millisecond time channel
SFz[42]	pV/(A*m <sup>4</sup> )	Z dB/dt 4.641 millisecond time channel
SFz[43]	pV/(A*m <sup>4</sup> )	Z dB/dt 5.333 millisecond time channel
SFz[44]	pV/(A*m <sup>4</sup> )	Z dB/dt 6.125 millisecond time channel
SFz[45]	pV/(A*m <sup>4</sup> )	Z dB/dt 7.036 millisecond time channel
SFz[46]	pV/(A*m <sup>4</sup> )	Z dB/dt 8.083 millisecond time channel
SFx[20]	pV/(A*m <sup>4</sup> )	X dB/dt 0.220 millisecond time channel
SFx[21]	pV/(A*m <sup>4</sup> )	X dB/dt 0.253 millisecond time channel
SFx[22]	pV/(A*m <sup>4</sup> )	X dB/dt 0.290 millisecond time channel
SFx[23]	pV/(A*m <sup>4</sup> )	X dB/dt 0.333 millisecond time channel
SFx[24]	pV/(A*m <sup>4</sup> )	X dB/dt 0.383 millisecond time channel
SFx[25]	pV/(A*m <sup>4</sup> )	X dB/dt 0.440 millisecond time channel
SFx[26]	pV/(A*m <sup>4</sup> )	X dB/dt 0.505 millisecond time channel
SFx[27]	pV/(A*m <sup>4</sup> )	X dB/dt 0.580 millisecond time channel
SFx[28]	pV/(A*m <sup>4</sup> )	X dB/dt 0.667 millisecond time channel
SFx[29]	pV/(A*m <sup>4</sup> )	X dB/dt 0.766 millisecond time channel
SFx[30]	pV/(A*m <sup>4</sup> )	X dB/dt 0.880 millisecond time channel
SFx[31]	pV/(A*m <sup>4</sup> )	X dB/dt 1.010 millisecond time channel
SFx[32]	pV/(A*m <sup>4</sup> )	X dB/dt 1.161 millisecond time channel
SFx[33]	pV/(A*m <sup>4</sup> )	X dB/dt 1.333 millisecond time channel
SFx[34]	pV/(A*m <sup>4</sup> )	X dB/dt 1.531 millisecond time channel
SFx[35]	pV/(A*m <sup>4</sup> )	X dB/dt 1.760 millisecond time channel
SFx[36]	pV/(A*m <sup>4</sup> )	X dB/dt 2.021 millisecond time channel
SFx[37]	pV/(A*m <sup>4</sup> )	X dB/dt 2.323 millisecond time channel

Channel name	Units	Description
SFx[38]	$\text{pV}/(\text{A}\cdot\text{m}^4)$	X dB/dt 2.667 millisecond time channel
SFx[39]	$\text{pV}/(\text{A}\cdot\text{m}^4)$	X dB/dt 3.063 millisecond time channel
SFx[40]	$\text{pV}/(\text{A}\cdot\text{m}^4)$	X dB/dt 3.521 millisecond time channel
SFx[41]	$\text{pV}/(\text{A}\cdot\text{m}^4)$	X dB/dt 4.042 millisecond time channel
SFx[42]	$\text{pV}/(\text{A}\cdot\text{m}^4)$	X dB/dt 4.641 millisecond time channel
SFx[43]	$\text{pV}/(\text{A}\cdot\text{m}^4)$	X dB/dt 5.333 millisecond time channel
SFx[44]	$\text{pV}/(\text{A}\cdot\text{m}^4)$	X dB/dt 6.125 millisecond time channel
SFx[45]	$\text{pV}/(\text{A}\cdot\text{m}^4)$	X dB/dt 7.036 millisecond time channel
SFx[46]	$\text{pV}/(\text{A}\cdot\text{m}^4)$	X dB/dt 8.083 millisecond time channel
SFy	$\text{pV}/(\text{A}\cdot\text{m}^4)$	Y dB/dt data for time channels 20 to 46
BFz	$(\text{pV}\cdot\text{ms})/(\text{A}\cdot\text{m}^4)$	Z B-Field data for time channels 4 to 46
BFx	$(\text{pV}\cdot\text{ms})/(\text{A}\cdot\text{m}^4)$	X B-Field data for time channels 20 to 46
BFy	$(\text{pV}\cdot\text{ms})/(\text{A}\cdot\text{m}^4)$	Y B-Field data for time channels 20 to 46
SFxFF	$\text{pV}/(\text{A}\cdot\text{m}^4)$	Fraser Filtered X dB/dt
NchanBF		Latest time channels of B-field TAU calculation
TauBF	ms	Time constant B-Field
NchanSF		Latest time channels of dB/dt TAU calculation
TauSF	ms	Time constant dB/dt
PLM		60 Hz power line monitor

Electromagnetic B-field and dB/dt Z component data is found in array channel format between indexes 4 – 46, and X & Y component data from 20 – 46, as described above.

- Database of the Resistivity Depth Images in Geosoft GDB format, containing the following channels:

**Table 7:** Geosoft Resistivity Depth Image GDB Data Format

Channel name	Units	Description
Xg	metres	Easting NAD83 Zone 16N
Yg	metres	Northing NAD83 Zone 16N
Dist	metres	Distance from the beginning of the line
Depth	metres	array channel, depth from the surface
Z	metres	array channel, depth
AppRes	Ohm-m	array channel, Apparent Resistivity
TR	metres	EM system height
Topo	metres	digital elevation model
Radarb	metres	Calculated EM transmitter-receiver loop terrain clearance from radar altimeter
SF	$\text{pV}/(\text{A}\cdot\text{m}^4)$	array channel, Z dB/dT
MAG	nT	TMI data
CVG	nT/m	CVG data
DOI	metres	Depth of Investigation: a measure of VTEM depth effectiveness
PLM		60Hz Power Line Monitor

- Database of the VTEM Waveform “GL200223\_Waveform.gdb” in Geosoft GDB format, containing the following channels:

**Table 8:** Geosoft database for the VTEM waveform

Channel name	Units	Description
Time	milliseconds	Sampling rate interval, 5.2083 microseconds
Tx_Current	amps	Output current of the transmitter

- Geosoft Resistivity Depth Image Products:

Sections: Apparent resistivity sections along each line in .GRD and .PDF format  
 Slices: Apparent resistivity slices at selected depths from 25m to depth of investigation, at an increment of 25m in .GRD and .PDF format  
 Voxel: 3D Voxel imaging of apparent resistivity data clipped by digital elevation and depth of investigation

- Grids in Geosoft GRD and GeoTIFF format, as follows:

GL200223\_BFz30: B-Field Z Component Channel 30 (Time Gate 0.880ms)  
 GL200223\_SFxFF22: Fraser Filtered dB/dt X Component Channel 22 (Time Gate 0.290 ms)  
 GL200223\_SFz10: dB/dt Z Component Channel 10 (Time Gate 0.055 ms)  
 GL200223\_SFz25: dB/dt Z Component Channel 25 (Time Gate 0.440 ms)  
 GL200223\_SFz40: dB/dt Z Component Channel 40 (Time Gate 3.521 ms)  
 GL200223\_TauBF: B-Field Z Component, Calculated Time Constant (ms)  
 GL200223\_TauSF: dB/dt Z Component, Calculated Time Constant (ms)  
 GL200223\_TMI3: Total Magnetic Intensity (nT)  
 GL200223\_CVG: Calculated Vertical Derivative (nT/m)  
 GL200223\_Hgcxline: Measured Cross-Line Gradient (nT/m)  
 GL200223\_Hginline: Measured In-Line Gradient (nT/m)  
 GL200223\_TotHGrad: Magnetic Total Horizontal Gradient (nT/m)  
 GL200223\_TiltDrv: Magnetic Tilt derivative (radians)  
 GL200223\_DEM: Digital Elevation Model (m)  
 GL200223\_PLM: 60Hz Power Line Monitor



## 6. CONCLUSIONS AND RECOMMENDATIONS

A helicopter-borne versatile time domain electromagnetic (VTEM™plus) horizontal magnetic gradiometer geophysical survey has been completed over the Echum Project near Wawa, ON, on behalf of Kingsview Minerals Ltd.

The total area coverage is 34 km<sup>2</sup> and the total survey line coverage is 387 line-kilometres over a single block. The principal sensors included a Time Domain EM system, and a horizontal magnetic gradiometer system with two caesium magnetometers. Results have been presented as stacked profiles, and contour colour images at a scale of 1:15,000. A formal interpretation has not been included in this study, however RDI resistivity-depth imaging has been performed in support of the VTEM data.

The Echum project is located in the southeastern Wawa Greenstone Belt. The bedrock geology and exploration history of the property are not fully known by the authors. Based on the geophysical results obtained, a number of geophysical anomalies have been identified across the survey area. Magnetically, the block features a NW-SE trending band of more strongly magnetic rocks that extends through the center and more weakly magnetic rocks on the northeast, southwest and southeast edges. The central magnetic horizon contains at least two distinct lineament trends : one group striking in the NNW direction, the other in NW-SE directions. The NW-SE oriented features appear truncated/crosscut by the NNW trends, likely indicating that latter are late dyke swarms. The conductive signatures are less complex, with a prominent, strong NW oriented zone of moderate to high conductivity occurring on the southwest flank of the magnetic horizon between L1310 and L1440 and appearing to feature multiple conductive bodies. Smaller/short strike-length conductive bodies also occur along strike and nearby. Based on the EM profiles the source of most of the EM anomalies are steep to sub-vertical dipping, thin to thick conductors, with top depths of about 50 metres. Depths of investigation (DOI) vary between 200-+500m across the property.

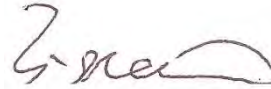
The Echum property is known to be prospective for shear-hosted gold-silver-lead and polymetallic zinc-copper mineralization is also present ([www.kingsviewminerals.ca](http://www.kingsviewminerals.ca)). It is likely that both the resistivity and the magnetic information are of exploration importance. We therefore recommend that EM anomaly picking and Maxwell plate modeling of EM anomalies be performed with test drill hole parameters planning prior to ground follow up and drill testing. More advanced 1D layered earth modeling of the EM data will prove useful in highlighting weakly anomalous resistive and conductive features of interest, both in plan and in cross-section, for targeting shear-hosted gold. Magnetic CET structural and lineament analysis as well as 3D MVI magnetic inversions will be useful for mapping structure, alteration, and lithology in 2D-3D space across the property. We recommend that more advanced, integrated interpretation be performed on these geophysical data and these results further evaluated against the known geology for future targeting.

Respectfully submitted<sup>2</sup>.



---

Marta Orta  
**Geotech Ltd.**



---

Zihao Han  
**Geotech Ltd.**



---

Jean M. Legault, M.Sc.A, P.Eng, P.Geo  
**Geotech Ltd.**



---

Emily Data  
**Geotech Ltd.**

April 2021.

---

<sup>2</sup> Final data processing of the EM and magnetic data were carried out by Zihao Han, from the offices of Geotech Ltd. in Aurora, Ontario, under the supervision of Emily Data & Jean M. Legault, M.Sc.A., P.Eng, P.Geo – Chief Geophysicist.

## APPENDIX A

### SURVEY AREA LOCATION MAP



Overview of the Survey Area

## APPENDIX B

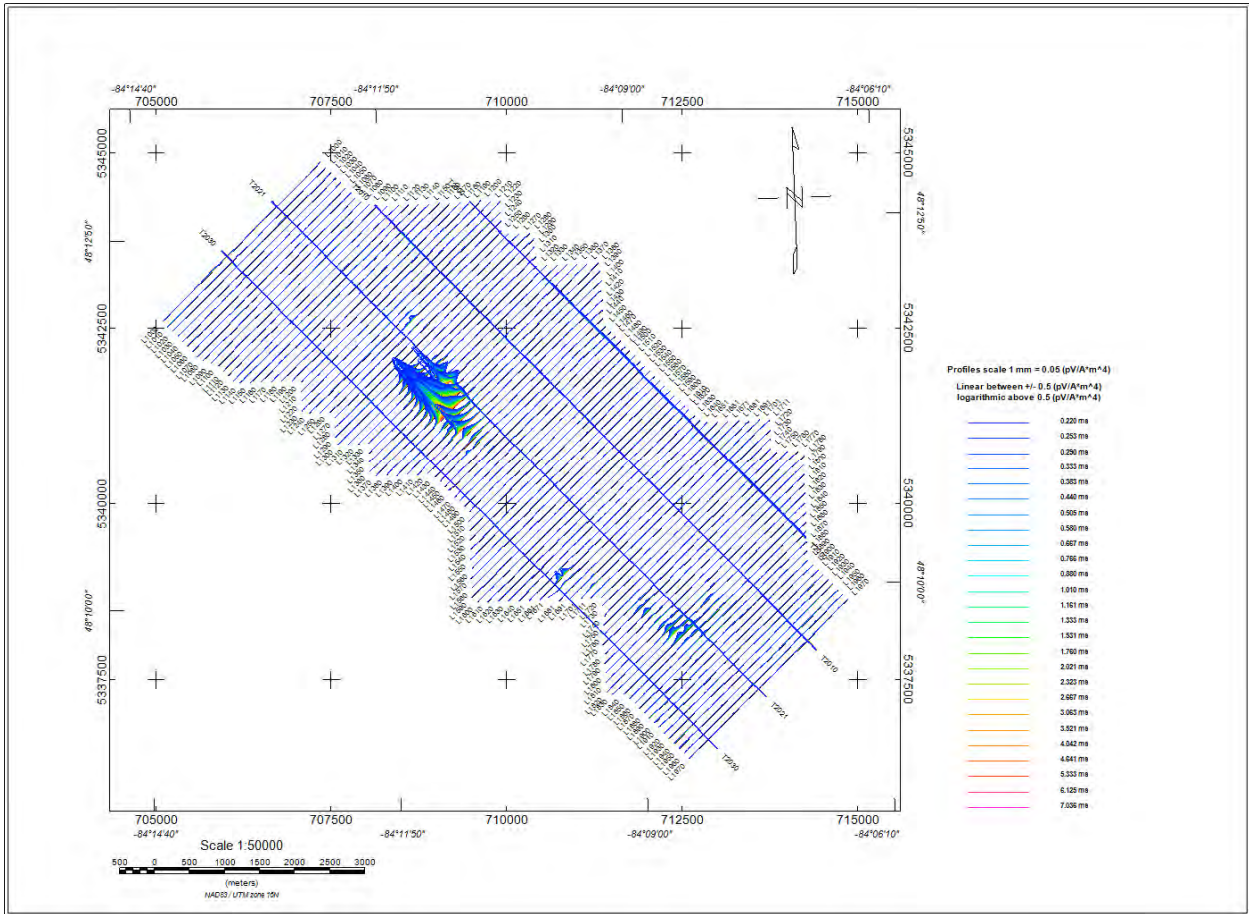
### SURVEY AREA COORDINATES

(NAD83 UTM Zone 16N)

X	Y
705098	5342660
707289	5344861
707923	5344271
709903	5344324
709903	5343875
710388	5343840
710449	5343417
711303	5343426
711338	5342555
712738	5341181
713732	5341199
713750	5340759
714190	5340750
714243	5339157
714859	5338647
712614	5336393
711761	5337300
711373	5337326
711382	5338682
709507	5338620
709472	5339896
708988	5340451
708029	5340451
708029	5340900
707509	5340891
707501	5341322
707104	5341331
707096	5341762
706215	5341745

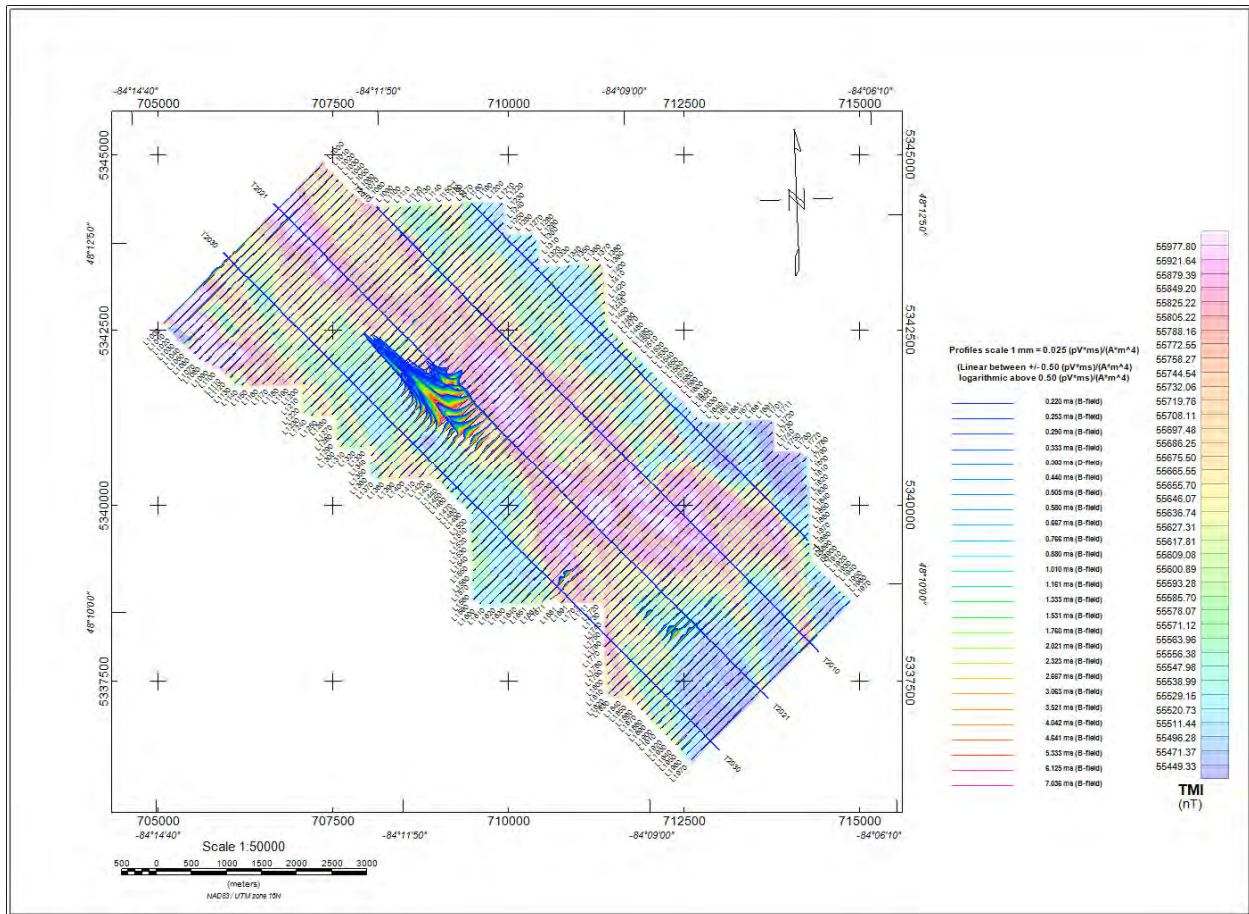


# APPENDIX C - GEOPHYSICAL MAPS<sup>1</sup>

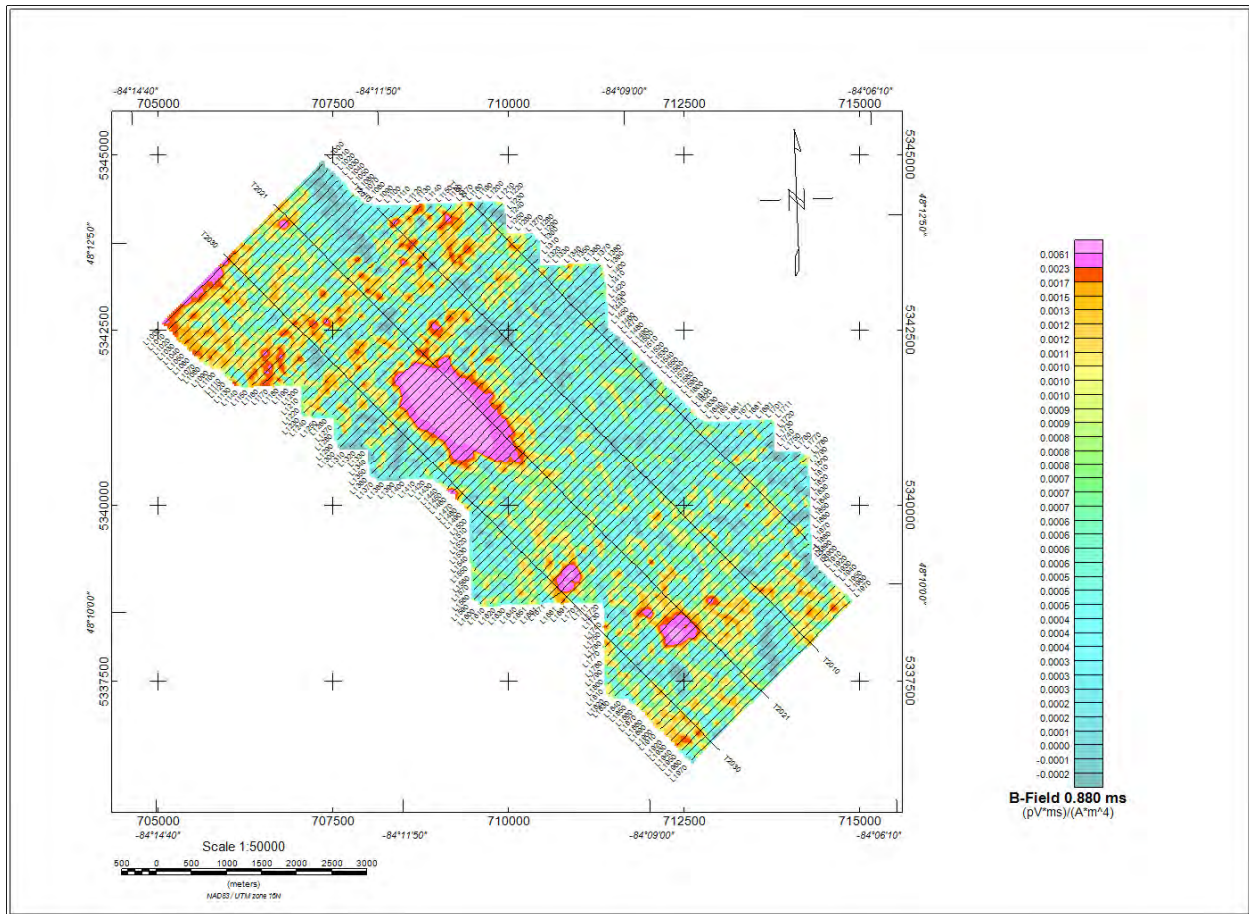


dB/dt profiles Z Component, Time Gates 0.220 – 7.036 ms

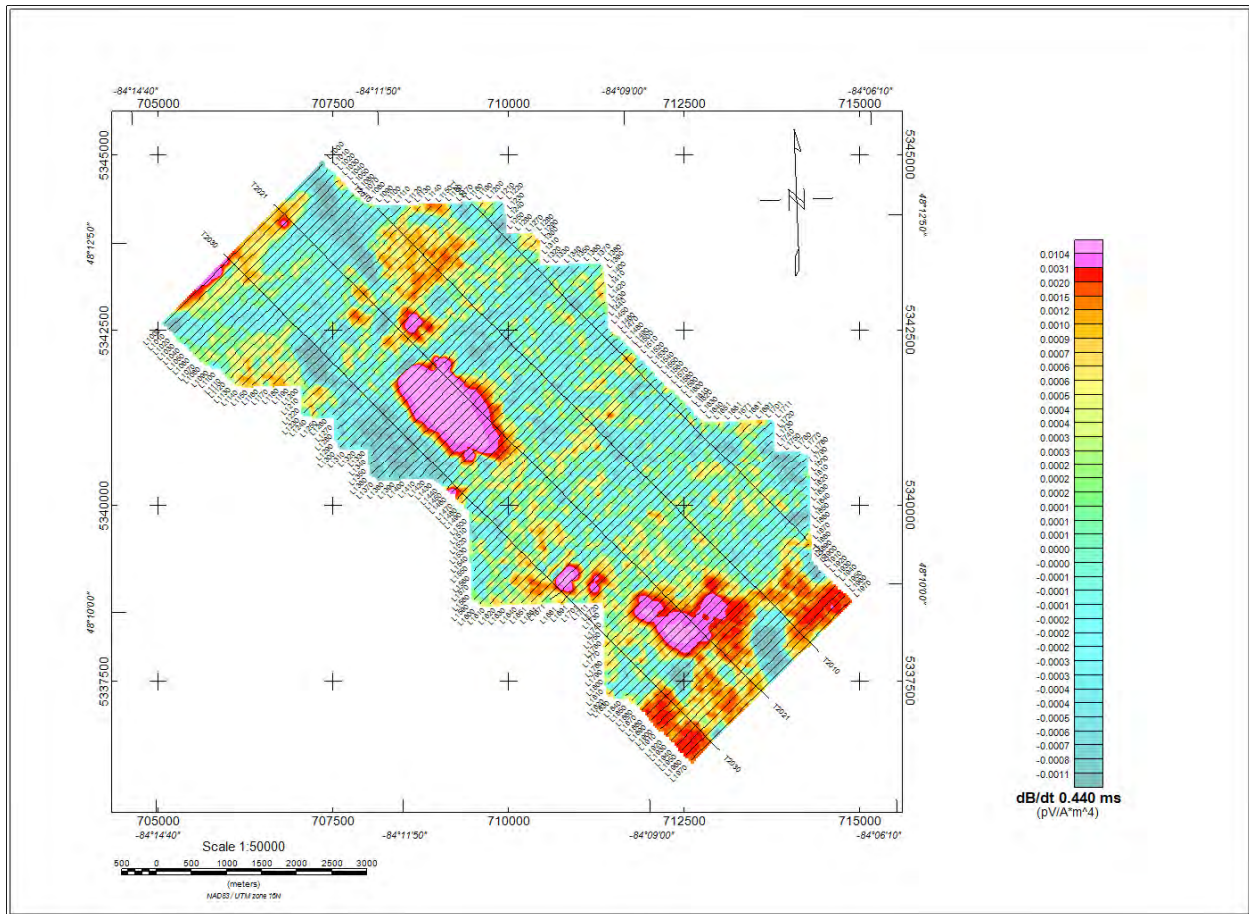
<sup>1</sup> Complete full size geophysical maps are also available in PDF format located in the final data maps folder



B-field profiles Z Component, Time Gates 0.220 – 7.036 ms over TMI colour image

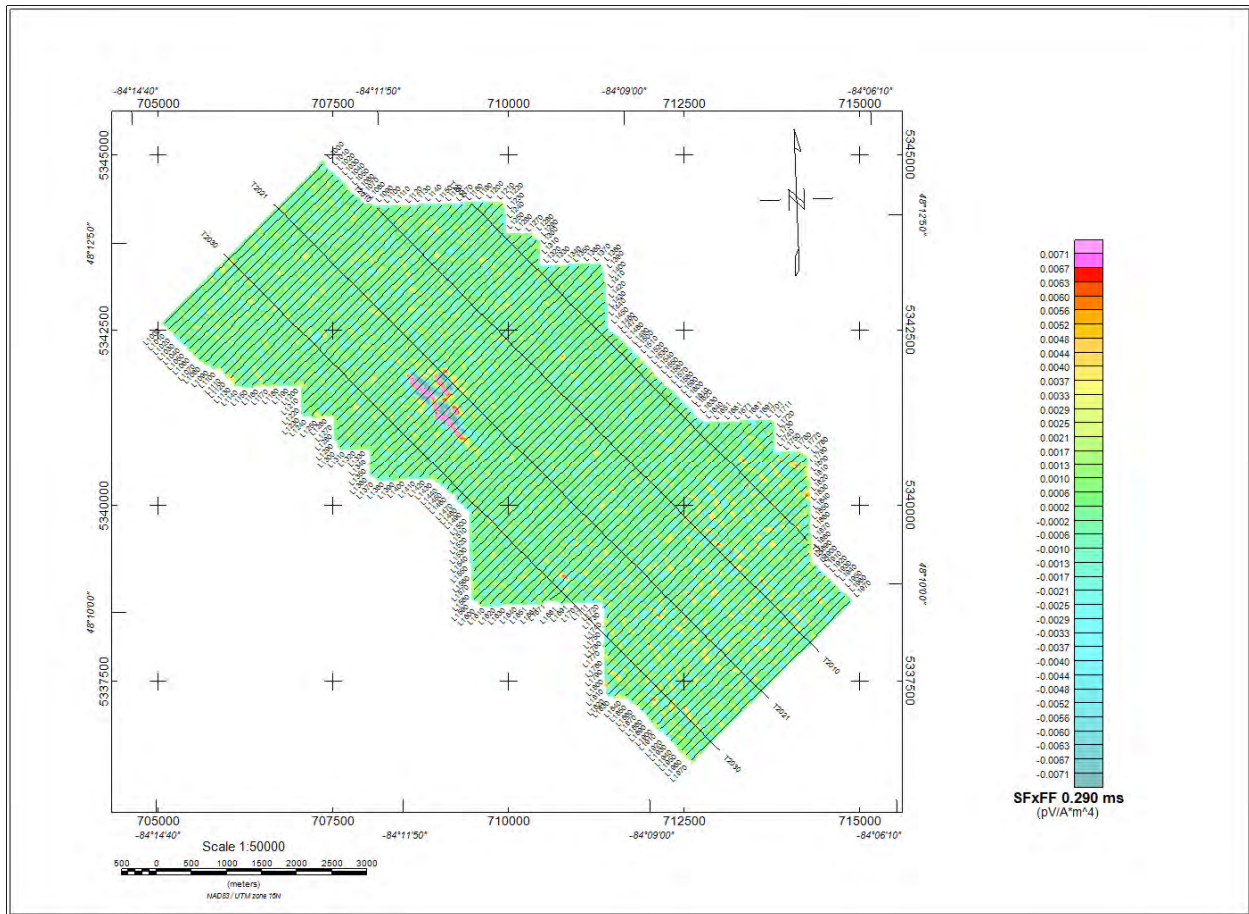


B-field Z Component Channel 30, Time Gate 0.880 ms colour image

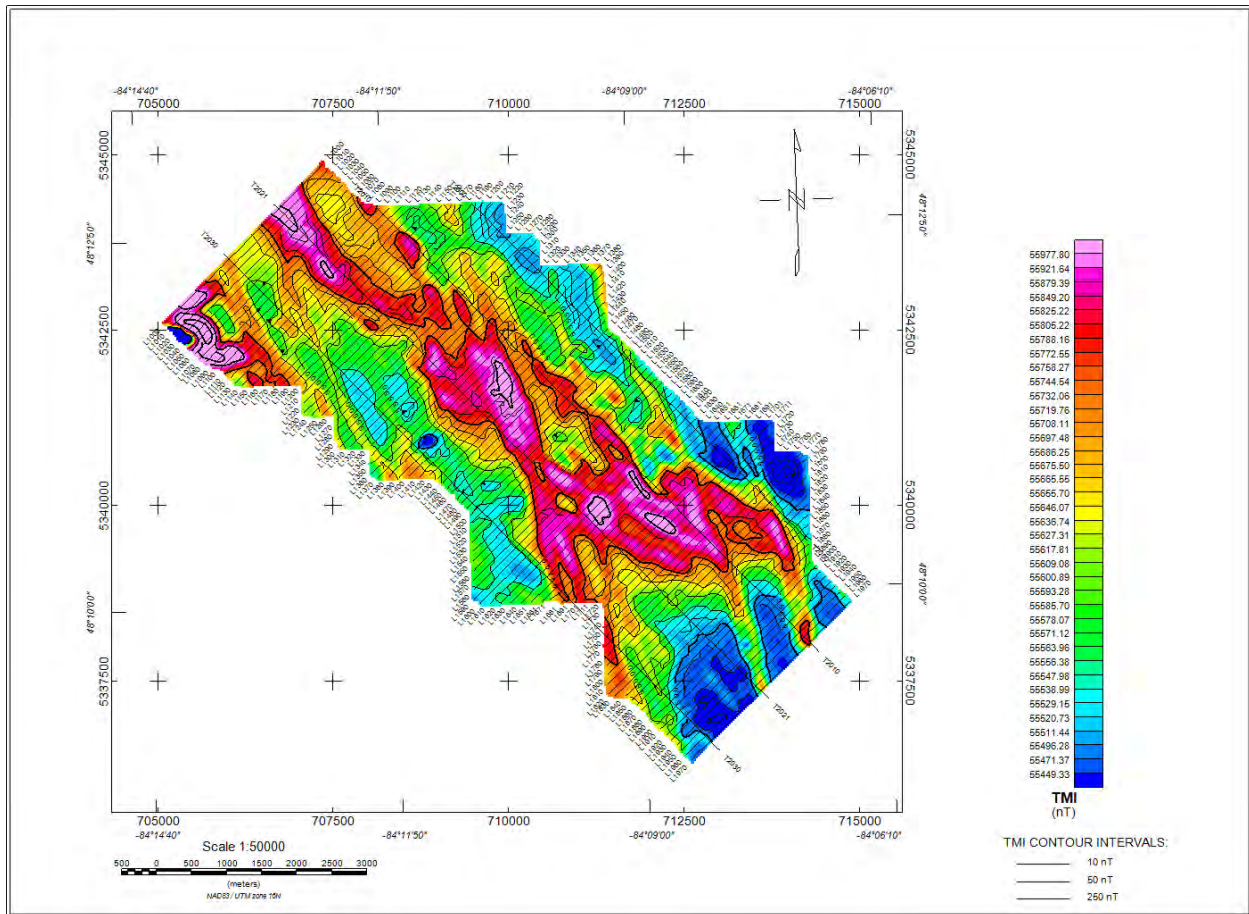


VTEM dB/dt Z Component Channel 25, Time Gate 0.440 ms colour image

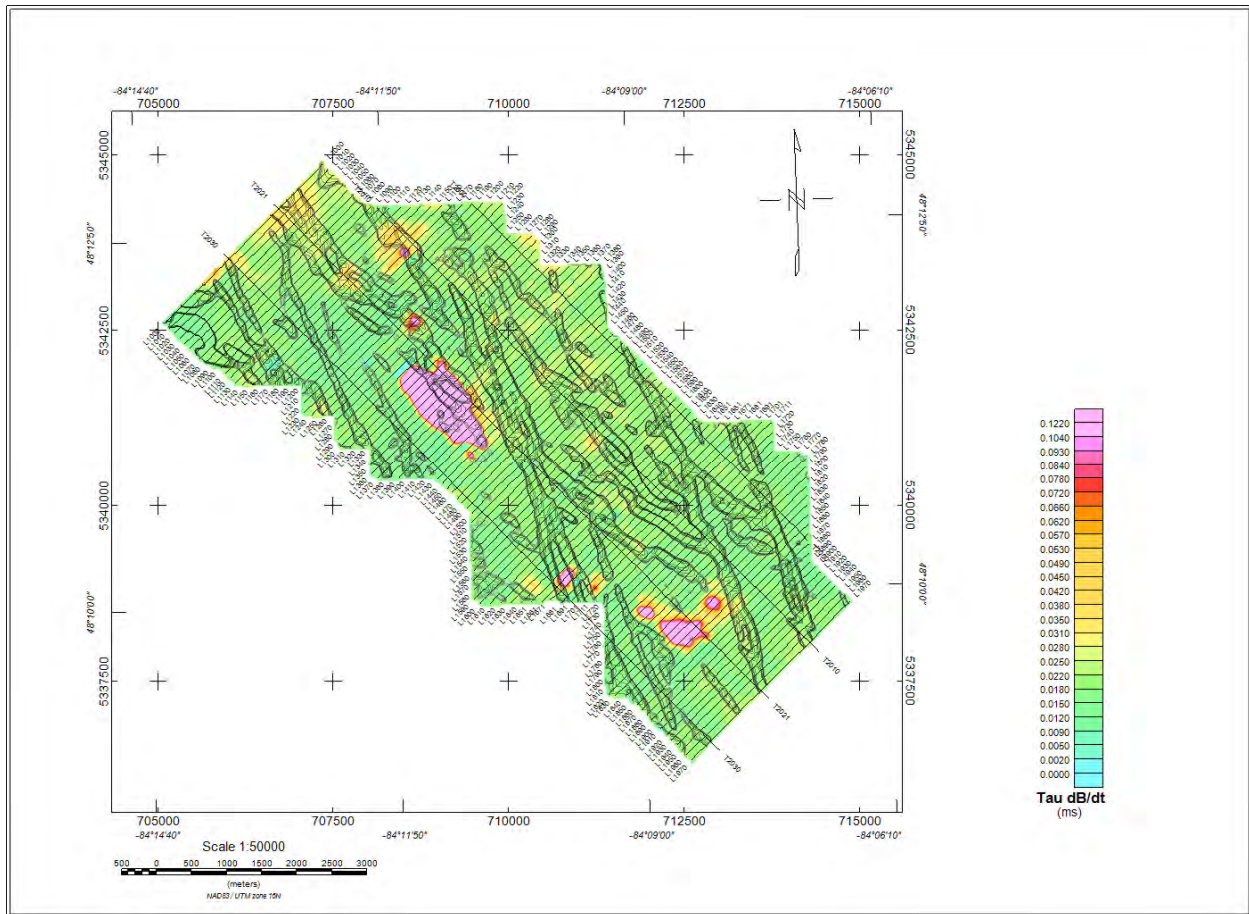




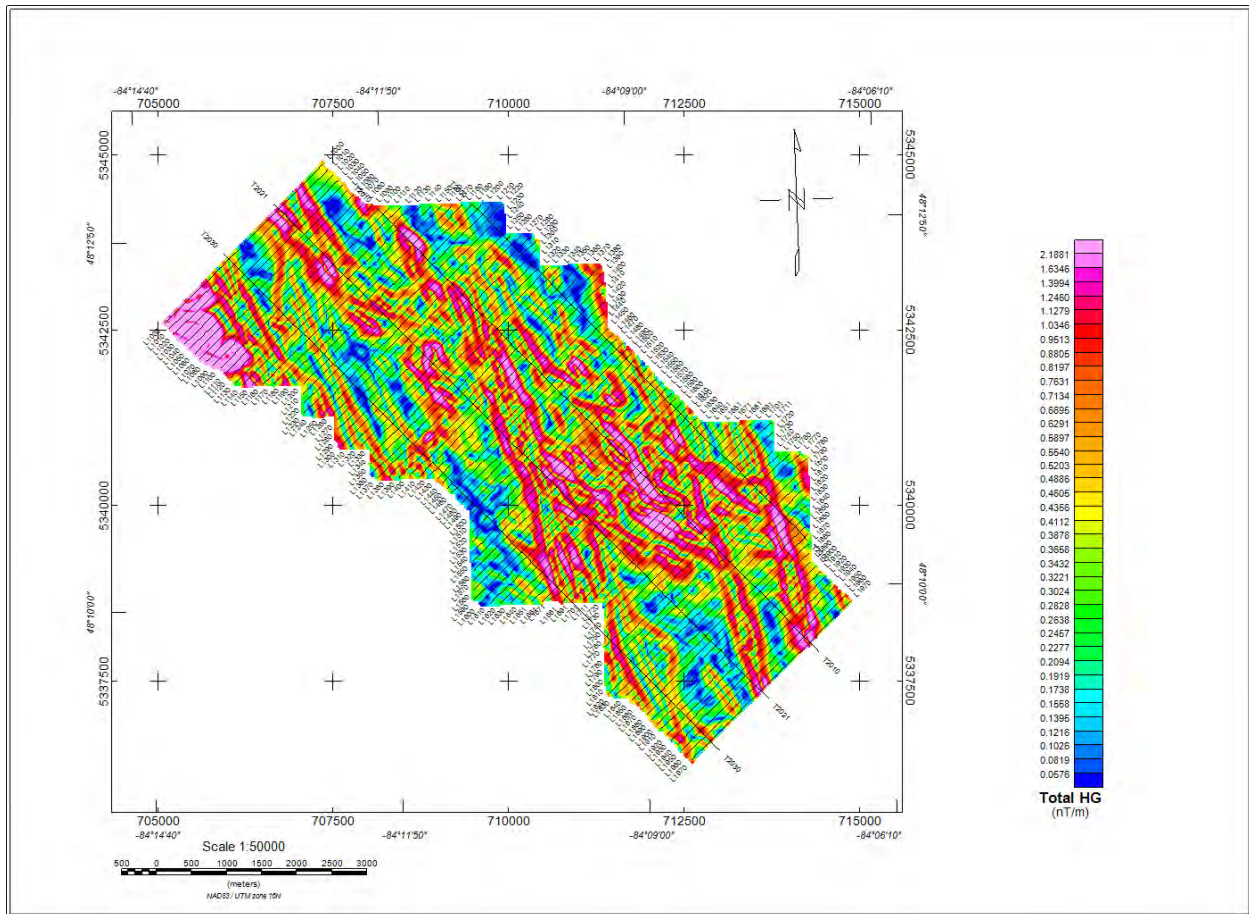
Fraser Filtered dB/dt X Component Channel 22, Time Gate 0.290 ms colour image



Total Magnetic Intensity (TMI) colour image and contours

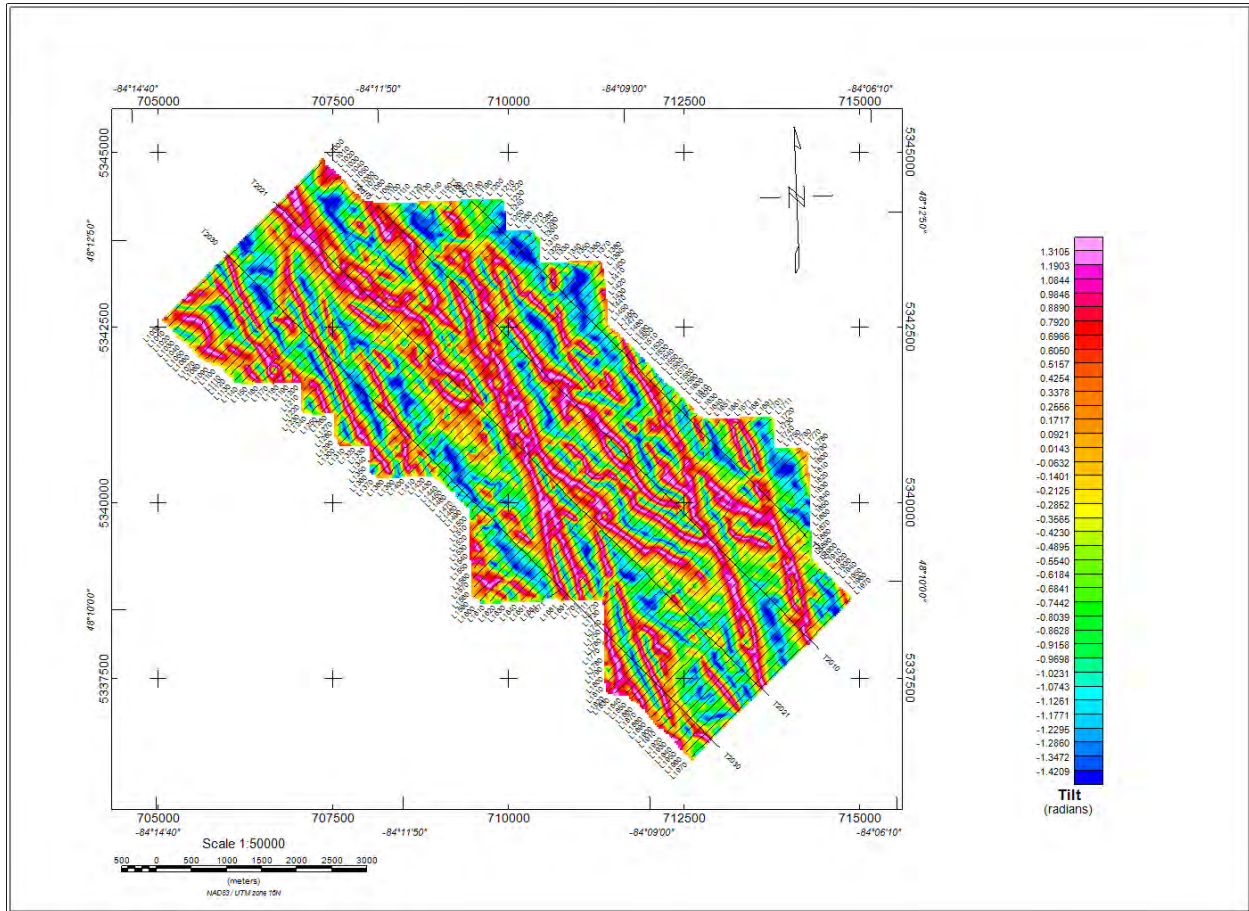


dB/dt Z-Component Calculated Time Constant (Tau) with Calculated Vertical Gradient (CVG) contours



Magnetic Total Horizontal Gradient colour image

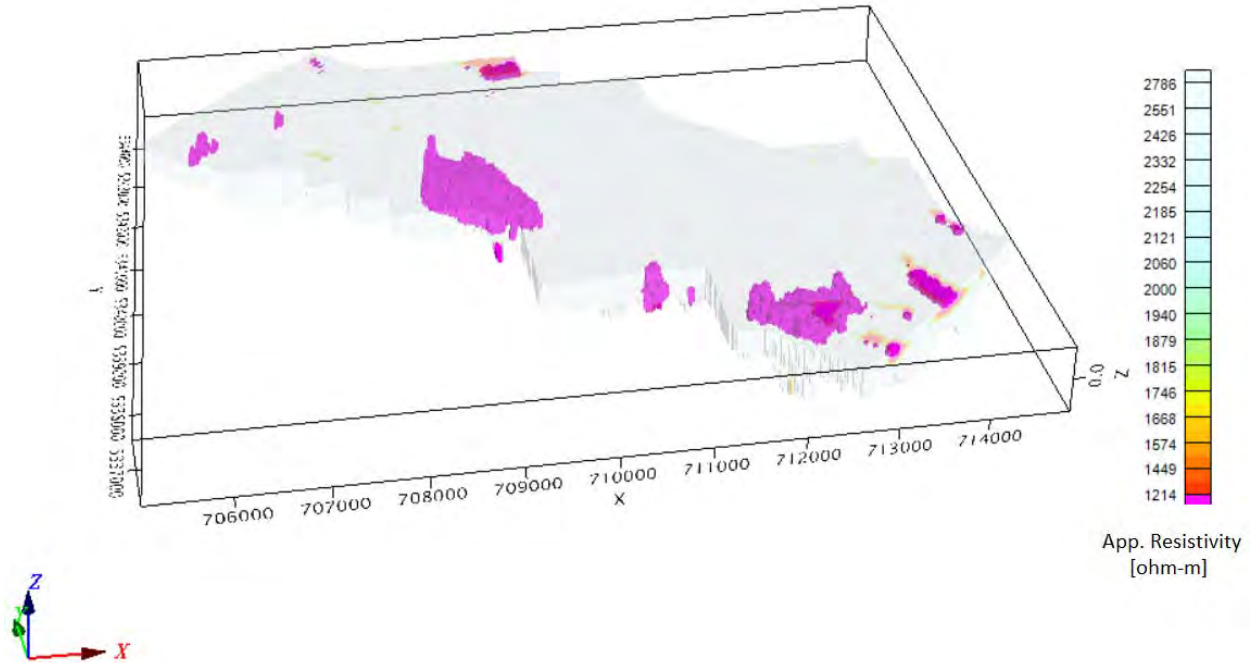




Magnetic Tilt Angle

## RESISTIVITY DEPTH IMAGE (RDI) MAPS

GL200223 VTEM Survey  
3D Apparent Resistivity View  
NAD83 / UTM zone 16N



3D View of Resistivity-Depth Image (RDI) Resistivity Voxel

## APPENDIX D

### GENERALIZED MODELING RESULTS OF THE VTEM SYSTEM INTRODUCTION

The VTEM system is based on a concentric or central loop design, whereby, the receiver is positioned at the centre of a transmitter loop that produces a primary field. The wave form is a bipolar, modified square wave with a turn-on and turn-off at each end.

During turn-on and turn-off, a time varying field is produced (dB/dt) and an electro-motive force (emf) is created as a finite impulse response. A current ring around the transmitter loop moves outward and downward as time progresses. When conductive rocks and mineralization are encountered, a secondary field is created by mutual induction and measured by the receiver at the centre of the transmitter loop.

Efficient modeling of the results can be carried out on regularly shaped geometries, thus yielding close approximations to the parameters of the measured targets. The following is a description of a series of common models made for the purpose of promoting a general understanding of the measured results.

A set of models has been produced for the Geotech VTEM™ system dB/dT Z and X components (see models D1 to D15). The Maxwell™ modeling program (EMIT Technology Pty. Ltd. Midland, WA, AU) used to generate the following responses assumes a resistive half-space. The reader is encouraged to review these models, so as to get a general understanding of the responses as they apply to survey results. While these models do not begin to cover all possibilities, they give a general perspective on the simple and most commonly encountered anomalies.

As the plate dips and departs from the vertical position, the peaks become asymmetrical.

As the dip increases, the aspect ratio (Min/Max) decreases and this aspect ratio can be used as an empirical guide to dip angles from near 90° to about 30°. The method is not sensitive enough where dips are less than about 30°.

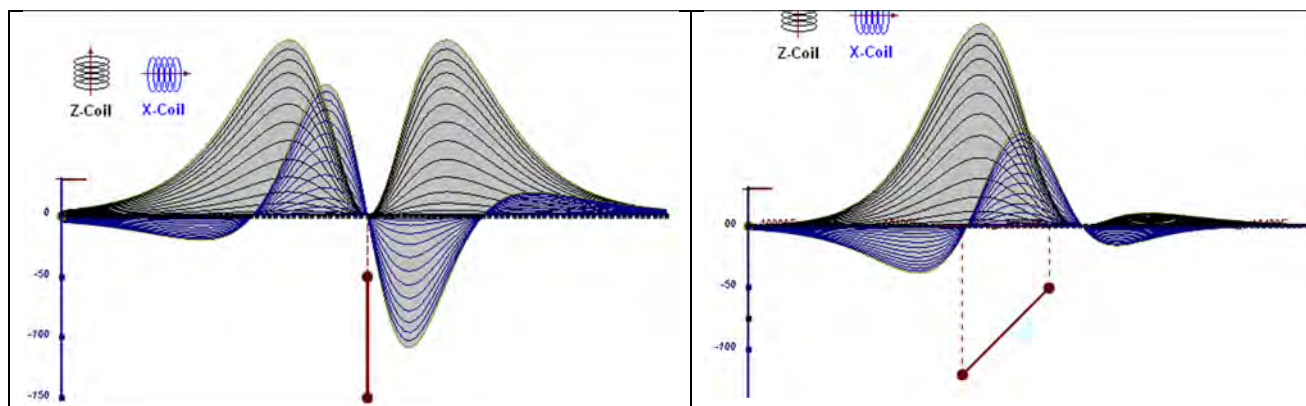


**Figure D-1:** vertical thin plate

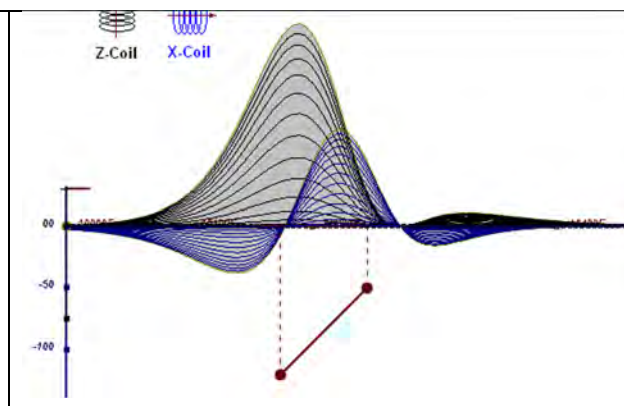


**Figure D-2:** inclined thin plate

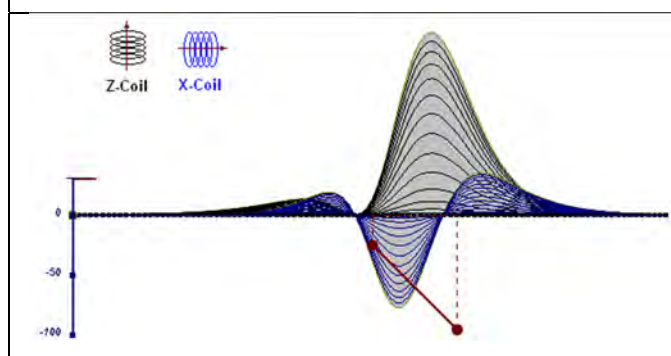


**Figure D-3:** inclined thin plate

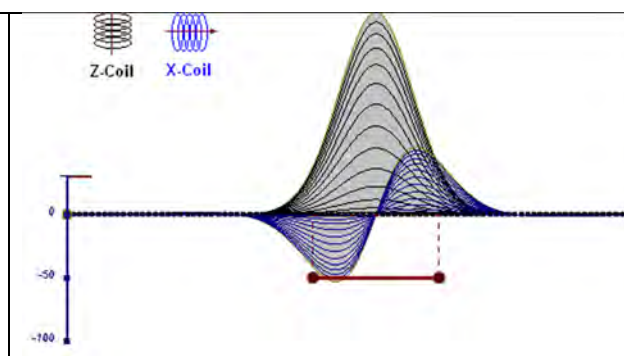


**Figure D-4:** horizontal thin plate

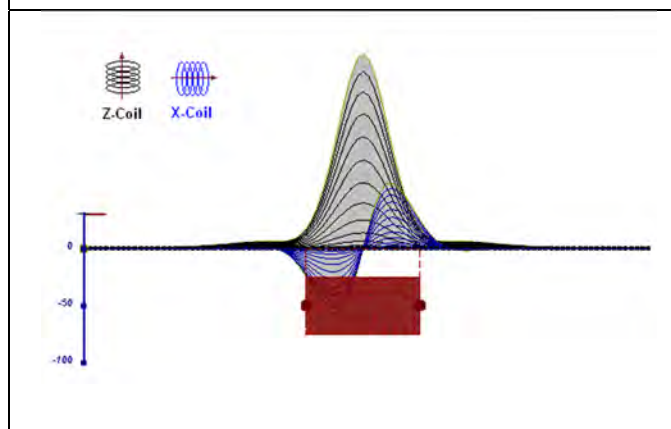


**Figure D-5:** horizontal thick plate (linear scale of the response)

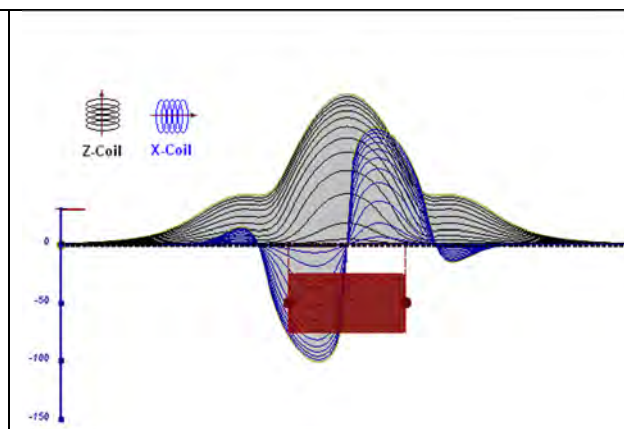


**Figure D-6:** horizontal thick plate (log scale of the response)



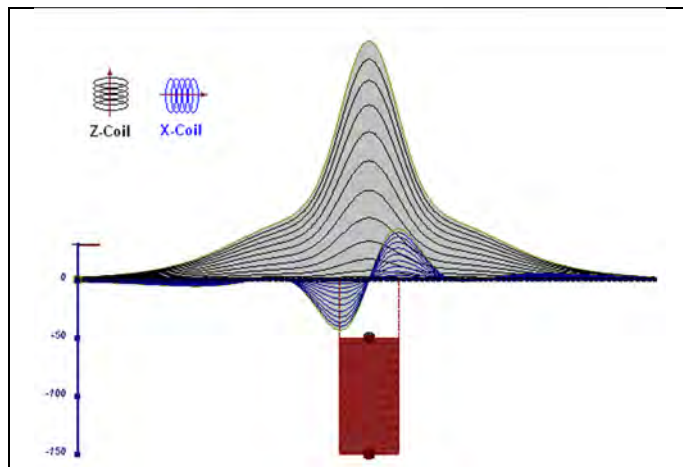


**Figure D-7:** vertical thick plate (linear scale of the response). 50 m depth

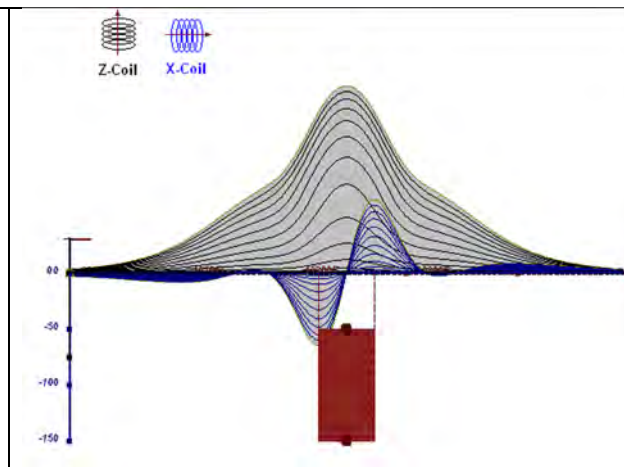


**Figure D-8:** vertical thick plate (log scale of the response). 50 m depth

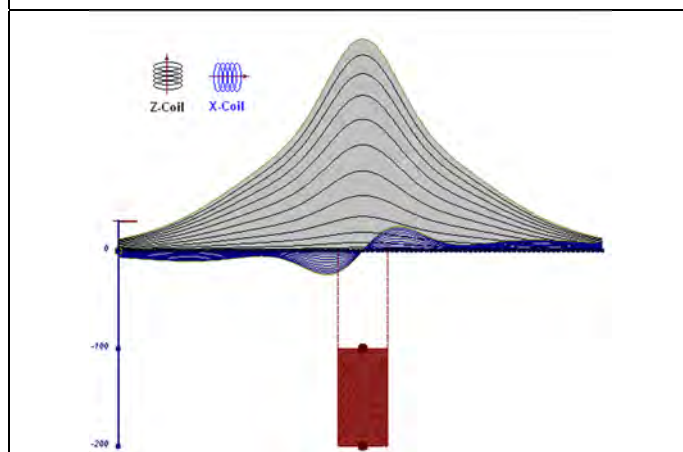


**Figure D-9:** vertical thick plate (linear scale of the response). 100 m depth

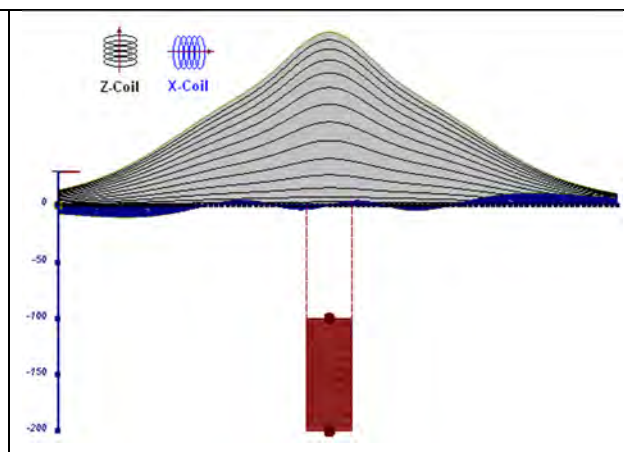


**Figure D-10:** vertical thick plate (linear scale of the response). Depth / horizontal thickness=2.5

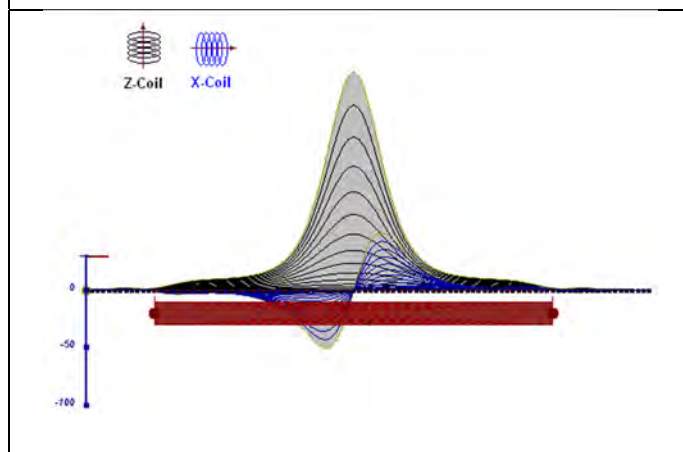


**Figure D-11:** horizontal thick plate (linear scale of the response)

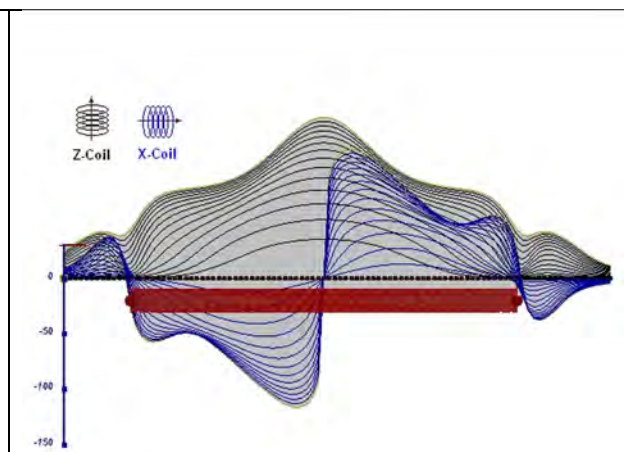


**Figure D-12:** horizontal thick plate (log scale of the response)

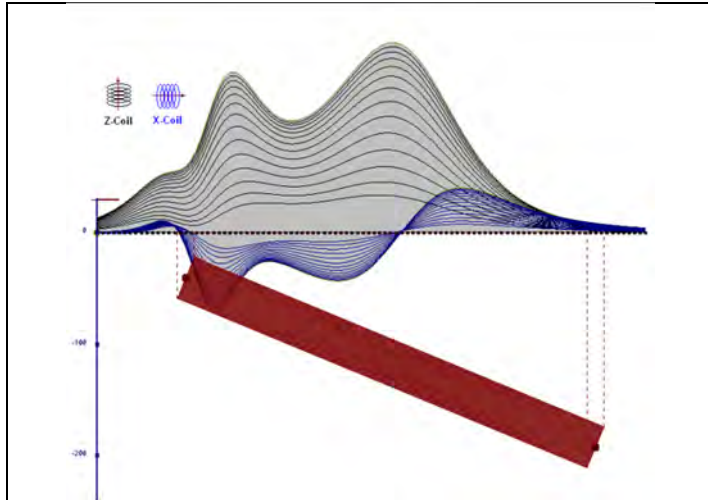


**Figure D-13:** inclined long thick plate

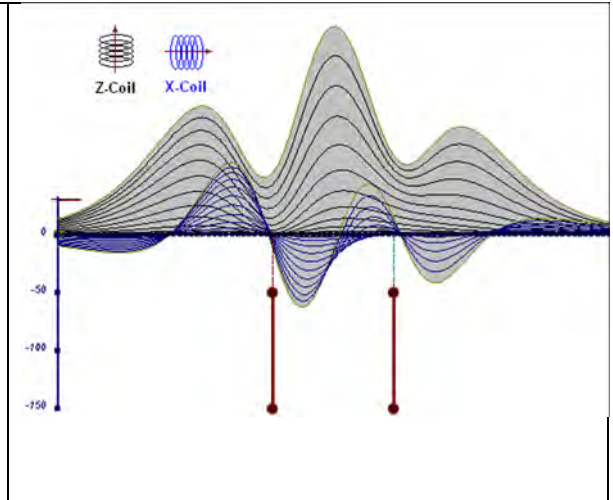


**Figure D-14:** two vertical thin plates

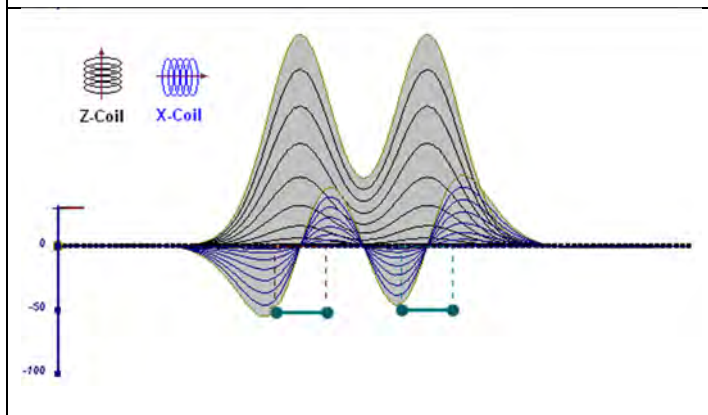


**Figure D-15:** two horizontal thin plates

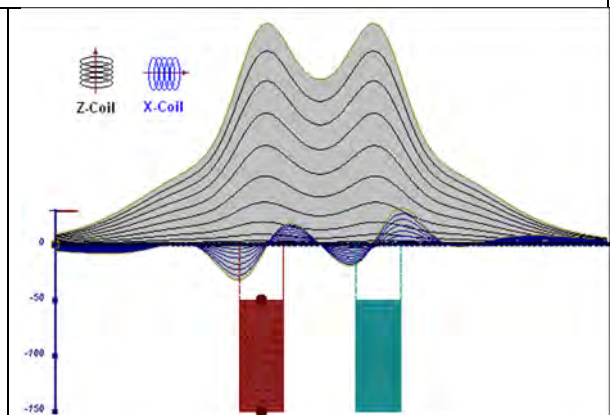


**Figure D-16:** two vertical thick plates

The same type of target but with different thickness, for example, creates different form of the response:

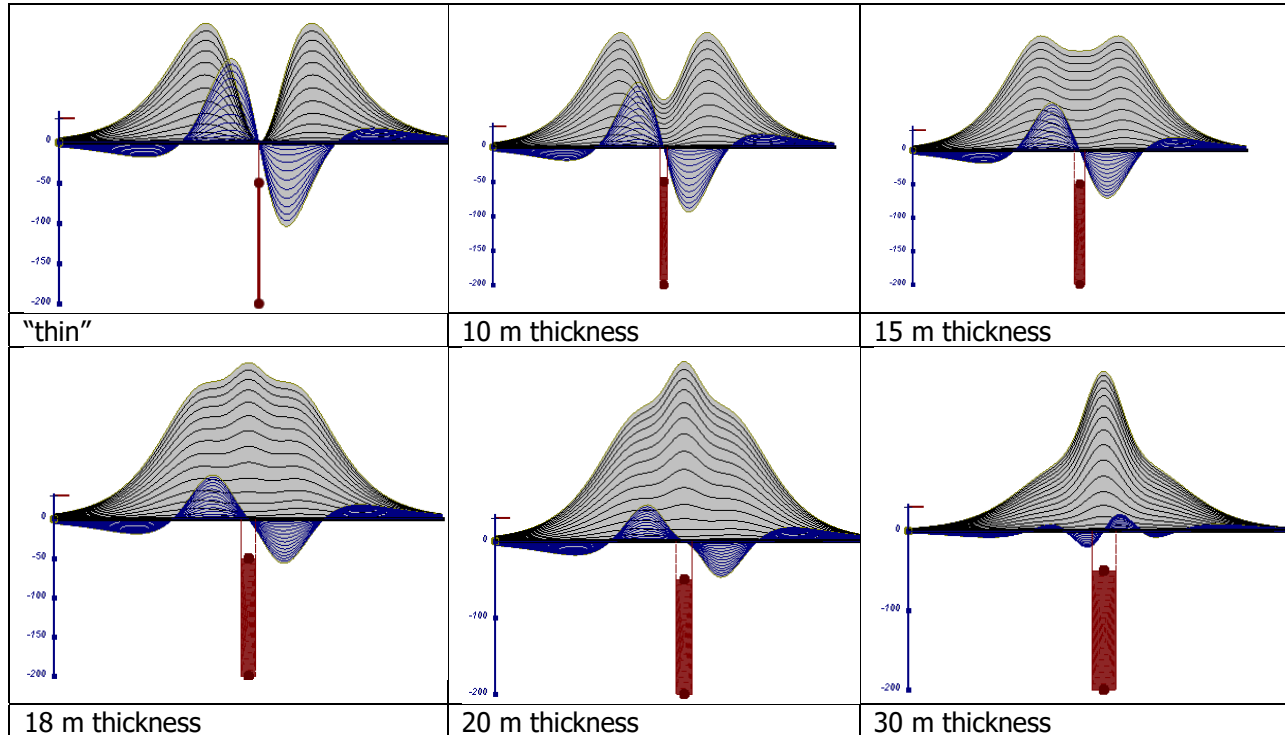


**Figure D-17:** Conductive vertical plate, depth 50 m, strike length 200 m, depth extends 150 m.

Alexander Prikhodko, PhD, P.Geol  
**Geotech Ltd.**

September 2010

## APPENDIX E

### EM TIME CONSTANT (TAU) ANALYSIS

Estimation of time constant parameter<sup>1</sup> in transient electromagnetic method is one of the steps toward the extraction of the information about conductances beneath the surface from TEM measurements.

The most reliable method to discriminate or rank conductors from overburden, background or one and other is by calculating the EM field decay time constant (TAU parameter), which directly depends on conductance despite their depth and accordingly amplitude of the response.

### THEORY

As established in electromagnetic theory, the magnitude of the electro-motive force (emf) induced is proportional to the time rate of change of primary magnetic field at the conductor. This emf causes eddy currents to flow in the conductor with a characteristic transient decay, whose Time Constant (Tau) is a function of the conductance of the survey target or conductivity and geometry (including dimensions) of the target. The decaying currents generate a proportional secondary magnetic field, the time rate of change of which is measured by the receiver coil as induced voltage during the Off time.

The receiver coil output voltage ( $e_0$ ) is proportional to the time rate of change of the secondary magnetic field and has the form,

$$e_0 \propto (1 / \tau) e^{-(t/\tau)}$$

Where,

$\tau = L/R$  is the characteristic time constant of the target (TAU)

R = resistance

L = inductance

From the expression, conductive targets that have small value of resistance and hence large value of  $\tau$  yield signals with small initial amplitude that decays relatively slowly with progress of time. Conversely, signals from poorly conducting targets that have large resistance value and small  $\tau$ , have high initial amplitude but decay rapidly with time<sup>1</sup> (Fig. E1).

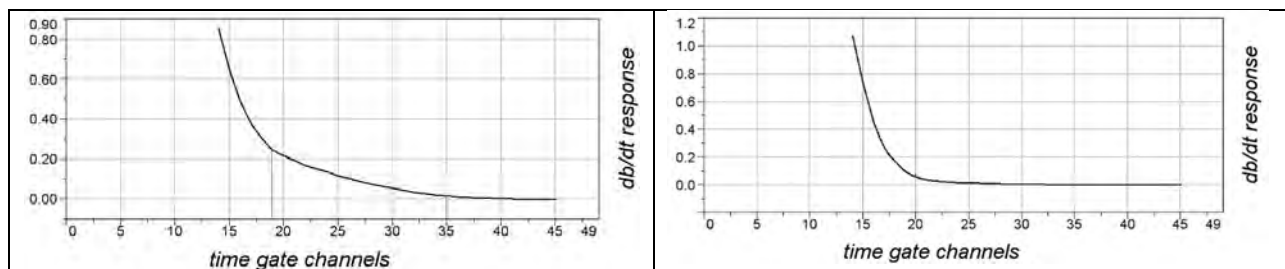


Figure E-1: Left – presence of good conductor, right – poor conductor.

<sup>1</sup> McNeill, JD, 1980, "Applications of Transient Electromagnetic Techniques", Technical Note TN-7 page 5, Geonics Limited, Mississauga, Ontario.



## EM Time Constant (Tau) Calculation

The EM Time-Constant (TAU) is a general measure of the speed of decay of the electromagnetic response and indicates the presence of eddy currents in conductive sources as well as reflecting the “conductance quality” of a source. Although TAU can be calculated using either the measured dB/dt decay or the calculated B-field decay, dB/dt is commonly preferred due to better stability (S/N) relating to signal noise. Generally, TAU calculated on base of early time response reflects both near surface overburden and poor conductors whereas, in the late ranges of time, deep and more conductive sources, respectively. For example early time TAU distribution in an area that indicates conductive overburden is shown in Figure 2.

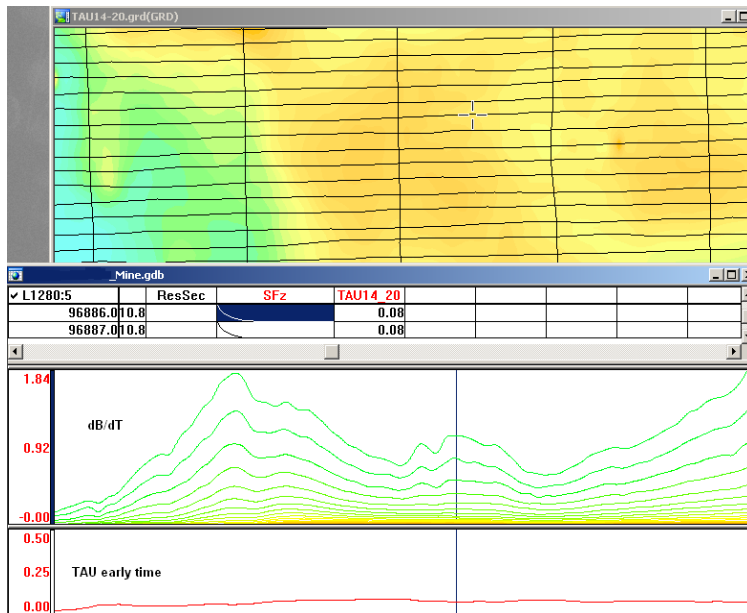


Figure E-2: Map of early time TAU. Area with overburden conductive layer and local sources.

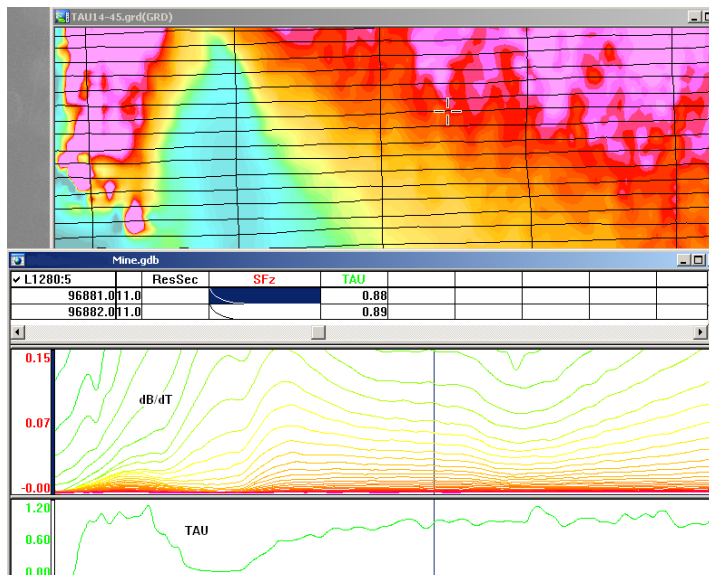


Figure E-3: Map of full-time range TAU with EM anomaly due to deep highly conductive target.

There are many advantages of TAU maps:

- TAU depends only on one parameter (conductance) in contrast to response magnitude;
- TAU is integral parameter, which covers time range and all conductive zones and targets are displayed independently of their depth and conductivity on a single map.
- Very good differential resolution in complex conductive places with many sources with different conductivity.
- Signs of the presence of good conductive targets are amplified and emphasized independently of their depth and level of response accordingly.

In the example shown in Figure 4 and 5, three local targets are defined, each of them with a different depth of burial, as indicated on the resistivity depth image (RDI). All are very good conductors but the deeper target (number 2) has a relatively weak dB/dt signal yet also features the strongest total TAU (Figure 4). This example highlights the benefit of TAU analysis in terms of an additional target discrimination tool.

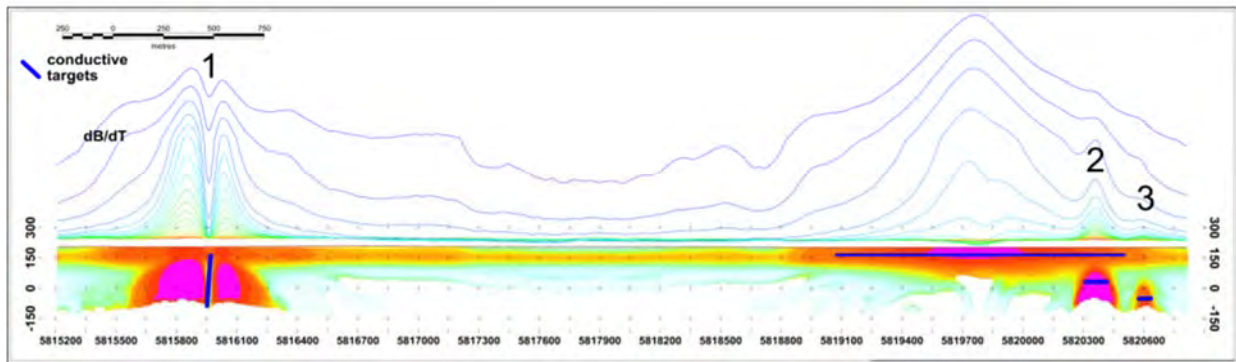


Figure E-4: dB/dt profile and RDI with different depths of targets.

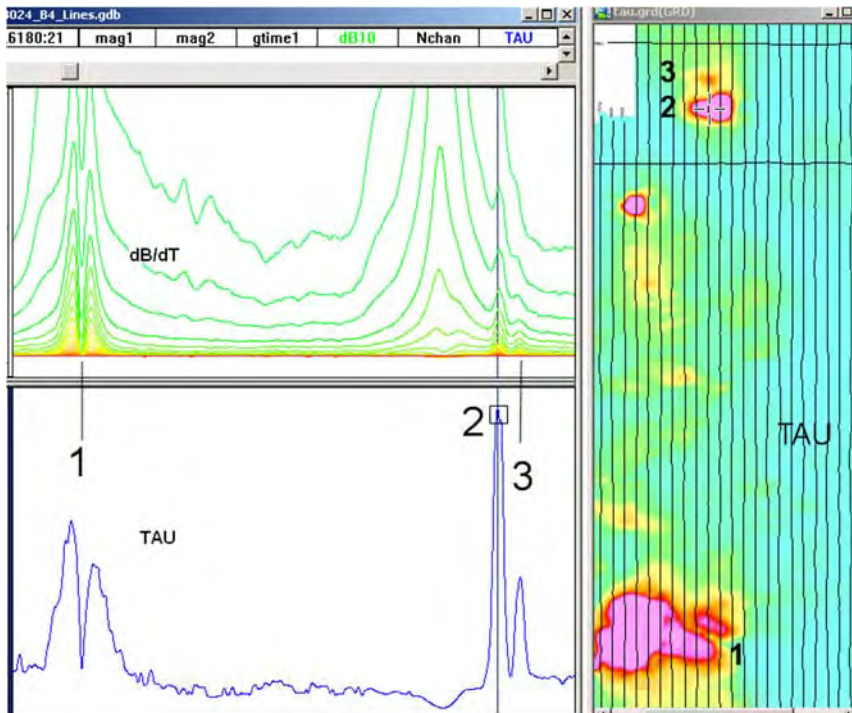


Figure E-5: Map of total TAU and dB/dt profile.

The EM Time Constants for dB/dt and B-field were calculated using the “sliding Tau” in-house program developed at Geotech2. The principle of the calculation is based on using of time window (4 time channels) which is sliding along the curve decay and looking for latest time channels which have a response above the level of noise and decay. The EM decays are obtained from all available decay channels, starting at the latest channel. Time constants are taken from a least square fit of a straight-line (log/linear space) over the last 4 gates above a pre-set signal threshold level (Figure F6). Threshold settings are pointed in the “label” property of TAU database channels. The sliding Tau method determines that, as the amplitudes increase, the time-constant is taken at progressively later times in the EM decay. Conversely, as the amplitudes decrease, Tau is taken at progressively earlier times in the decay. If the maximum signal amplitude falls below the threshold or becomes negative for any of the 4 time gates, then Tau is not calculated and is assigned a value of “dummy” by default.

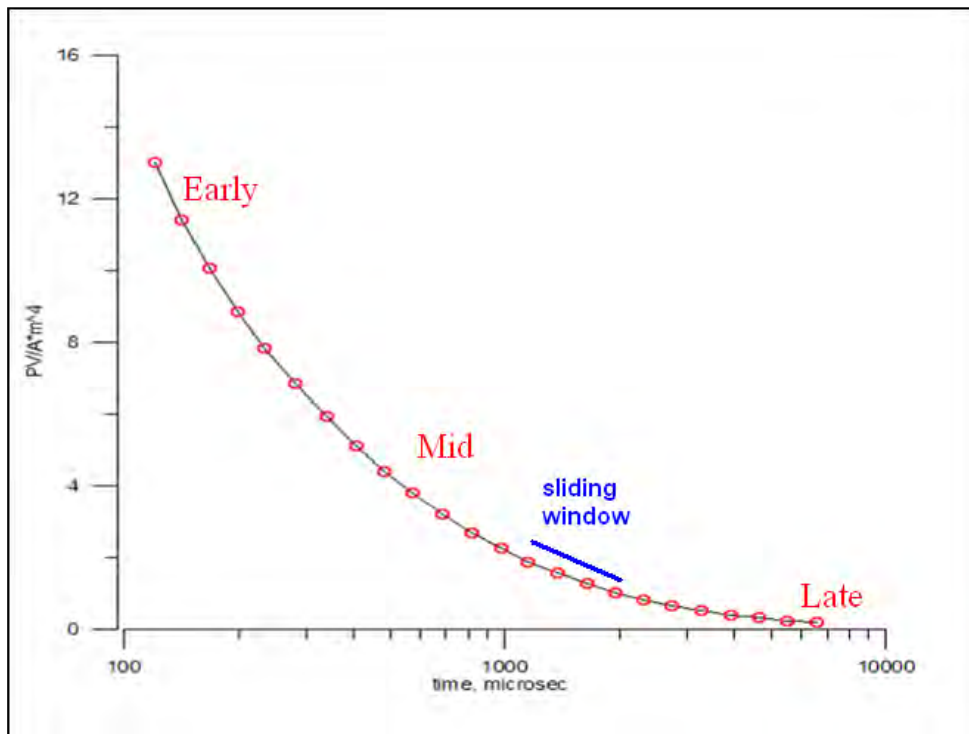


Figure E-6: Typical dB/dt decays of Vtem data

Alexander Prikhodko, PhD, P.Geo  
**Geotech Ltd.**

September 2010

<sup>2</sup> by A.Prikhodko

## APPENDIX F

### TEM RESISTIVITY DEPTH IMAGING (RDI)

Resistivity depth imaging (RDI) is a technique used to rapidly convert EM profile decay data into an equivalent resistivity versus depth cross-section, by deconvolving the measured TEM data. The used RDI algorithm of Resistivity-Depth transformation is based on the scheme of the apparent resistivity transform of Maxwell A. Meju (1998)<sup>1</sup> and TEM response from a conductive half-space. The program is developed by Alexander Prikhodko and is depth-calibrated based on forward plate modeling for VTEM system configuration (Fig. 1-10).

RDIs provide reasonable indications of conductor relative depth and vertical extent, as well as accurate 1D layered-earth apparent conductivity/resistivity structure across VTEM flight lines. Approximate depth of investigation of a TEM system, image of secondary field distribution in half-space, effective resistivity, initial geometry and position of conductive targets is the information obtained on the basis of the RDIs.

Maxwell forward modeling with RDI sections from the synthetic responses (VTEM system).

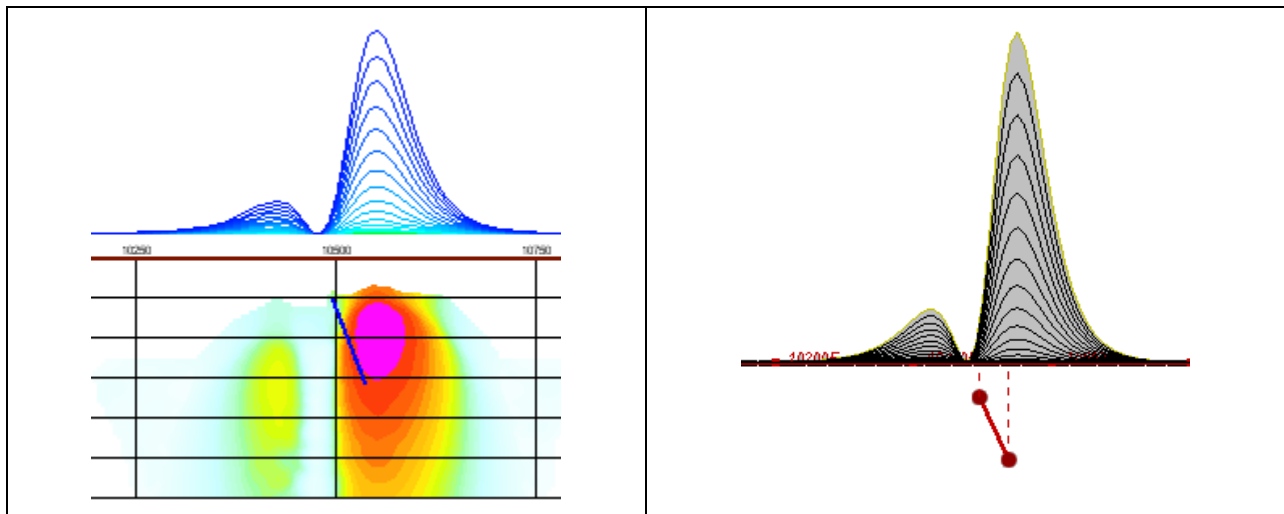


**Figure F-1:** Maxwell plate model and RDI from the calculated response for a conductive "thin" plate (depth 50 m, dip 65 degrees, depth extend 100 m).

<sup>1</sup> Maxwell A. Meju, 1998, Short Note: A simple method of transient electromagnetic data analysis, *Geophysics*, **63**, 405–410.



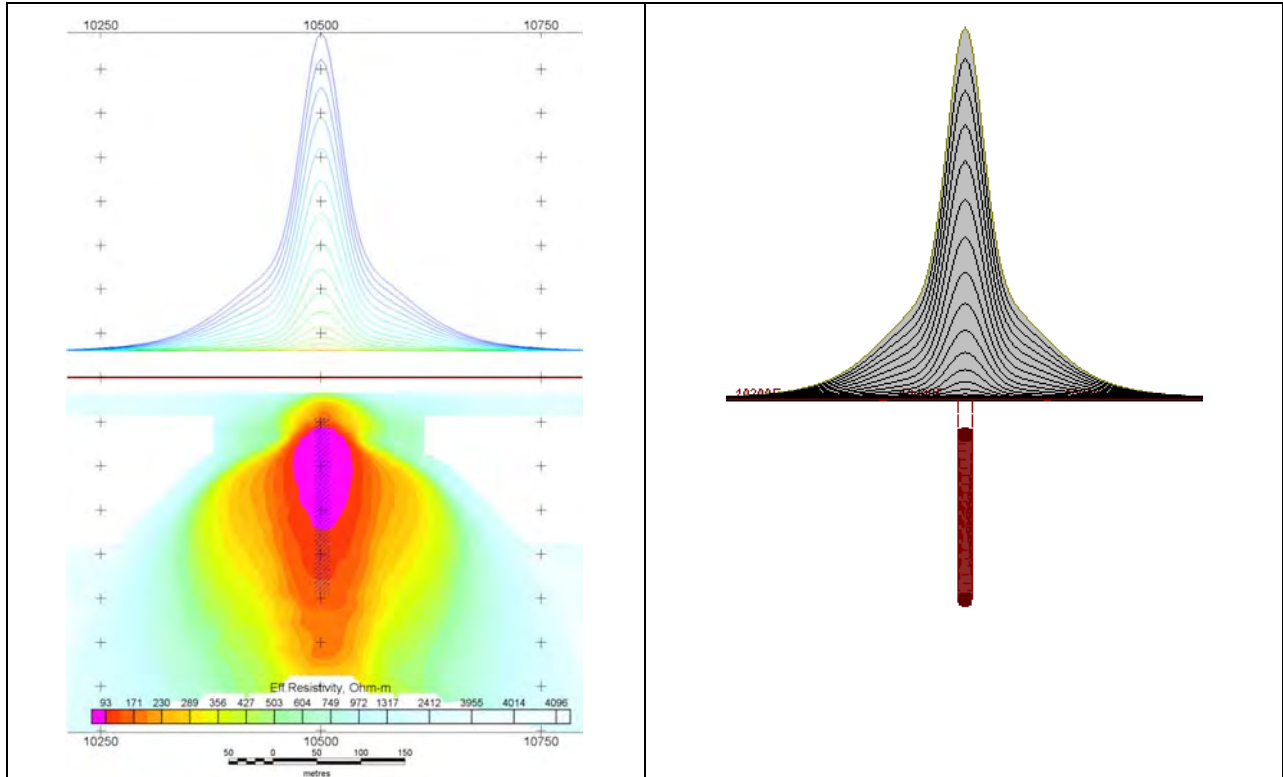


Figure F-2: Maxwell plate model and RDI from the calculated response for "thick" plate 18 m thickness, depth 50 m, depth extend 200 m).

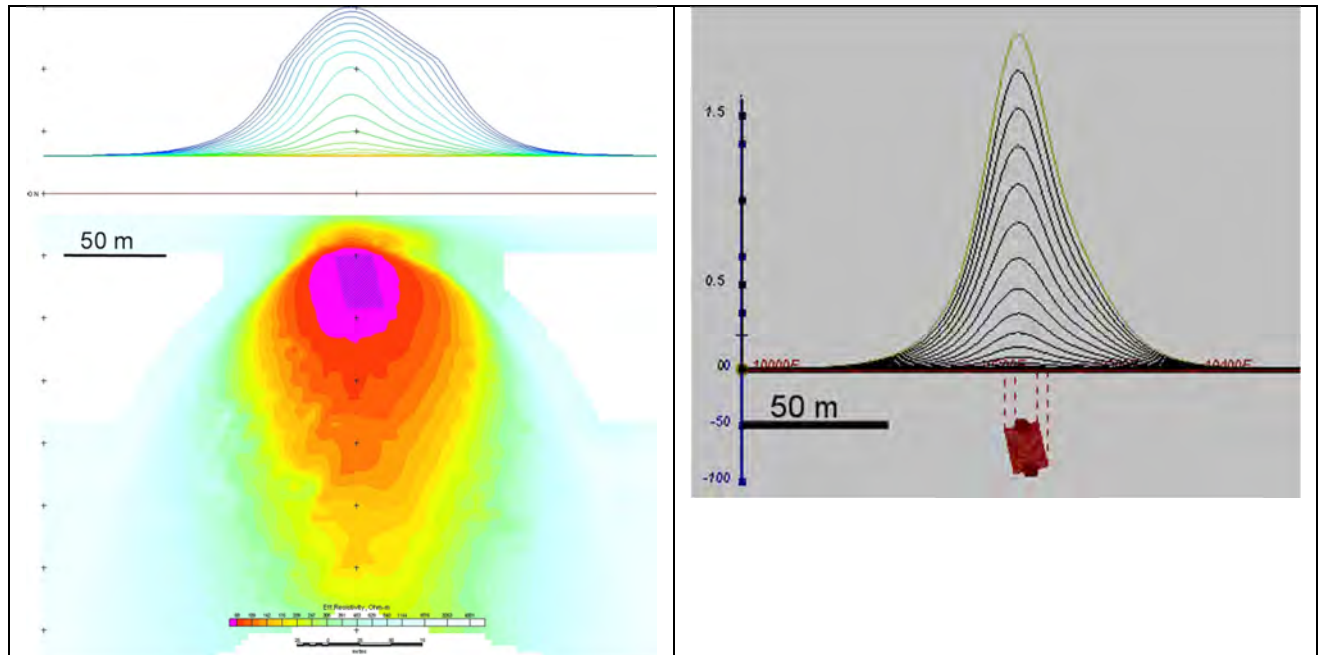


Figure F-3: Maxwell plate model and RDI from the calculated response for bulk ("thick") 100 m length, 40 m depth extend, 30 m thickness.

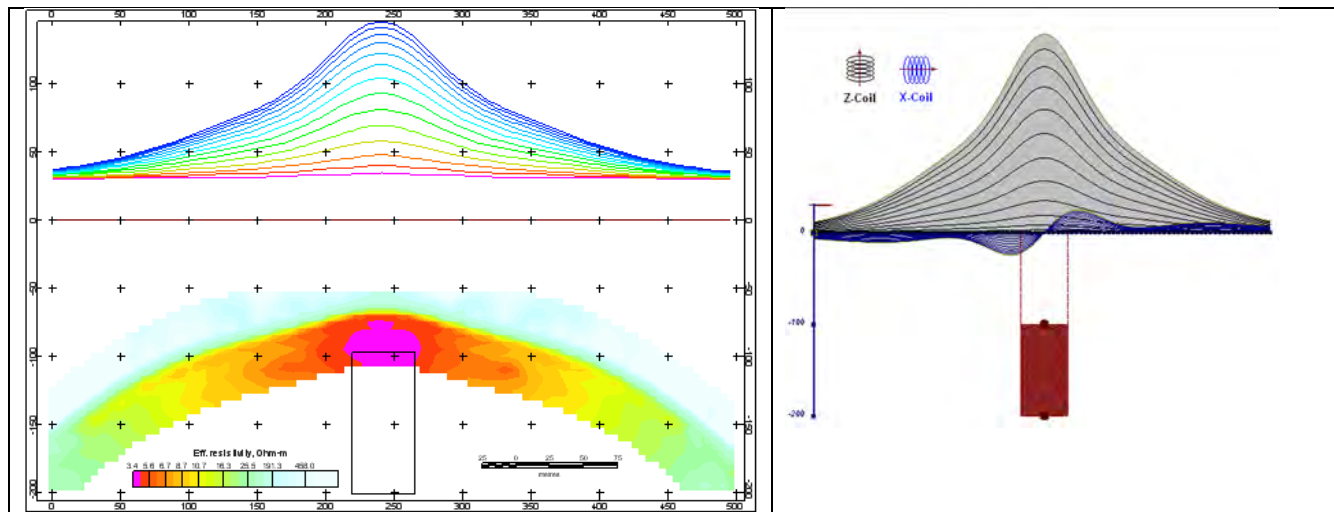


Figure F-4: Maxwell plate model and RDI from the calculated response for "thick" vertical target (depth 100 m, depth extend 100 m). 19-44 chan.

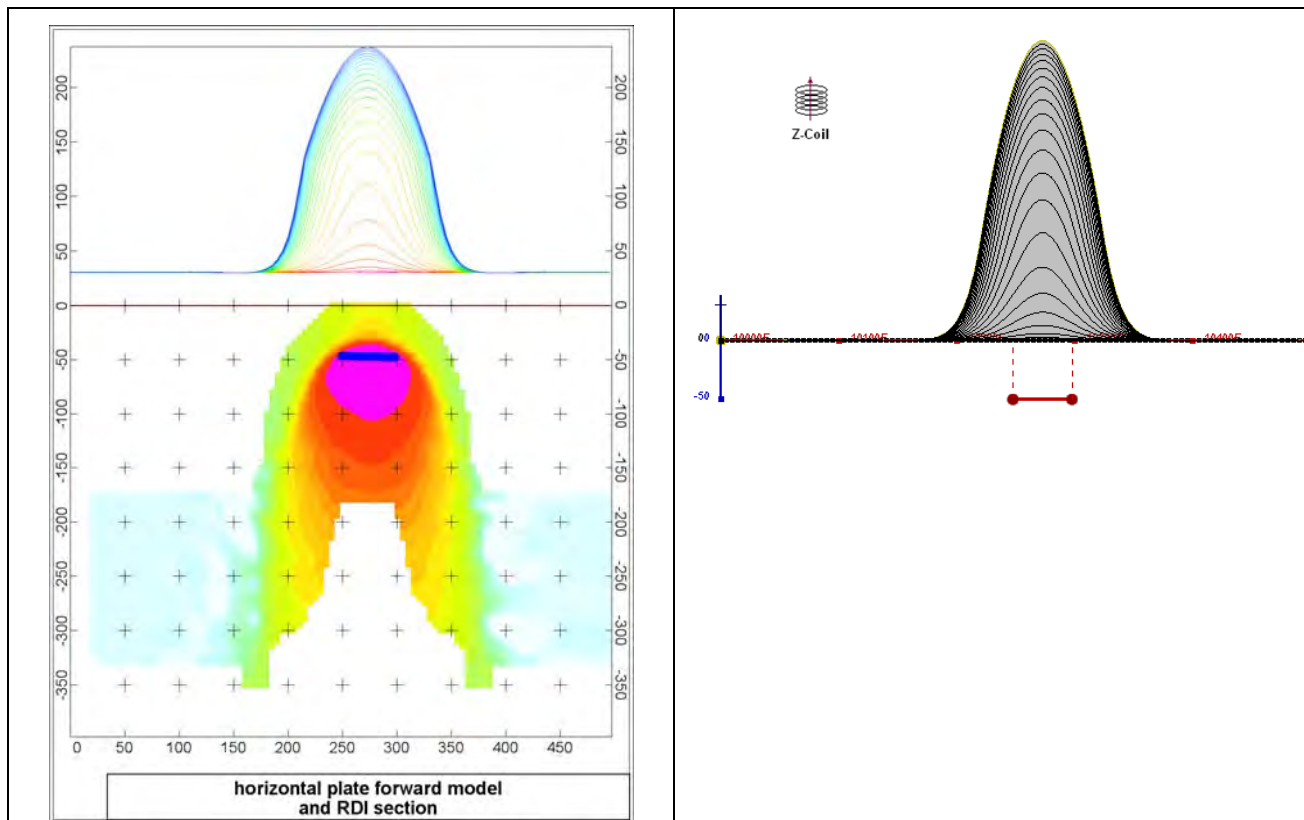


Figure F-5: Maxwell plate model and RDI from the calculated response for horizontal thin plate (depth 50 m, dim 50x100 m). 15-44 chan.

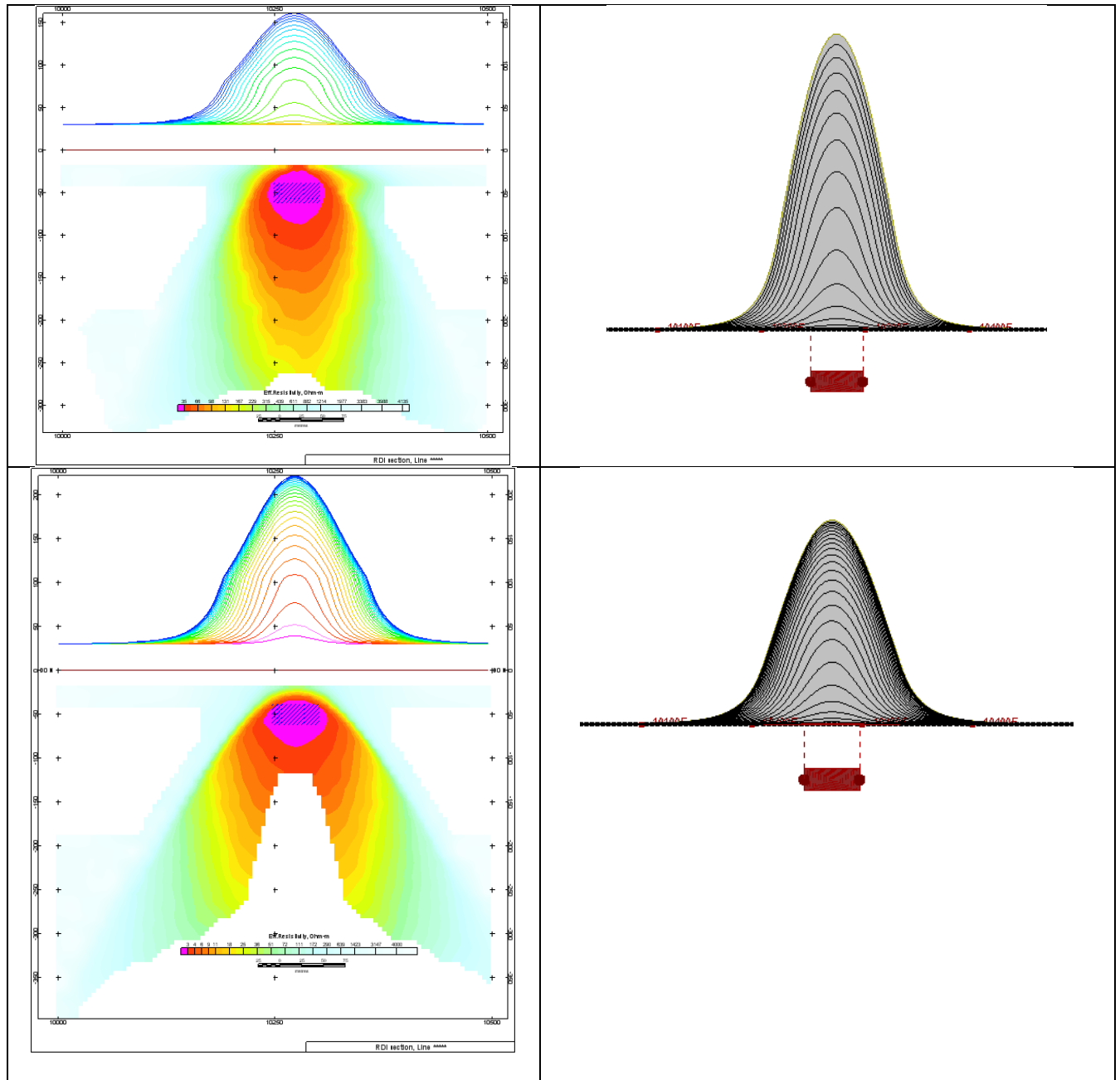


Figure F-6: Maxwell plate model and RDI from the calculated response for horizontal thick (20m) plate – less conductive (on the top), more conductive (below).

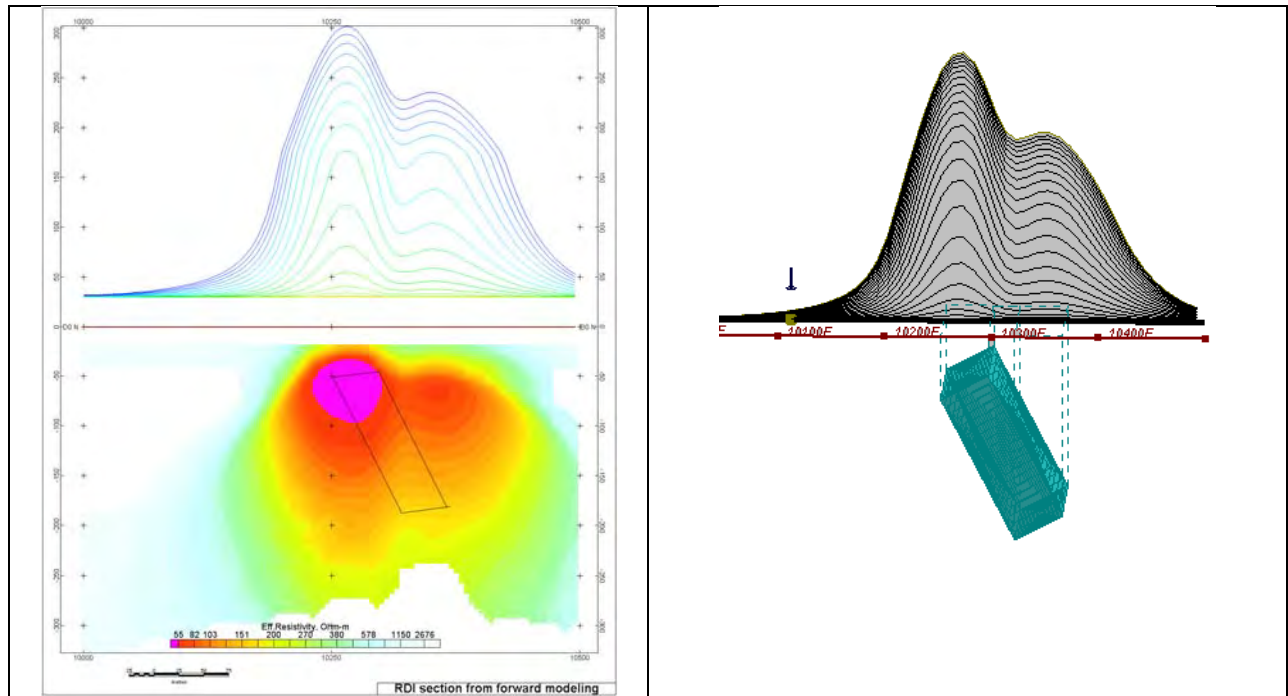


Figure F-7: Maxwell plate model and RDI from the calculated response for inclined thick (50m) plate. Depth extends 150 m, depth to the target 50 m.

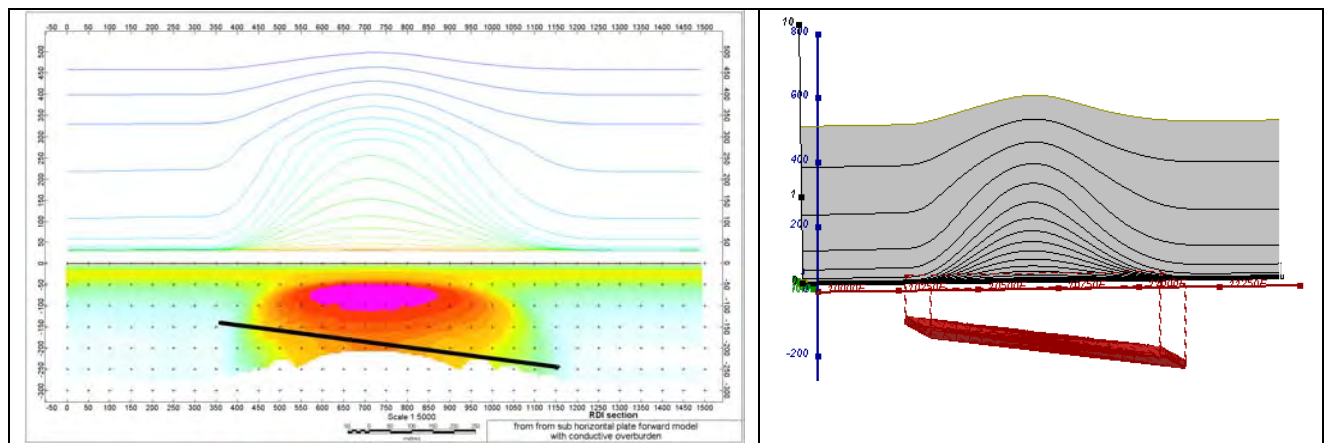


Figure F-8: Maxwell plate model and RDI from the calculated response for the long, wide and deep subhorizontal plate (depth 140 m, dim 25x500x800 m) with conductive overburden.



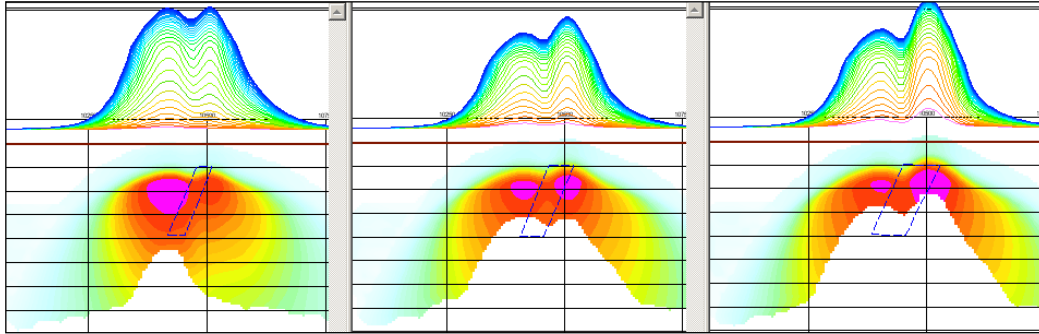


Figure F-9: Maxwell plate models and RDIs from the calculated response for "thick" dipping plates (35, 50, 75 m thickness), depth 50 m, conductivity 2.5 S/m.

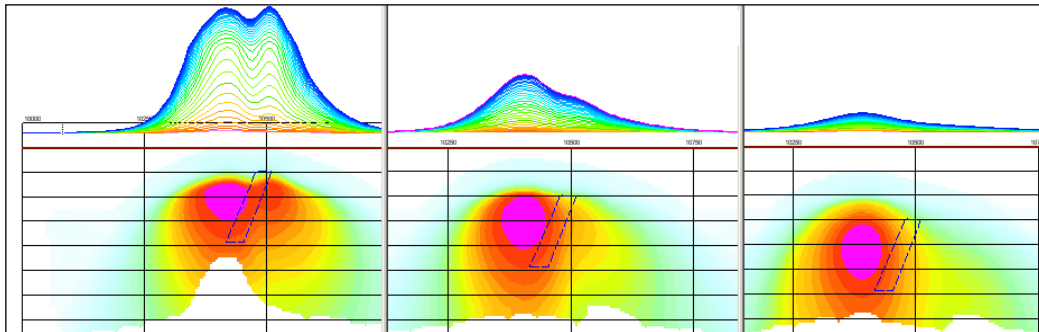


Figure F-10: Maxwell plate models and RDIs from the calculated response for "thick" (35 m thickness) dipping plate on different depth (50, 100, 150 m), conductivity 2.5 S/m.

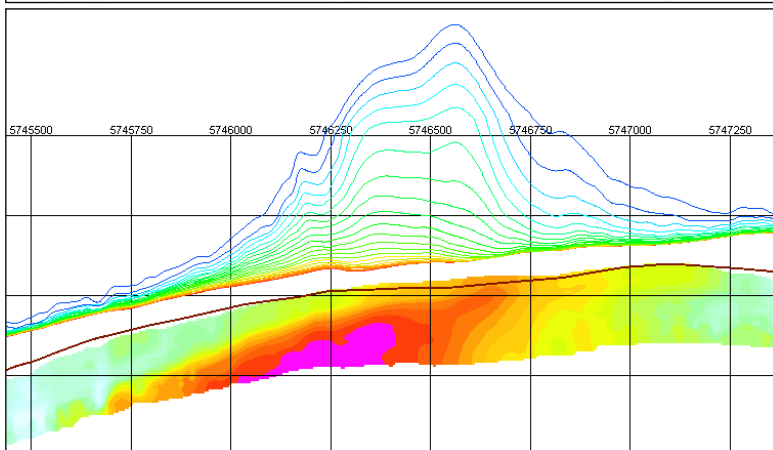
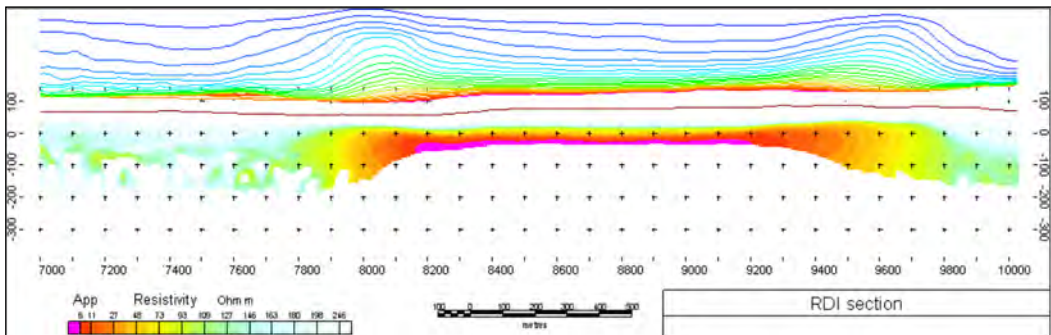
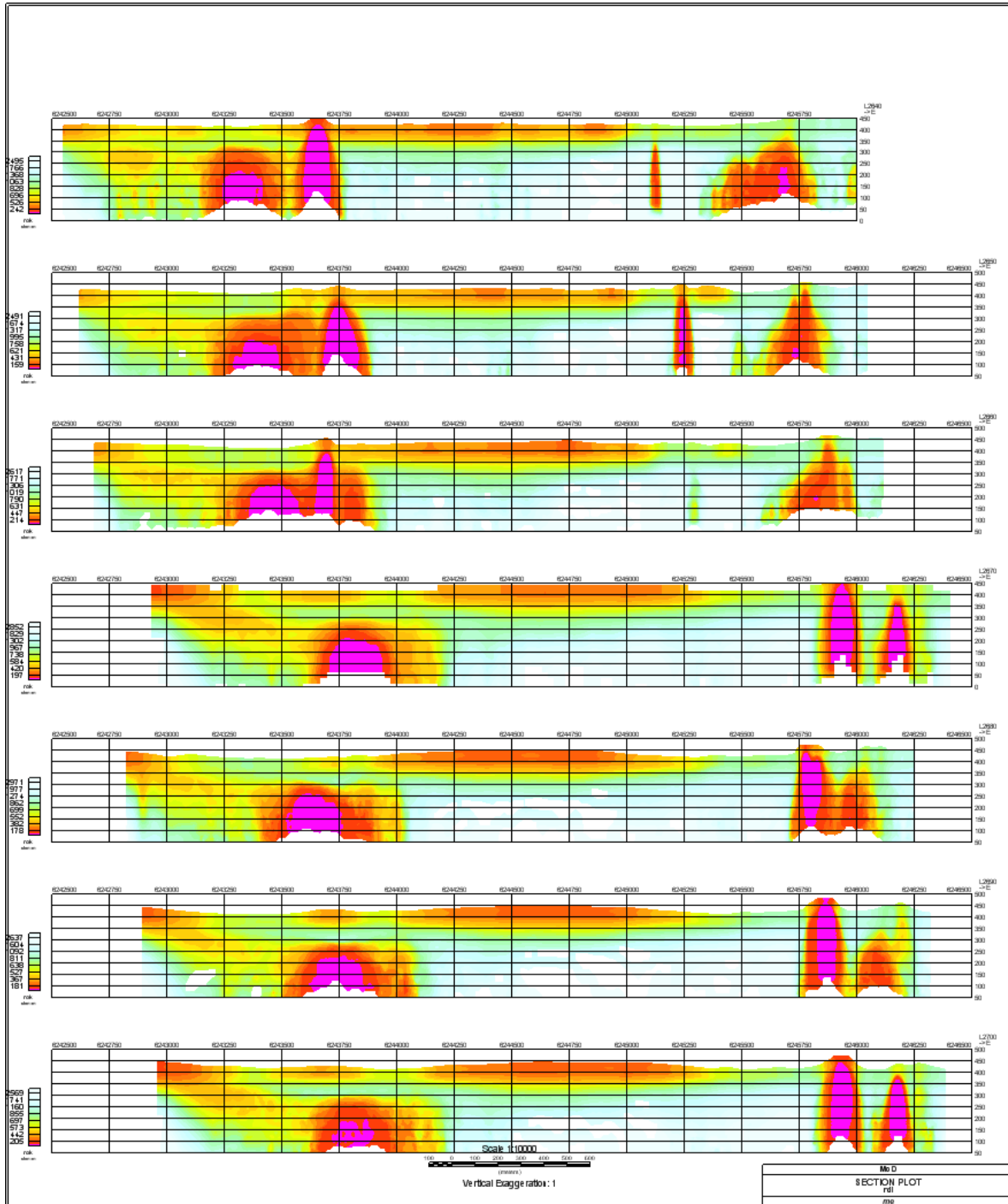


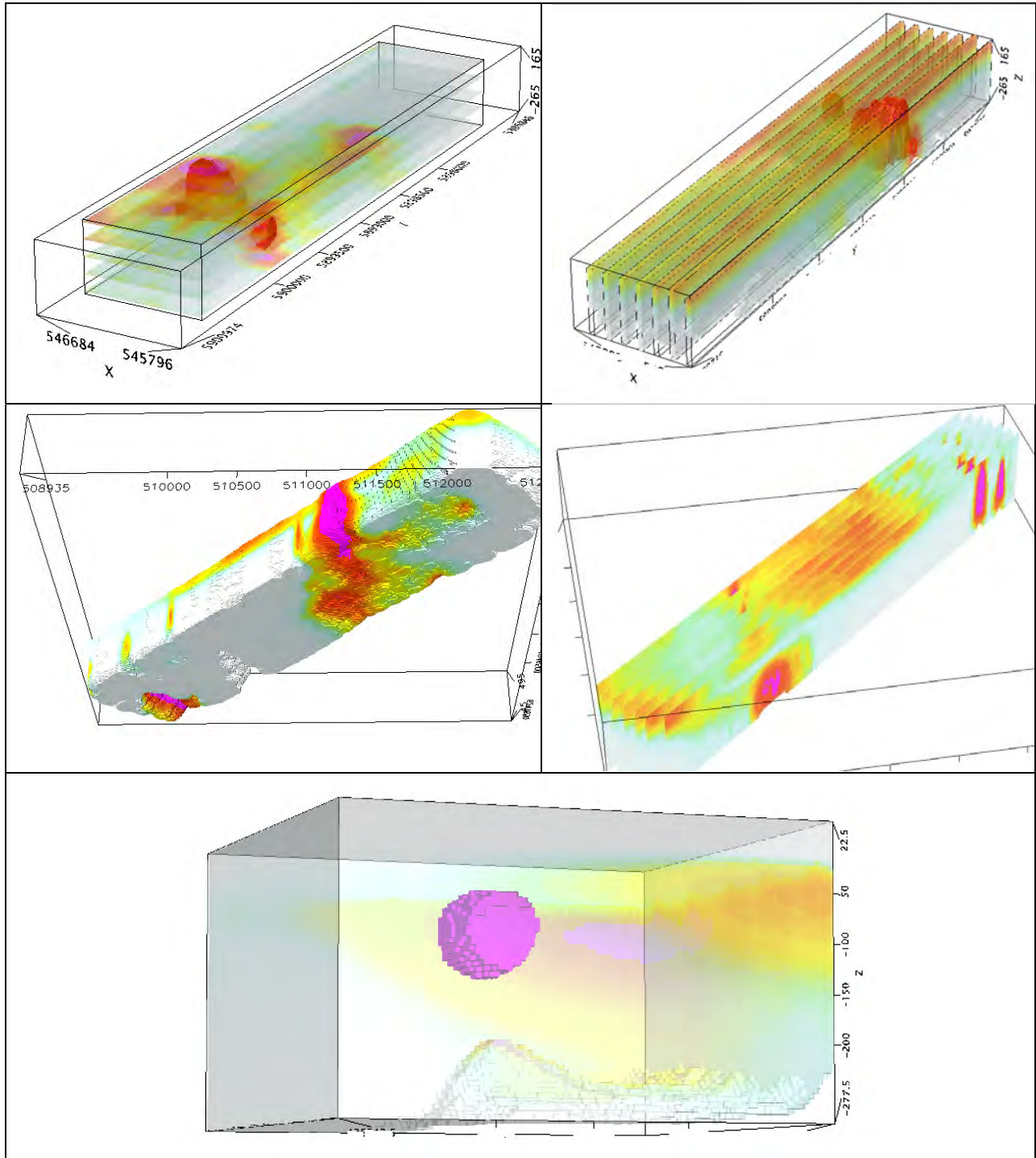
Figure F-11: RDI section for the real horizontal and slightly dipping conductive layers

# FORMS OF RDI PRESENTATION

## PRESENTATION OF SERIES OF LINES

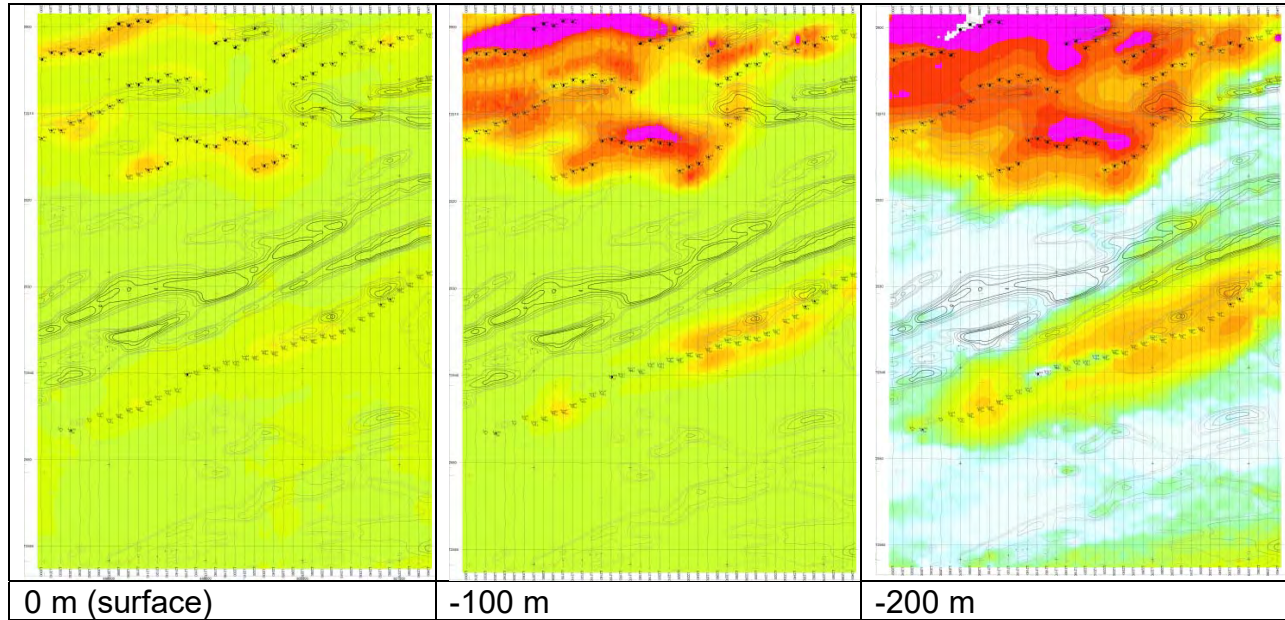


### 3D PRESENTATION OF RDIS

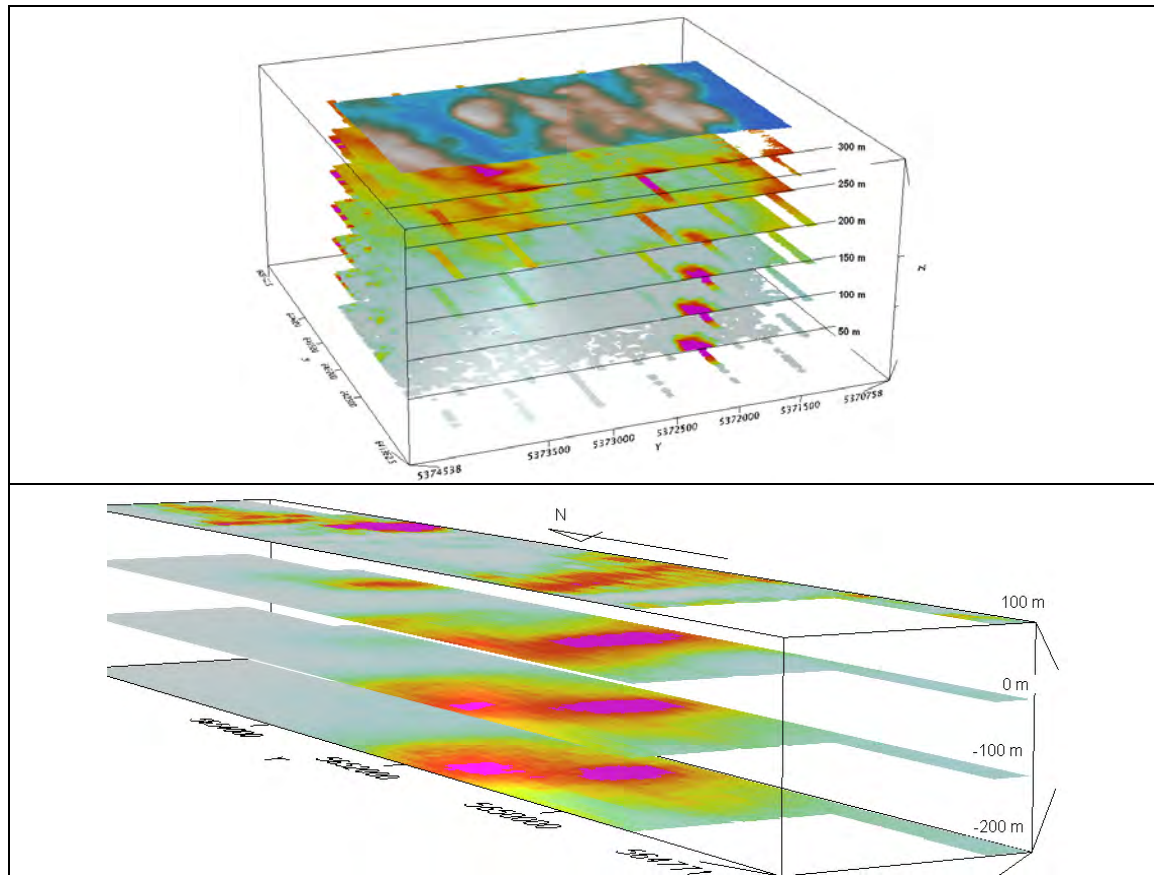




APPARENT RESISTIVITY DEPTH SLICES PLANS:



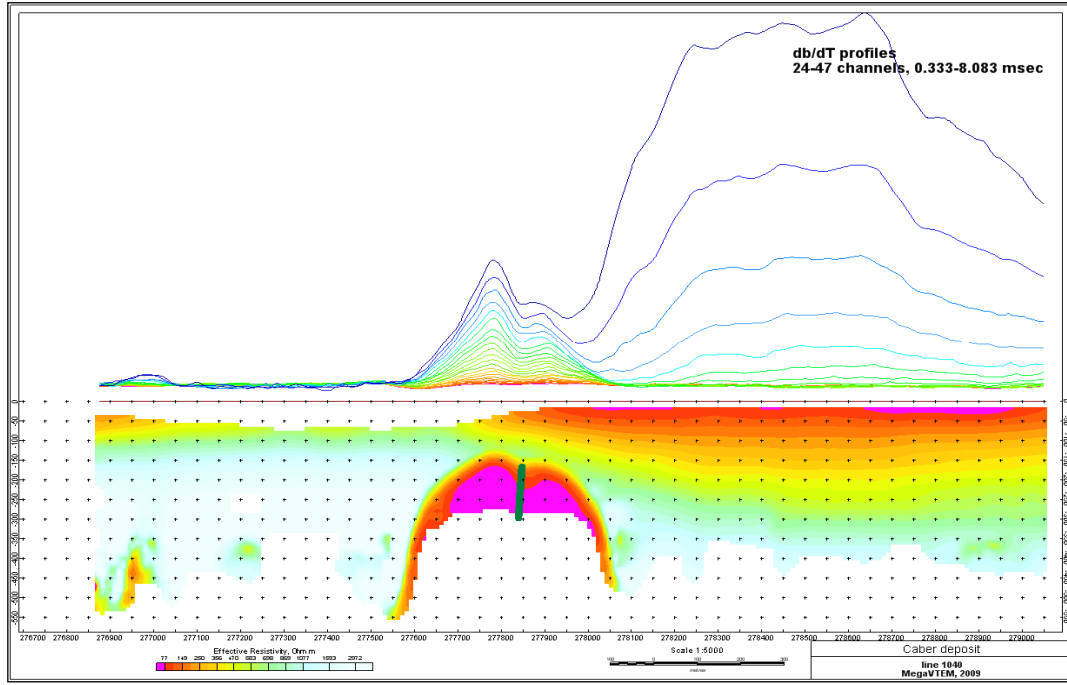
3D VIEWS OF APPARENT RESISTIVITY DEPTH SLICES:



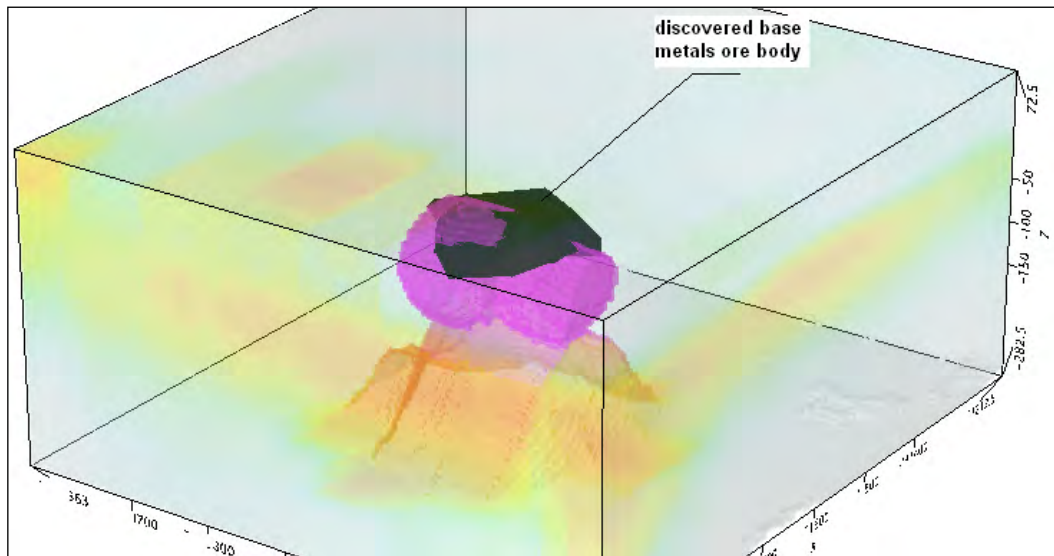


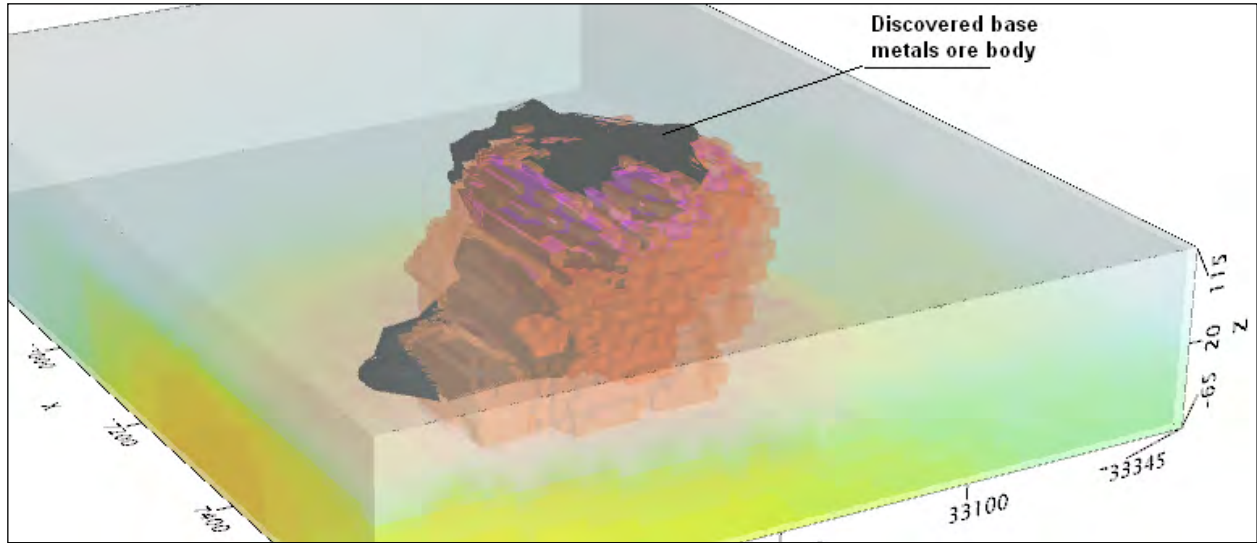
## REAL BASE METAL TARGETS IN COMPARISON WITH RDIS:

RDI section of the line over Caber deposit ("thin" subvertical plate target and conductive overburden).



## 3D RDI VOXELS WITH BASE METALS ORE BODIES (MIDDLE EAST):





Alexander Prikhodko, PhD, P.Ge  
**Geotech Ltd.**  
April 2011

## APPENDIX G

### RESISTIVITY DEPTH IMAGES (RDI)

Please see RDI folder on DVD for PDFs